

Old Dominion University

ODU Digital Commons

Chemistry & Biochemistry Theses & Dissertations

Chemistry & Biochemistry

Winter 2006

Development of Single Nanoparticle Optical Assays for Imaging Single Living Cells

William John Brownlow
Old Dominion University

Follow this and additional works at: https://digitalcommons.odu.edu/chemistry_etds



Part of the [Biochemistry Commons](#), and the [Pharmacology Commons](#)

Recommended Citation

Brownlow, William J.. "Development of Single Nanoparticle Optical Assays for Imaging Single Living Cells" (2006). Master of Science (MS), Thesis, Chemistry & Biochemistry, Old Dominion University, DOI: 10.25777/z0b3-q124
https://digitalcommons.odu.edu/chemistry_etds/27

This Thesis is brought to you for free and open access by the Chemistry & Biochemistry at ODU Digital Commons. It has been accepted for inclusion in Chemistry & Biochemistry Theses & Dissertations by an authorized administrator of ODU Digital Commons. For more information, please contact digitalcommons@odu.edu.

**DEVELOPMENT OF SINGLE NANOPARTICLE OPTICAL
ASSAYS FOR IMAGING SINGLE LIVING CELLS**

by

William John Brownlow
B.S. May 1994, Virginia Tech

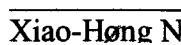
A Thesis Submitted to the Faculty of
Old Dominion University in Partial Fulfillment of the
Requirement for the Degree of

MASTER OF SCIENCE


CHEMISTRY

OLD DOMINION UNIVERSITY
December 2006

Approved by:

_____
Xiao-Hong Nancy Xu (Director)

_____
Kenneth Brown (Member)

_____
Christopher Osgood (Member)

_____
Jennifer Poutsma (Member)

ABSTRACT

DEVELOPMENT OF SINGLE NANOPARTICLE OPTICAL ASSAYS FOR IMAGING SINGLE LIVING CELLS

William John Brownlow
Old Dominion University, 2006
Director: Dr. Xiao-Hong Nancy Xu

Multi-drug resistance (MDR) has been reported in both prokaryotes and eukaryotes; the pathogenic gram-negative bacteria *Pseudomonas aeruginosa* can extrude a variety of structurally and functionally diverse substrates via a number of membrane transport systems leading to MDR. We have developed a novel nanoparticle assay to characterize both the membrane transport system composed of the MexAB–OprM efflux pump and the membrane permeability induced by antibiotics. Gold (Au) and silver (Ag) nanoparticles were investigated for use as probes to explore membrane transport in *P. aeruginosa*.

The surface plasmon absorption (color) of Au nanoparticle solutions was found to change in the presence of Tris(2, 2'-bipyridine)ruthenium(II). The color change was both size and temperature dependent. The change in surface plasmon absorption was caused by the formation of Au nanoparticle aggregates.

The surface plasmon absorption (color) of Ag nanoparticles was found to correlate with nanoparticle size and was readily observable using dark field microscopy. Ag nanoparticles were used to measure real-time transformation of cell permeability and MDR efflux dynamics of individual bacteria cells at nanometer resolution. The MDR efflux dynamics data was validated using time-course fluorescence of bulk cell populations.

**For all her love, support, and faith, this thesis is dedicated to my wife
Christina Marie Brownlow.**

ACKNOWLEDGMENTS

There are a number of people who have made the completion of this thesis possible. First and foremost, I would like to thank my academic advisor, thesis committee chair, and mentor Dr. Xiao-Hong Nancy Xu for the opportunity to work in her laboratory. In the few years spent in Dr. Xu's laboratory, I learned an array of analytical techniques but, more importantly, I learned the importance of ethical integrity, tenacity and strength of character. Without her guidance, encouragement and mentorship, it would not have been possible for me to complete this work.

I would like to extend my gratitude to the members of my thesis committee, Dr. Kenneth Brown, Dr. Christopher Osgood and Dr. Jennifer Poutsma for all their helpful advice and assistance throughout this undertaking. I would also like to thank my fellow colleagues in the Xu lab group, Robert Jeffers, Nazita Youseffi, Suang Huang, Michelle Nowak, Khalid Salatia, Qian Wan, Josh Viola, Christina Steel, and Sophia Kyriacou for their help and camaraderie.

I am truly blessed to have a large number of supportive friends and relatives. I would like to thank them all for the encouragement they have given me during my academic pursuits.

Financial support for this work was provided by the Department of Chemistry and Biochemistry at Old Dominion University and NIH (RR15057-01). The work was carried out at the Department of Chemistry and Biochemistry, Old Dominion University, Norfolk, VA.

ABBREVIATIONS

Å	Angstrom (10^{-10} meter)
ΔABM	<i>P. aeruginosa</i> (TNP076) mutant strain with no expression of MexA, MexB, OprM proteins
β-lactam	Antibiotic belonging to the beta-lactam family
°C	Degree Celsius
μg	Microgram (10^{-6} gram)
μL	Microliter (10^{-6} liter)
μm	Micrometer (10^{-6} meter)
AFM	Atomic force microscopy
Ag	Silver
AgNO ₃	Silver Nitrate
Au	Gold
AZT	Aztreonam
CCD	Charge coupled device
Chl	Chloramphenicol
cm	Centimeter (10^{-2} meter)
d	Density
D	Diameter
DNA	Deoxyribonucleic acid
EtBr	Ethidium bromide
Fig	Figure
g	Gram

h	Hour(s)
H ₂ O	Water
HAuCl ₄	Tetrachloroauric acid
HCl	Hydrochloric acid
HNO ₃	Nitric Acid
kV	Kilovolts (10 ³ volt)
LN	Liquid nitrogen
LPS	Lipopolysaccharide
MΩ	Megaohm (10 ⁶ ohm)
MgCl ₂	Magnesium chloride
MHz	Megahertz (10 ⁶ cycles per second)
MIC	Minimum inhibitory concentration
mL	Milliliter (10 ⁻³ liter)
mm	Millimeter (10 ⁻³ meter)
mol	Mole
ms	Millisecond (10 ⁻³ second)
MW	Molecular weight
N.A.	Numerical aperature
NaCl	Sodium chloride
nalB-1	<i>P. aeruginosa</i> (TNP030#1) mutant strain with over-expression of MexA, MexB, OprM proteins
nm	Nanometer (10 ⁻⁹ meter)
nM	Nanomolar (10 ⁻⁹ moles per liter)
NSOM	Near-field scanning optical microscopy

OD _{600nm}	Optical density measured at 600-nanometer wavelength
OsO ₄	Osmium tetroxide
PBS	Phosphate buffered saline
pH	Logarithmic measure of hydronium concentration
pM	Picomolar (10^{-12} moles per liter)
r	Radius
rpm	Revolutions per minute
Ru(bpy) ₃ ²⁺	Tris(2,2'-bipyridine)ruthenium(II)
SCE	Saturated calomel electrode
STM	Scanning tunneling microscopy
TEM	Transmission electron microscopy
UV-vis	Light in the ultraviolet and visible spectrum
V	Volume
W	Weight
WT	<i>P. aeruginosa</i> (PAO4290) with wild-type expression of MexA, MexB, OprM proteins

TABLE OF CONTENTS

	Page
LIST OF TABLES	x
LIST OF FIGURES	xiii
 Chapter	 Page
I. INTRODUCTION	1
Scope and Objectives	1
Nanoparticles	3
<i>Pseudomonas aeruginosa</i>	7
II. TUNABLE OPTICAL PROPERTIES OF NANOPARTICLES	16
Gold Nanoparticles	16
Experimental	18
Results	21
III. DIRECT MEASUREMENTS OF MEMBRANE PERMEABILITY AND MULTI-DRUG RESISTANCE OF <i>P. AERUGINOSA</i> USING SINGLE NANOPARTICLE OPTICS	42
Introduction	42
Experimental	44
Aztreonam Experiments	45
Results	46
Discussion	51
Chloramphenicol Experiments	54
Results	58
Discussion	69
IV. VALIDATION OF NANOPARTICLE OPTICS USING CONVENTIONAL METHODS	74
Introduction	74
Aztreonam Experiments	75
Results	76
Discussion	79
Chloramphenicol Experiments	79
Results	80
Discussion	85
V. CONCLUSIONS	87
Gold Nanoparticles	87
Aztreonam	87
Chloramphenicol	88
Ethidium Bromide	89

Page

REFERENCES 90

VITA97

LIST OF TABLES

Table	Page
1. Pathogenic Products of <i>Pseudomonas Aeruginosa</i>	11
2. The Minimum Concentrations of $\text{Ru}(\text{bpy})_3^{2+}$ Needed for the Color Change of Au Nanoparticle Solutions	35

LIST OF FIGURES

Figure	Page
1. Rayleigh and Mie Scattering Patterns.....	6
2. Tissues Affected by <i>P. Aeruginosa</i> Infection	9
3. Electron Micrograph of <i>P. Aeruginosa</i>	10
4. Membrane Composition and Permeability of Gram-positive and Gram-negative Bacteria.	14
5. Representative UV-vis Absorbance Spectra of 2.13 nM Au Nanoparticles (6.5 nm) in the Absence and Presence of $\text{Ru}(\text{bpy})_3^{2+}$ at 24 °C.	22
6. Representative UV-vis Absorbance Spectra of 0.36 nM Au Nanoparticles (19 nm) in the Absence and Presence of $\text{Ru}(\text{bpy})_3^{2+}$ at 24 °C	23
7. Representative UV-vis Absorbance Spectra of 6 pM Au Nanoparticles (48 nm) in the Absence and Presence of $\text{Ru}(\text{bpy})_3^{2+}$ at 24°C	24
8. Representative UV-vis Absorbance Spectra of 2 pM Au Nanoparticles (97 nm) in the Absence and Presence of $\text{Ru}(\text{bpy})_3^{2+}$ at 24 °C	25
9. Representative Plots of Baseline-Subtracted Peak Absorbance at 524 nm Versus Incubation Time are Constructed from the Absorbance Spectra of the Solution	37
10. Representative Color Photos of the Au Nanoparticle Solutions are Acquired from Experiments in FIG. 9, Showing Temperature-Dependence.....	38
11. Silver Nanoparticles.....	47
12. Monitoring Membrane Permeability of Multiple Cells (WT) Simultaneously in Real-Time Using Nanoparticle Optics.....	49
13. Direct Observation of Real-Time Size Transformation of Membrane Permeability of the Cells Induced by AZT	50
14. Characterization of Ag Nanoparticles, Color and Size Indices	59
15. Simultaneous Real-Time Monitoring of Membrane Transport in Multiple Living Cells (WT) With and Without Chloramphenicol	60
16. Direct Real-Time Observations of Dose-Dependent Changes in Membrane Permeability and Pore Sizes in <i>P. Aeruginosa</i> (WT), Induced by Chloramphenicol..	62

Figure	Page
17. Representative Normalized Histograms of the Number of Ag Nanoparticles with the Cells Versus Sizes of Nanoparticles from the solutions in Fig. 16.	63
18. Determination of Extracellular and Intracellular Ag Nanoparticles Using the Scattering Intensity of Nanoparticles	64
19. Transmission Electron Micrographs Showing Sizes and Locations of Ag Nanoparticles Inside Wild Type (WT) Cells.....	66
20. Real-Time Measurements of Accumulation Kinetics of Single Ag Nanoparticles in Living Cells	67
21. Real-Time Monitoring of EtBr Accumulation Kinetics in <i>P. Aeruginosa</i>	77
22. Minimum Inhibitory Concentration (MIC) of Aztreonam.....	78
23. Real-time Monitoring of EtBr Accumulation Kinetics in Living Cells.....	82
24. Minimum Inhibitory Concentration (MIC) of Chloramphenicol.....	84

CHAPTER I

INTRODUCTION

SCOPE AND OBJECTIVES

Effective therapy for infections stemming from *P. aeruginosa* has been problematic due to the microorganism's inherent resistance to a broad spectrum of antibiotics. *P. aeruginosa*'s antibiotic resistance is a result of many factors including low permeability of the outer membrane and the production of efflux pumps and β -lactamases (1). While researchers have investigated the multi-drug resistance (MDR) mechanism of *P. aeruginosa* for decades, a clear characterization and understanding of the efflux machinery responsible for multi-drug resistance still eludes us. Genomic sequencing of pathogenic bacteria indicates that efflux pumps are culpable in the disease process and empirical data suggests that the more complex the organism (i.e. larger genome) the greater the number and type of efflux pumps (2).

Despite decades of study, *P. aeruginosa* still thwarts our attempts to gain a true understanding of its multi-drug resistance mechanism. Many questions remain unanswered. For example: How do the MDR efflux proteins MexA, MexB, OprM assemble, sense, and selectively extrude antibiotics? What is the antibiotic susceptibility of MexA, MexB, and OprM? How do antibiotics cross the membrane of *P. aeruginosa*? How can a large molecule cross the membrane of *P. aeruginosa*? Does active extrusion by MexA, MexB, OprM, have steric limitations? This work aims to address some of these questions by the development of a nanoparticle optical assay to provide real-time imaging of the transformation of cell membrane permeability induced by antibiotics at

The model for this thesis is *The Journal of Biological Chemistry*.

single-cell resolution. The use of nanoparticle optical assays for single living cells is expected to provide a new tool to elucidate the multi-drug resistance mechanism.

The overall goal of this thesis is to develop an assay that uses nanoparticles that can visualize size transformations of cellular membranes on the nanometer scale in real time. This thesis also attempts to gain new understanding in both the permeability of the cellular membrane of *P. aeruginosa* and the activity of the MDR mechanism comprised of the MexA, MexB, OprM efflux pump with regard to substrate size. Active extrusion systems play an important role in cellular defense mechanisms of many living organisms including bacteria, yeasts, molds and mammalian cells (2-5).

Chapter I: The scope and objectives of this research are presented as well as a brief description of *P. aeruginosa*, and an overview of nanoparticle optics. The topics covered include *P. aeruginosa* as a human pathogen, MDR and efflux pumps, bulk versus surface plasmon resonance, Mie and Rayleigh scattering.

Chapter II: The experimental work done to characterize size dependant properties of gold nanoparticles is presented. The central theme of the chapter details the use of Ru(II)-tris-(2,2'-bipyridine) as a probe to investigate the surface chemistry of various sized Au nanoparticles.

Chapter III: Real-time monitoring of *P. aeruginosa* cell membrane permeability changes and multi-drug resistance using Ag nanoparticles in the presence of antibiotics is reported. The Experiments utilize varying concentrations of the antibiotics aztreonam and chloramphenicol in conjunction with three strains of *P. aeruginosa* to induce membrane permeability changes. The permeability changes and MDR are followed in real-time using multicolored Ag nanoparticles as nanometer-scale probes.

Chapter IV: Time-course bulk fluorescence measurements of *P. aeruginosa* incubated with ethidium bromide (EtBr) are reported. These experiments are used to validate the aztreonam and chloramphenicol results obtained using the nanoparticle assay.

Chapter V: A summary of the development of novel nanoparticle optical assays for imaging cell membrane transformation and MDR efflux kinetics of single living cells at the nanometer scale in real time is presented. Conclusions from the experimental results of the work described in preceding chapters are presented.

NANOPARTICLES

Nanochemistry

Chemistry is the branch of the physical sciences that has particular focus on the composition, structure, properties and reactions of matter particularly at the atomic and molecular level. Presently, nanochemistry is concerned with the development of novel synthesis and characterization methods for materials in the size range of 1 to 100 nm. Objects on this scale exhibit novel electronic, optical, magnetic, transport, photochemical, electrochemical, catalytic, and mechanical properties that are functions of composition, size and shape. The unique properties of nanoparticles do not correspond to those of the free atoms making up the nanoparticle nor to bulk solids comprised of the same material (6).

Current nanomaterials include nanoparticles, nanocrystalline structures, and nanodevices (7). Nanomaterials are single-phase or multiphase polycrystals with a typical crystal size of 1 to 100 nm. Depending on the dimensions, nanomaterials may be further classified into nanoparticles, layered or lamellar structures, filamentary structures and bulk nanostructured materials. Properties of such materials depend mostly on the

grain size and size distribution, chemical composition, interfaces, and interaction between constituent domains. Due to the large interface (surface) to volume ratio of nanomaterials, a wide variety of size dependent effects may be introduced by controlling the size of the nanoparticle. Some effects include quantum confinement, increased catalytic activity, and magnetism (7). Quantum confinement, the quantization of electron energy levels due to confined grain size, has application in semiconductors, optoelectronics, and non-linear optics. Quantum dots for example can be tuned to absorb and emit light at specific wavelengths by changing both the composition of the quantum dot and its diameter.

Gold and Silver Nanoparticles

In the 1980s, gold and silver nanoparticles were readily used as molecular probes for studying sub-cellular events. Gold nanoparticles on the 20 to 40 nm scale were being employed to detect microtubule-dependent intracellular motility (8). By conjugating gold nanoparticles to specific ligands, nanoparticles were used as probes to study a variety of biological systems such as intracellular motility, cell membrane dynamics, intracellular routing, and cell receptor translocation (9). Both gold and silver nanoparticles were used to study the motion of motor molecules and membrane proteins (10 - 13). To study nitric oxide release from macrophages, Au nanoparticles have been modified with fluorescent dyes (14). Numerous articles have been written which mention the use of both gold and silver nanoparticles to study facets of microtubules (15). Au nanoparticles attached to monoclonal tubulin antibodies are used to study the relative motion of microtubules as motor driven microtubule transport (16). These nanometer-sized particles constitute an essential tool for studying a variety of biological and cellular events.

Characteristics of Single Silver Nanoparticles

Much of this thesis centers on the use of nonbleaching, multicolored silver nanoparticles ranging from approximately 10 to 100 nm in diameter as molecular probes for the real time study of membrane permeability transformations. We used these single silver nanoparticles because of their unique optical properties (i.e. surface plasmon resonance spectra).

The study of colloidal metal nanoparticles has a long history due to the strong optical resonance in the visible portion of the electromagnetic spectrum, permitting the use of metal nanoparticles in the design of colored glasses for stained glass in cathedrals and art ware (17). The Mie theory of scattering and absorption, which explains much of the fundamental characteristics of colloidal nanoparticles, was published in 1908. According to Mie theory, the concepts of geometrical optics such as refraction and reflection that are familiar in the macroscopic world do not adequately describe the interaction of particles with light when the particle size is comparable to the wavelength of the light. The mathematics of Mie theory addresses the full complexity of vector electromagnetic quantities interacting with a particle (18) but is outside the scope of this thesis. Fig. 1 provides a visual to understand the difference between Mie scattering and Rayleigh scattering. A strong forward scatter characterizes Mie scattering; note as the particle becomes larger, the forward scattering intensifies. Many methods have been developed to produce nanoparticles including precipitation from solution, sol-gel, ion implantation, precipitation of metal clusters via annealing, chemical synthesis, co-sputtering, electron-beam lithography and low energy cluster-beam (19, 20).

The optical properties, including color, of the silver nanoparticles are determined by surface plasmon resonance of the nanoparticles and depend on the size, shape and

dielectric constant of the medium as described by Mie theory with a quasi-static regime (21, 22). Unlike the bulk plasmon, propagating electromagnetic waves (e.g. light) can directly excite the surface plasmon of nanoparticles.

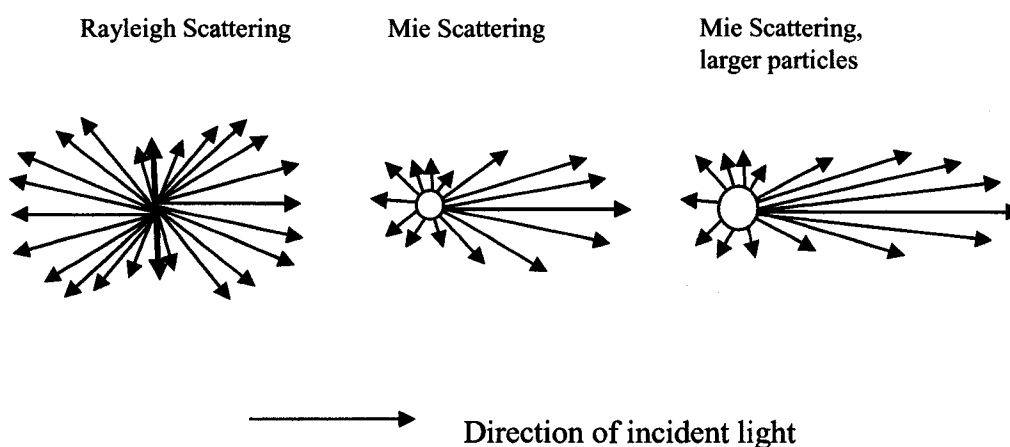


FIGURE 1. Rayleigh and Mie scattering patterns. Mie scattering becomes more wavelength (λ) dependent as particle size decreases. Rayleigh scattering dominates when the particle dimension is $\ll 1/10$ of λ .

Due to the size of the nanoparticle, the conducting electrons making up the surface plasmon are quantumly confined; therefore only specific energy frequencies will excite the plasmon. This leads to selective absorption of light wavelengths and results in colored nanoparticles. If the shape and medium are kept constant, adjusting the size of the particle will change its color. We have calibrated a wide spectrum of silver nanoparticle probes using plasmon resonance spectra and transmission electron microscopy (TEM). A statistical comparison showed that the color of our Ag nanoparticles corresponded to nanoparticle size. We have used these multicolored

probes as a nanometer size-index to directly measure microbial cell wall permeability transformations.

We have demonstrated that Ag nanoparticles can measure the sizes of many events simultaneously using dark-field microscopy and spectroscopy. We can measure many single membrane transformations on single living cells at nanometer spatial resolution with millisecond temporal resolution. This unique system is superior to TEM in that TEM cannot make real time measurements of living systems. The technique is also superior to scanning probe microscopy, including AFM, STM, and NSOM, due to both the low temporal resolution of scanning probe techniques and the inability of these techniques to measure intracellular nanoparticles.

PSEUDOMONAS AERUGINOSA

Human Pathogen

P. aeruginosa is part of the genus *Pseudomonas* which contains more than 140 individual species, the majority of which are saprophytic, meaning they obtain their nutrition by assimilating decaying organic matter (23). *P. aeruginosa* is found almost anywhere in the natural habitat in sites ranging from surface waters to vegetation and soil. It can multiply in distilled water but is rarely isolated from sea water except near sewage outfalls and polluted river estuaries. It is not a fish pathogen. The organism is a resident of the soil and rhizosphere and is frequently recovered from fresh vegetables and plants. It is pathogenic for plants such as tobacco, cucumbers and lettuce and is also a well-established pathogen of grasshoppers and insects.

P. aeruginosa has been isolated from a variety of sources including aviation fuel, cutting oils, cosmetics, plasticizers, and photographic materials. Hospital and domestic sink traps, taps and drains are invariably colonised by pseudomonads. *P. aeruginosa* dies

rapidly on dry human skin but in conditions of superhydration of the skin, such as divers in long term saturation chambers and military personnel in swampy terrain, the frequency of colonization is markedly increased and infections such as otitis externa in divers and toe web rot in soldiers are common.

Despite the commonality of the organism, acquired infections of *P. aeruginosa* are relatively rare. In hospitals, however, *P. aeruginosa* may account for about 10% of all infections acquired during the patients' stay. *Pseudomonas* induced pneumonia, urinary tract, surgical wound and blood stream infections are all common. The species is a particularly frequent cause of chronic respiratory infection in cystic fibrosis patients. *P. aeruginosa* has a low intrinsic virulence in man and animals. Thermal injury or neutropenia or the introduction of relatively large inocula direct into tissues are often necessary prerequisites for the establishment of infection. Fig. 2 provides an illustration of the diverse tissues in which *P. aeruginosa* may cause infection.

Structure and Pathogenic Mechanism

P. aeruginosa is a gram-negative rod with a width of 0.5-0.8 μm and a length of 1.5-3.0 μm (24). Most strains are motile by means of a single polar flagellum, though some strains have multiple flagella (Fig. 3). Clinical isolates are likely to have pili which are thought to aid against phagocytosis and also aid in bacterial attachment, thus promoting colonization. The cell envelope of *P. aeruginosa* is similar to other gram-negative bacteria, consisting of three layers: the inner membrane, a peptidoglycan layer, and the outer membrane. The outer membrane is composed of phospholipids, protein, and lipopolysaccharide (LPS). The lipopolysaccharide of *P. aeruginosa* is less toxic than that of other typical gram-negative bacteria. The LPS of most strains of *P. aeruginosa*

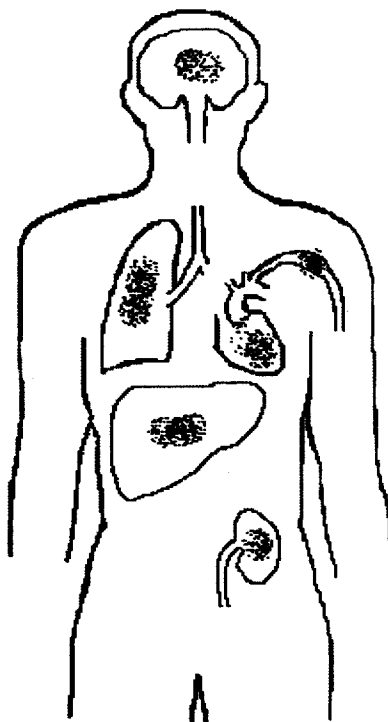


FIGURE 2. Tissues affected by *P. aeruginosa* infection. This opportunistic pathogen may infect virtually any tissue. Infection is facilitated by the presence of underlying disease (e.g., cancer, cystic fibrosis) or by a breakdown in nonspecific host defenses (as in burns).

contains 2-keto-3-deoxyoctonic acid, hydroxy fatty acids, heptose, side chain, and core polysaccharides (25). Studies of clinical isolates suggest strong conservation of many of the outer membrane proteins in *P. aeruginosa*. Although numerous seroloci types exist, many of the outer membrane proteins from these strains are antigenically crossreactive. *P. aeruginosa* is a non-fermentative aerobe that obtains energy from oxidation of carbohydrates. Although the bacteria are able to use more than 75 different organic compounds, it will only grow on media providing acetate and ammonium sulfate as carbon and nitrogen sources. *P. aeruginosa* is a facultative anaerobe using nitrate as an electron acceptor. The bacteria grow well between 25 °C and 37 °C, but will survive at

elevated temperatures; the ability to grow at 42 °C helps distinguish *P. aeruginosa* from other bacteria in the *Pseudomonas* genus.

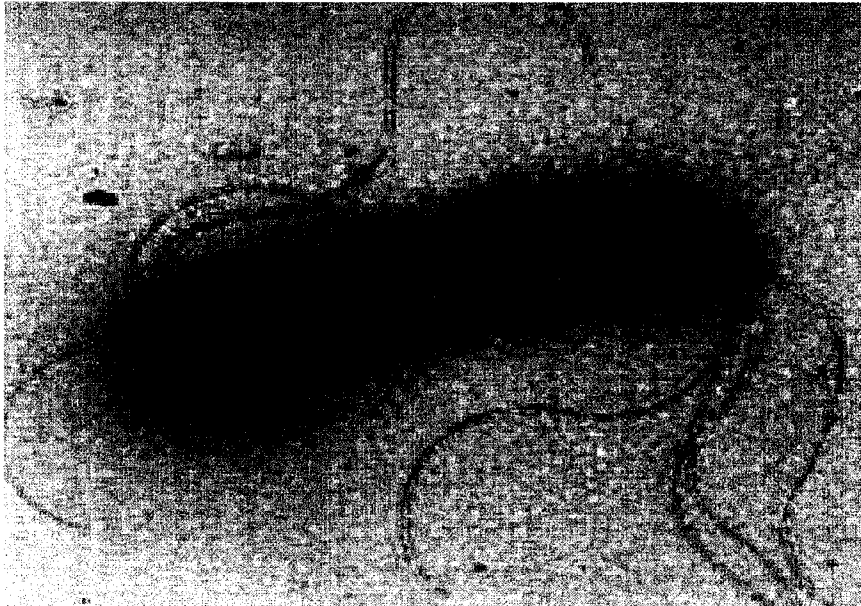


FIGURE 3. Electron Micrograph of *P. aeruginosa*. Source of micrograph is [http:// www.textbookofbacteriology.net](http://www.textbookofbacteriology.net)

The ability of *P. aeruginosa* to invade tissues depends upon production of extracellular enzymes and toxins that break down physical barriers and damage host cells, as well as resistance to phagocytosis and the host immune defenses (Table 1).

Two extracellular proteases associated with virulence exert their activity at the invasive stage: elastase and alkaline protease. Elastase has several activities that relate to virulence. The enzyme cleaves collagen, IgG, IgA, and complement. It also lyses fibronectin to expose receptors for bacterial attachment on the mucosa of the lung.

TABLE 1Pathogenic products of *Pseudomonas aeruginosa*

Product	Strains Producing Product	Role of Product
Endotoxin	100 %	Terminal shock
Heat-stable hemolysin	95 %	Macrophage toxicity
Leukocidin	4 %	Depress host defense
Phospholipase C	70 %	Hydrolysis of lecithin
Pigments	90 %	Antimicrobial agents
Proteases	90 %	Tissue necrosis and spreading factor
Toxin A	90 %	Lethality and inhibition of host defenses
Exoenzyme S	90 %	Local and systemic toxicity

Elastase disrupts the respiratory epithelium and interferes with ciliary function. Alkaline protease interferes with fibrin formation and will lyse fibrin. Together, elastase and alkaline protease destroy the ground substance of the cornea and other supporting structures composed of fibrin and elastin. Elastase and alkaline protease together are also reported to cause the inactivation of gamma interferon and tumor necrosis factor.

P. aeruginosa produces three other soluble proteins involved in invasion: a cytotoxin and two hemolysins. The cytotoxin is a pore-forming protein. It was originally named leukocidin because of its effect on neutrophils, but it appears to be cytotoxic for most eukaryotic cells (26). Of the two hemolysins, one is a phospholipase and the other is a lecithinase. They appear to act synergistically to break down lipids and lecithin. The

cytotoxin and hemolysins contribute to invasion through their cytotoxic effects on eukaryotic cells.

One *Pseudomonas* pigment is probably a determinant of virulence for the pathogen. The blue pigment, pyocyanin, impairs the normal function of human nasal cilia, disrupts the respiratory epithelium, and exerts a pro-inflammatory effect on phagocytes. Pyocyanin is also known to retard the growth of some other bacteria and may help colonization by *P. aeruginosa*. A derivative of pyocyanin, pyochelin, is a siderophore that is produced under low-iron conditions to sequester iron from the environment for growth of the pathogen. No direct role in virulence is known for the pigment fluorescein (26).

Multi-Drug Resistance in *P. aeruginosa*

The multi-drug resistance (MDR) mechanism of *P. aeruginosa* has been under study for decades to develop a better understanding of antibiotic resistance in prokaryotes and to develop more effective treatment regimens for *Pseudomonas* infection. Several genes encoding multi-drug efflux systems have been reported in *P. aeruginosa*; they include the MexAB-OprM, Mex CD-OprJ, MexXY-OprM, and MexEF-OprN (27-29). Of the known MDR genes, the efflux pump encoded by MexAB-OprM is the most highly expressed pump in the wild type (WT) microorganism. This efflux pump consists of two inner membrane proteins and a single outer membrane protein. The two inner proteins are MexA and MexB; MexA (40 kDa) serves as an accessory periplasmic protein, while the role of MexB (108 kDa) is a cytoplasmic membrane efflux transporter. The outer membrane protein OprM (50 kDa) serves as a channel forming protein (29).

The roles of the individual proteins were elucidated by the construction of mutant strains of *P. aeruginosa* in which genes encoding the individual proteins were deleted. The effect of individual protein deletion on the multi-drug extrusion system was evaluated by measuring the accumulation of fluorescent probes within the bacteria. Several fluorescent probes including 2-(4-dimethylaminostyryl)-1-ethylpyridinium (DMP), 1-(4-trimethylammoniumphenyl)-6-phenyl-1,3,5-hexatriene (TMA-DHP) and ethidium bromide (EtBr) have been used in such accumulation experiments (29). The results of the studies demonstrate that fluorescent probes are capable of monitoring the function of drug extrusion mechanisms in real time.

The role of the outer membrane permeability barrier together with the efflux pump has been studied and the results showed that the interplay of the outer membrane permeability barrier and the xenobiotic extrusion pump lowers the intracellular substrate concentration (30, 31). Among the MexAB-OprM, MexCD-OprJ, and MexEF-OprN extrusion pumps in *P. aeruginosa*, the MexAB-OprM was the most efficient in the extrusion of fluorescent dyes.

The intrinsic resistance expressed by all *P. aeruginosa* isolates was originally thought to be a result of the inherent impermeability of the gram negative cell (Fig. 4), but it is now known to involve an interplay of impermeability with multi-drug extrusion which is primarily mediated by the MexAB- OprM efflux pump. The MexB protein is a broad-spectrum pump located in the cytoplasmic membrane, while OprM protein is a pore-forming protein through which xenobiotics are expelled from the cell; MexA forms the linkage between the pump and the pore (32).

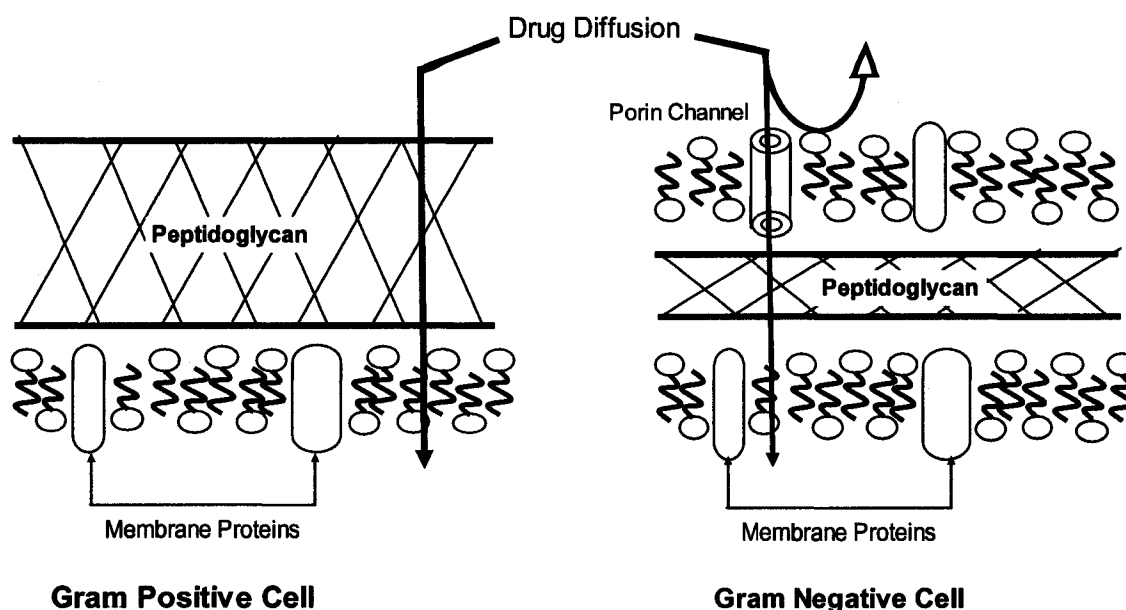


FIGURE 4. Membrane Composition and Permeability of Gram-positive and Gram-negative Bacteria.

Although a number of efflux systems have been identified and characterized, the underlying mechanism of multi-drug resistance remains unclear. How individual bacterium develop multi-drug resistance is not well understood. Neither the mechanism by which antibiotic resistance is induced nor the efflux kinetics of the various pumping systems is known. Several models have been proposed to describe how the membrane pump proteins recognize specific substrates and transport them out of the cell. It is unclear whether the substrates stay temporarily or are stored permanently in the cellular membrane where the pump proteins are located. It is still an open question about how rapidly substrates diffuse into the cell, and how quickly the pump recognizes substrates as foreign substances. It is also unclear how large a substrate can enter living cells and how large a substrate can the efflux system handle. This thesis reports the development

of a novel nanoparticle assay allowing the direct measurement of cellular membrane permeability on the nanometer scale with millisecond resolution.

CHAPTER II

TUNABLE OPTICAL PROPERTIES OF NANOPARTICLES

GOLD NANOPARTICLES

Introduction

Colloidal gold (Au) nanoparticles have superior stability, uniform surface and high affinity for organic functional groups. In addition, colloidal Au nanoparticles show unique size- and shape-dependent optical, electronic and catalytic properties (33-38). These unique features provide the possibility of developing biocompatible Au nanoparticles for bioanalysis (39-48), interfacing Au nanoparticles with living cells, and building nanoparticle blocks for nano-optical devices (49). Surface plasmon absorption of Au nanoparticles depends upon its size, shape and surrounding surface environments (e.g., surface adsorbates and inter-nanoparticle spacing). Unlike the bulk plasmon, the surface plasmon of Au nanoparticles can be directly excited by propagating light waves (electromagnetic waves), leading to the absorption and scattering of selective wavelengths of light. Therefore, one could tune the color of the nanoparticles by carefully controlling the size, shape and surface environment of the nanoparticles. Despite extensive studies over decades, it still remains a challenge to precisely control the optical properties of Au nanoparticles (50 - 54). Furthermore, it is not yet fully understood how the surface adsorbates of Au nanoparticles affect the optical, electronic and catalytic properties of the nanoparticles (55 - 56). For instance, do the optical properties of Au nanoparticles depend upon its surface adsorbed species (6-12, 49-56)? What mechanisms are involved? Are the optical properties of Au nanoparticles sensitive to temperature in the presence of surface adsorbates? These are key questions to be

addressed in order to rationally design Au nanoparticles for biochemical sensing and assembly of nano-optical devices (57-59).

Tris(2,2'-bipyridine)ruthenium(II), $\text{Ru}(\text{bpy})_3^{2+}$, has rich photochemistry, photophysics, and photoredox properties. It provides intense absorption bands at 285 nm ($\epsilon = 1.2 \times 10^5 \text{ M}^{-1}\text{cm}^{-1}$) and 452 nm ($\epsilon = 1.5 \times 10^4 \text{ M}^{-1}\text{cm}^{-1}$) and gives off intensive phosphorescence at 600 nm with a quantum yield of 0.042 at ambient temperature (60). Previous studies have demonstrated that $\text{Ru}(\text{bpy})_3^{2+}$ directly adsorbed on the Au surface using the hydrophobic interaction of tris-bipyridine with the surface Au atoms (61).

In this study, we select $\text{Ru}(\text{bpy})_3^{2+}$ as a probe to study the dependence of optical properties of Au nanoparticles upon its surface environment because the unique optical and electrochemical properties of $\text{Ru}(\text{bpy})_3^{2+}$ offer an opportunity to probe the surface properties of Au nanoparticles using an array of ultrasensitive detection means. Furthermore, the study of the photochemical and photocatalytic properties of $\text{Ru}(\text{bpy})_3^{2+}$ adsorbed on the surface of Au nanoparticles is also an interesting and important topic.

In previous studies, Ru(II)-tris-(2,2'-bipyridine)-cyclobis(paraquat-p-phenylene) catenane was used as a photosensitizer to cross-link Au-nanoparticle arrays for photoelectrochemical and electrochemical sensing. The emission of $\text{Ru}(\text{bpy})_3^{2+}$ quenched by Au nanoparticles has also been reported (62). Unlike these previously reported studies, this work will describe the dependence of surface plasmon absorption (color) upon the size of the nanoparticles, the amount of surface adsorbed $\text{Ru}(\text{bpy})_3^{2+}$, and temperature. To the best of our knowledge, surface plasmon absorption of Au nanoparticles as a function of nanoparticle size and temperature in the presence of $\text{Ru}(\text{bpy})_3^{2+}$ has not yet been reported. This study provides new opportunities to probe surface and optical properties of Au nanoparticles, the coagulation rate of the

nanoparticles, the chemical interface damping model (63-64), photochemistry and photocatalytical properties of $\text{Ru}(\text{bpy})_3^{2+}$ on Au nanoparticle surfaces, and to develop Au nanoparticles for ultrasensitive sensing and nano-optics.

EXPERIMENTAL

Chemicals and Materials

$\text{HAuCl}_4 \cdot 2\text{H}_2\text{O}$, sodium citrate dihydrate, tannic acid, and $\text{Ru}(\text{bpy})_3\text{Cl}_2 \cdot \text{H}_2\text{O}$ are purchased from Aldrich and used as received without further purification. Ultra-pure water (Nanopore, 18 M Ω , sterilized) is used to prepare all solutions and to synthesize Au nanoparticles. The stock solution of 45.5 μM $\text{Ru}(\text{bpy})_3^{2+}$ is prepared using ultrapure water and stored in a light-protected container at 4 °C.

Synthesis and Characterization of Au Nanoparticles

The Au nanoparticles with a diameter of 6.5, 19, 48, and 97 nm are prepared using the synthesis procedures as described previously (65); nanoparticle sizes were confirmed using transmission electron micrographs. Glassware is cleaned with aqua regia (3:1 of HCl to HNO_3), rinsed with ultrapure water, and then dried prior to the use. The 6.5 nm Au nanoparticles are prepared as follows: (i) a mixture of freshly prepared tri-sodium citrate (10 mL, 1%) and tannic acid (2.25 mL, 1%) is rapidly added into a stirring and refluxing HAuCl_4 (0.01%, 500 mL), leading to a color change of solution from yellow to violet within seconds. (ii) The solution is refluxed for additional 5 minutes, cooled to room temperature, and subsequently filtered using a 0.22 μm filter. The Au nanoparticles of 19, 48 and 97 nm are prepared by adding 50 mL of 38.8 mM, 5 mL of 1%, 2.1 mL of 1% of freshly prepared sodium citrate into a stirring and refluxing HAuCl_4 (0.01%, 500 mL), respectively. The solutions are refluxed for

additional 15 minutes, cooled to room temperature, and subsequently filtered using a 0.22 μm filter.

These Au nanoparticles are characterized using UV-vis spectroscopy (U 2010, Hitachi and Cary-3G, Varian) and transmission electron microscopy (TEM) (JEOL 100CX). Au nanoparticles are prepared on 100 mesh formvar coated copper grids (Electron Microscopy Sciences) for TEM imaging.

The concentrations of the Au nanoparticles are calculated as follows. The weight of Au (W_{Au}) produced from the complete reduction of HAuCl_4 is calculated by multiplying the moles of added HAuCl_4 (weight of added $\text{HAuCl}_4 \cdot 2\text{H}_2\text{O}$ divided by molecular weight (MW) of $\text{HAuCl}_4 \cdot 2\text{H}_2\text{O}$) with the atomic weight of Au (196.97 g/mol). The volume of generated Au (V_{Au}) is calculated by dividing the weight of produced Au (W_{Au}) by the density of Au ($d = 19.32 \text{ g/cm}^3$), as $V_{\text{Au}} = W_{\text{Au}}/d$. The number of the Au nanoparticles (diameter (D) = 6.5, 19, 48, 97 nm) is computed by dividing the volume of generated Au (V_{Au}) by the volume of an individual Au nanoparticle ($4/3\pi r^3$). The moles of Au nanoparticles are then determined by dividing the number of Au nanoparticles by Avogadro's constant (6.02×10^{23}). Finally, the molar concentrations of Au nanoparticles are calculated by dividing the moles of Au nanoparticles by the solution volume. Using this approach, the concentration of 6.5, 19, 48 and 97 nm Au nanoparticles is determined as 29.9 nM, 4.3 nM, 74 pM, and 8.2 pM, respectively. The 6.5, 19 and 48 nm Au nanoparticle solutions are diluted 10 times and the 97 nm Au nanoparticle solution is diluted 3 times using ultrapure water prior to its titration with $\text{Ru}(\text{bpy})_3^{2+}$.

Titration of Au Nanoparticle Solution with $\text{Ru}(\text{bpy})_3^{2+}$

The diluted Au nanoparticle solutions (2500 μL) are used for all titration experiments. In these experiments, the Au nanoparticle solutions are mixed with $\text{Ru}(\text{bpy})_3^{2+}$ solution (45.5 μM) and ultrapure water to prepare a final solutions of 3500 μL . Thus, the final concentrations of the 6.5, 19, 48 and 97 nm Au nanoparticle solutions are 2.13 nM, 0.36 nM, 6 pM, and 2 pM, respectively.

Ultrapure H_2O and 2500 μL Au nanoparticle solution are first added into a clean quartz cuvette (optical path 10 mm). A timer is started simultaneously as $\text{Ru}(\text{bpy})_3^{2+}$ solution is mixed with the Au nanoparticle solution in the cuvette. The cuvette with a tightened cap is quickly inverted several times to mix the solution and is inserted into the cuvette holder of the UV-vis spectrometer. The absorbance spectra of the mixture are recorded over 2 h by repeatedly scanning wavelength from 200-800 nm. Different volumes of $\text{Ru}(\text{bpy})_3^{2+}$ are used to titrate the Au nanoparticle solution to determine the minimum (critical) concentration of $\text{Ru}(\text{bpy})_3^{2+}$ that is needed to change the color of Au nanoparticle solution. Plots of baseline-subtracted peak absorbance versus time at the corresponding $\text{Ru}(\text{bpy})_3^{2+}$ concentration are used to determine the dependence of color-change kinetics upon $\text{Ru}(\text{bpy})_3^{2+}$ concentration. After the Au nanoparticle solutions have been measured using UV-vis spectroscopy over 2 h (Fig. 5A-8A), TEM samples of the Au nanoparticle solutions in the absence and presence of $\text{Ru}(\text{bpy})_3^{2+}$ are prepared on 100 mesh formvar coated copper grids and imaged using TEM (Fig. 5-8: C&D).

Temperature-Dependence Experiment

The circulating water bath of the UV/vis spectrometer (Cray 3G Varian) is used to maintain solution temperature in the cuvettes at 24.0, 33.0, 51.0°C, respectively. To maintain a homogenous mixture and temperature, a tiny stirring bar is used to mix the

solution in the cuvette during the experiments. Using the same approach as described above in the titration experiments, the minimal (critical) concentration of $\text{Ru}(\text{bpy})_3^{2+}$ for the color-change of Au nanoparticles at 33.0°C is determined. Plots of baseline-subtracted peak absorbance versus time in the presence of the critical concentration of $\text{Ru}(\text{bpy})_3^{2+}$ at 24.0, 33.0, 51.0°C are used to study the temperature-dependence of the color-change rate of the Au nanoparticle solution (Fig. 9). Two sizes of Au nanoparticles, 19 nm and 48 nm, are selected to investigate whether the temperature-dependence of the color-change kinetics is associated with the size of nanoparticles.

RESULTS

Synthesis and Characterization of Au Nanoparticles

The Au nanoparticles are synthesized as described above and were characterized using UV-vis spectroscopy and TEM. The surface plasmon absorption of Au nanoparticles occurs at a peak absorbance wavelength (λ_{max}) of 519, 524, 531, and 545 nm for the sizes of nanoparticles of 6.5 ± 1.5 , 18.6 ± 3.5 , 48.1 ± 5.8 , and 96.7 ± 15.4 nm, respectively (Fig. 5-9). Typical electron micrographs used to determine nanoparticle size are also provided (Fig. 5-9). The peak wavelength indicates a red shift with a broader bandwidth as the size of nanoparticles increases, demonstrating that the surface plasmon absorption of Au nanoparticles shows size-dependence. As reported in the literature, the intense color of Au nanoparticles is attributable to collective oscillation of free conduction electrons.

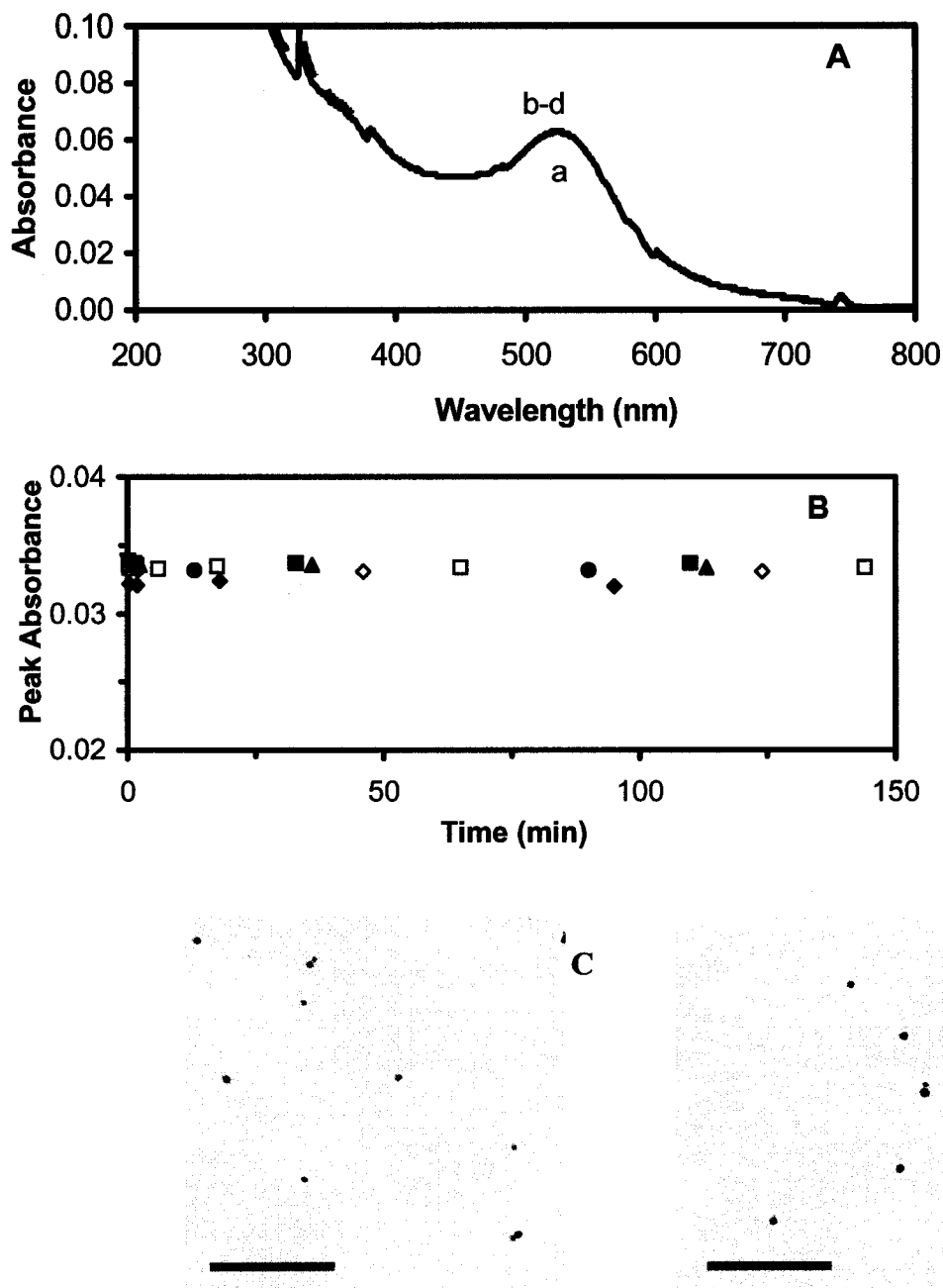


FIGURE 5. Representative UV-vis absorbance spectra of 2.13 nM Au nanoparticles (6.5 nm) in the absence and presence of Ru(bpy)_3^{2+} at 24 °C. A, Absorbance spectra are taken from the Au nanoparticle solutions incubated with 0-142 nM Ru(bpy)_3^{2+} for (a) 0 to (b-d) 2 hours. B, Plots of baseline-subtracted peak absorbance at 519 nm versus time are constructed from the absorbance spectra of the Au nanoparticle solutions incubated with Ru(bpy)_3^{2+} concentrations at (♦) 107 nM, (■) 114 nM, (▲) 119 nM, (◇) 131 nM, (□) 142 nM, and (●) 568 nM NaCl or MgCl_2 . TEM images are acquired from 2.13 nM of the 6.5 nm Au nanoparticle solutions that have already been incubated with (C) 0 and (D) 142 nM Ru(bpy)_3^{2+} for 2 hours. The scale bar represents 94 nm.

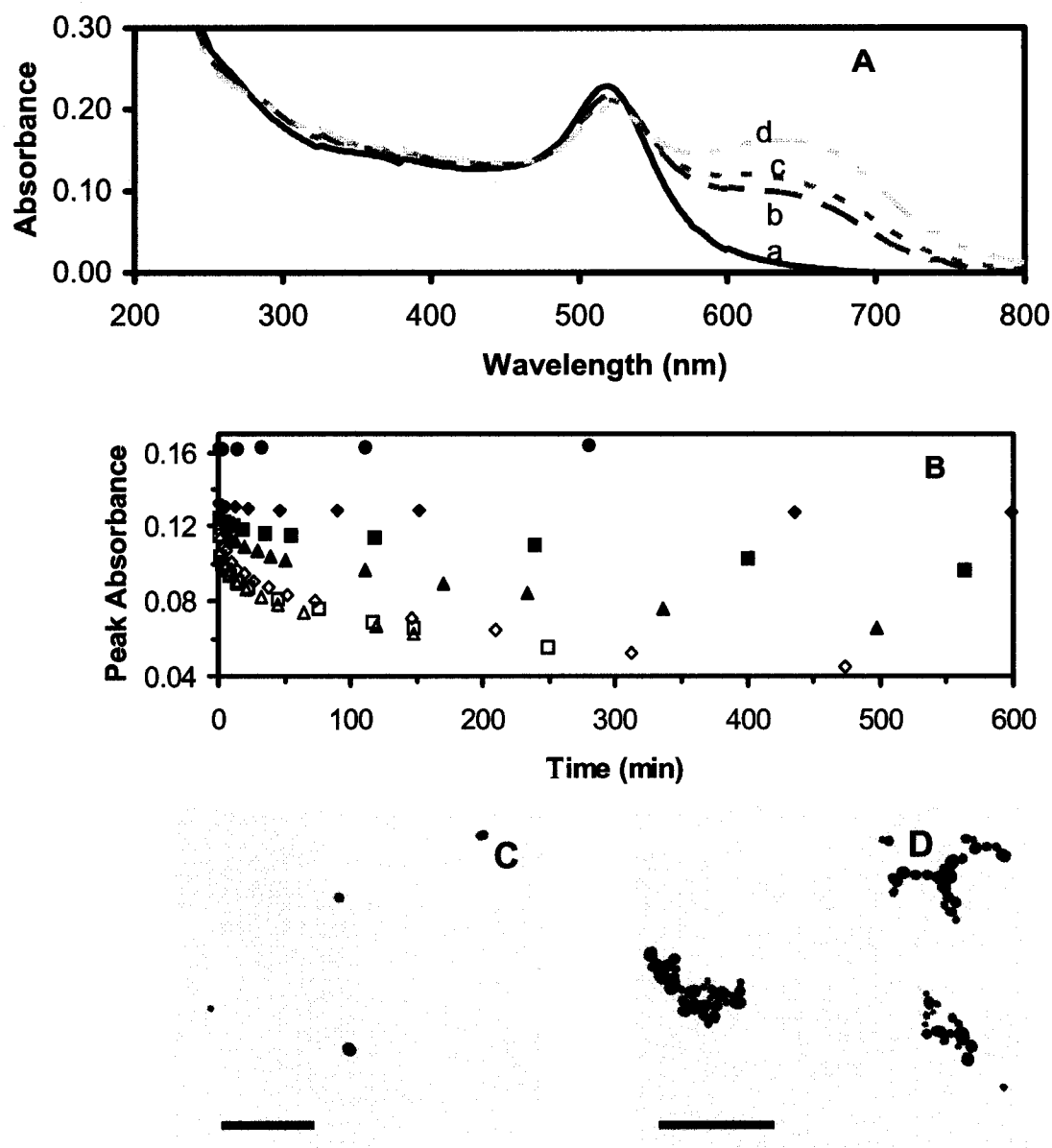


FIGURE 6. Representative UV-vis absorbance spectra of 0.36 nM Au nanoparticles (19 nm) in the absence and presence of Ru(bpy)₃²⁺ at 24 °C. A, Absorbance spectra are recorded from the Au nanoparticle solutions incubated with 114 nM Ru(bpy)₃²⁺ at (a) 0 min (Au nanoparticles only), (b) 0.33 min, (c) 10.83 min, (d) 163 min; B, Plots of the baseline-subtracted peak absorbance at 524 nm versus time are constructed from the absorbance spectra of Au nanoparticle solutions incubated with Ru(bpy)₃²⁺ concentrations at (♦) 95 nM, (■) 107 nM, (▲) 112 nM, (◇) 114 nM, (□) 119 nM, (Δ) 131 nM, and (●) 524 nM NaCl or MgCl₂. TEM images are acquired from 0.360 nM of the 19 nm Au nanoparticle solutions that have already been incubated with (C) 0 and (D) 107-131 nM Ru(bpy)₃²⁺ for 2 hours. The scale bar represents 137 nm.

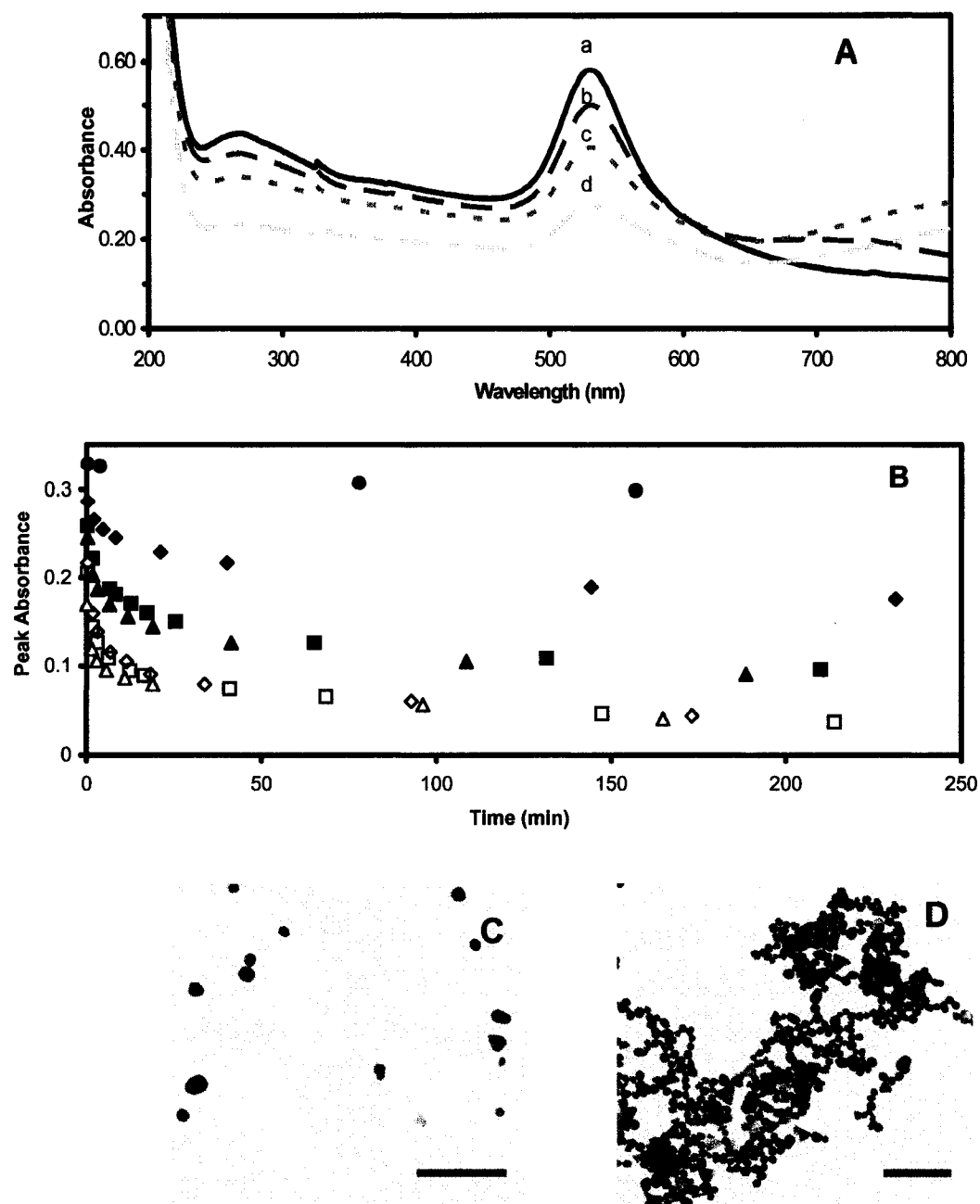


FIGURE 7. Representative UV-vis absorbance spectra of 6 pM Au nanoparticles (48 nm) in the absence and presence of Ru(bpy)₃²⁺ at 24°C. A, Absorbance spectra are recorded from the Au nanoparticle solutions incubated with 83 nM Ru(bpy)₃²⁺ at (a) 0 min, (b) 0.28 min, (c) 8.33 min, (d) 131.5 min; B, Plots of baseline-subtracted peak absorbance at 524 nm versus time are constructed from the Au nanoparticle solution incubated with Ru(bpy)₃²⁺ concentrations at (♦) 76 nM, (■) 83 nM, (▲) 95 nM, (◇) 107 nM, (□) 119 nM, (Δ) 142 nM, and (●) 570 nM NaCl or MgCl₂. TEM images are acquired from 6 pM of the 48 nm Au nanoparticle solutions that have already been incubated with (C) 0 and (D) 107 nM Ru(bpy)₃²⁺ for 2 hours. The scale bar represents 288 nm.

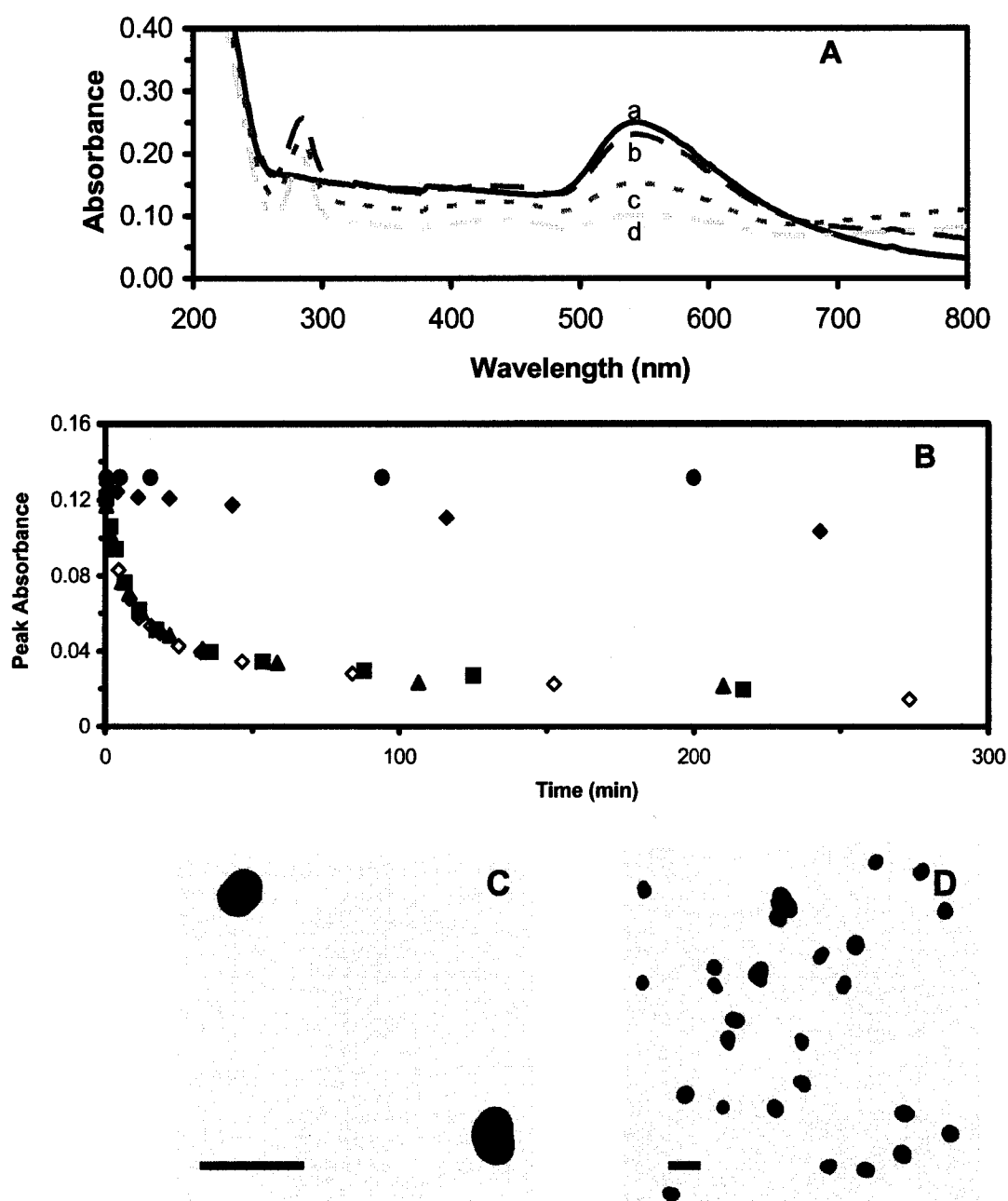


FIGURE 8. Representative UV-vis absorbance spectra of 2 pM Au nanoparticles (97 nm) in the absence and presence of $\text{Ru}(\text{bpy})_3^{2+}$ at 24 °C. A, Absorbance spectra are acquired from the Au nanoparticle solutions incubated with 1.22 μM $\text{Ru}(\text{bpy})_3^{2+}$ at (a) 0 min, (b) 0.27 min, (c) 11.5 min, (d) 125 min; B, Plots of baseline-subtracted peak absorbance at 524 nm versus time are constructed from the Au nanoparticle solutions incubated with $\text{Ru}(\text{bpy})_3^{2+}$ concentration at (\blacklozenge) 1.17 μM , (\blacksquare) 1.22 μM , (\blacktriangle) 1.27 μM , (\diamond) 1.30 μM , and (\bullet) 5.20 μM NaCl or MgCl_2 . TEM images are acquired from 2 pM of the 97 nm Au solutions that have already been incubated with (C) 0 and (D) 1.30 μM $\text{Ru}(\text{bpy})_3^{2+}$ for 2 hours. The scale bar represents 151 nm.

These conduction electrons (surface plasmon) resonate with the incident photon frequency, leading to specific absorbance in a visible range.

The extinction coefficient of 6.5, 19, 48 and 97 nm Au nanoparticles is about 3, 4, 5 and 6 orders of magnitude greater than that of $\text{Ru}(\text{bpy})_3^{2+}$, respectively. Therefore, the absorbance of $\text{Ru}(\text{bpy})_3^{2+}$ at 285 nm ($\epsilon = 1.2 \times 10^5 \text{ M}^{-1} \text{ cm}^{-1}$) and 452 nm ($\epsilon = 1.5 \times 10^4 \text{ M}^{-1} \text{ cm}^{-1}$) in Fig. 5-8 appears not to interfere with the absorbance of Au nanoparticle at 524 nm.

Color-Change Kinetics: Nanoparticle Size and $\text{Ru}(\text{bpy})_3^{2+}$ Concentration Dependence

The Au nanoparticles are surrounded by excess citrate anions, resulting in a negatively charged Au nanoparticle surface. The electrostatic repulsion among the nanoparticles prevents the Au nanoparticles from aggregation. The addition of $\text{Ru}(\text{bpy})_3^{2+}$ into the Au nanoparticles may lead to the color change of Au nanoparticle solution because $\text{Ru}(\text{bpy})_3^{2+}$ is a multi-charged cation and could neutralize the negative charges on the Au nanoparticle surface and decrease the ξ potential on the Au nanoparticle surface. Such a salt effect may bring individual Au nanoparticles into very close contact and hence change the inter-nanoparticle spacing, leading to the inter-nanoparticle plasmon coupling and an additional absorption peak at a longer wavelength beyond 600 nm. Consequently, the color of Au nanoparticle solution would change from pink to blue.

To study whether the color change of Au nanoparticles induced by $\text{Ru}(\text{bpy})_3^{2+}$ depends upon the size of nanoparticles, we select 6.5, 19, 48 and 97 nm Au nanoparticles to determine the minimum (critical) concentration of $\text{Ru}(\text{bpy})_3^{2+}$ that is needed to change the color of Au nanoparticle solutions from pink to blue. The color-change kinetics of Au nanoparticle solutions in the presence of the critical concentration

of $\text{Ru}(\text{bpy})_3^{2+}$ are investigated to understand its dependence upon nanoparticle size. We attempted to prepare the same concentration of different sizes of Au nanoparticles for their titration experiments with $\text{Ru}(\text{bpy})_3^{2+}$. Unfortunately, it was impossible to perform the experiment using the same concentration of the different-size Au nanoparticles because 0.36 nM of the 97 nm Au nanoparticles tended to aggregate. In addition to aggregation, differences in extinction coefficients for the different sized particles made it impossible to use a single concentration of nanoparticles. Therefore, 2.13 nM, 0.36 nM, 6 pM and 2 pM of 6.5, 19, 48 and 97 nm Au nanoparticles were selected to maintain the total surface Au atoms in each Au nanoparticle solution nearly comparable at 7×10^{15} , 1×10^{16} , 1×10^{15} and 2×10^{15} , respectively. The total number of surface Au atoms was calculated by dividing the surface area of all Au nanoparticles ($\pi D^2 NCV$) by the area of an individual Au atom (diameter of Au atom (d_{Au}) = 0.288 nm; area = d_{Au}^2) using a close-pack model. Where D, N, C, and V refers to diameter of an individual Au nanoparticle ($D = 6.5, 19, 48, \text{ and } 97 \text{ nm}$), Avogadro's constant (6.02×10^{23}), molar concentration of Au nanoparticles, and volume of Au nanoparticle solution, respectively.

For the 6.5 nm Au nanoparticles, 2.13 nM Au nanoparticle solutions were titrated with $\text{Ru}(\text{bpy})_3^{2+}$. The absorbance spectra of the Au nanoparticles incubated with 0.142 μM $\text{Ru}(\text{bpy})_3^{2+}$ were recorded over 2 h at 5-min intervals. The spectra remained nearly constant (Fig. 5A). The peak absorbance of the 6.5 nm Au nanoparticles at 519 nm in the absence and presence of $\text{Ru}(\text{bpy})_3^{2+}$ (0-0.142 μM) remained unchanged as shown in Fig. 5B, indicating that the color of Au nanoparticle solution remains unchanged over time. TEM images of Au nanoparticles that have already been incubated with 0 and 0.142 μM $\text{Ru}(\text{bpy})_3^{2+}$ for 2 h demonstrate that individual Au nanoparticles are well isolated as illustrated in Fig. 5C and 5D. This result suggests that 0.142 μM $\text{Ru}(\text{bpy})_3^{2+}$

is unable to cause the aggregation of 6.5 nm Au nanoparticles (2.13 nM). Increasing the titration concentration of $\text{Ru}(\text{bpy})_3^{2+}$ up to 1.3 μM left the peak absorbance (color) of the Au nanoparticle solution unchanged. The absorbance of 1.3 μM $\text{Ru}(\text{bpy})_3^{2+}$ at 452 nm appeared to interfere with the measurement of Au nanoparticle absorbance at 519 nm, which prevented higher concentrations of $\text{Ru}(\text{bpy})_3^{2+}$ from being used in the titration experiment.

To determine whether the salt effect (neutralization of surface charges of Au nanoparticles) leads to the color-change of the Au nanoparticles, 568 nM NaCl and MgCl_2 were incubated with 2.13 nM of 6.5 nm Au nanoparticles and the spectra of the Au nanoparticle solutions were recorded over 2 hours. Plots of peak absorbance of the Au nanoparticles versus time indicated that the peak absorbance remained constant, showing neither 568 nM NaCl nor MgCl_2 can cause the color change of the 6.5 nm Au nanoparticle. TEM images of the Au nanoparticle solution containing 568 nM NaCl or MgCl_2 were the same as presented in Fig. 5C and 5D, indicating that the Au nanoparticles did not aggregate in the presence of 568 nM NaCl or MgCl_2 .

For the 19 nm Au nanoparticles, 0.36 nM Au nanoparticle solutions are titrated by $\text{Ru}(\text{bpy})_3^{2+}$. Concentrations of $\text{Ru}(\text{bpy})_3^{2+}$ greater than 107 nM changed the color of Au nanoparticles from pink to blue. The absorbance spectra of the 0.36 nM Au nanoparticles incubated with 114 nM $\text{Ru}(\text{bpy})_3^{2+}$ were recorded over 2 hours and showed that the absorbance (524 nm) of Au nanoparticles decreased over time as a broader absorbance peak at a longer wavelength (650 nm) appeared and increased with time (Fig. 6A). In contrast, the peak absorbance of the 19 nm Au nanoparticles at 524 nm in presence of lower concentrations of $\text{Ru}(\text{bpy})_3^{2+}$ (0-95 nM) remained unchanged as shown in Fig. 6B. Taken together, the results in Fig. 6B show that the peak absorbance

of 0.36 nM of 19 nm Au nanoparticles decreased with time in the presence of $\text{Ru}(\text{bpy})_3^{2+}$ concentrations, 107, 112, 114, 119, and 131 nM. A minimum (critical) concentration of 107 nM $\text{Ru}(\text{bpy})_3^{2+}$ was needed to change the color of the Au nanoparticles at room temperature.

The results in Fig. 6B also indicated that the rate of decreased absorbance (color change) of Au nanoparticles was highly sensitive to $\text{Ru}(\text{bpy})_3^{2+}$ concentration. For example, the absorbance of Au nanoparticles in the presence of 95 nM $\text{Ru}(\text{bpy})_3^{2+}$ remains constant, while the absorbance of the Au nanoparticles in the presence of 107 nM $\text{Ru}(\text{bpy})_3^{2+}$ decreased with time at a rate of $4.9 \times 10^{-4} \text{ min}^{-1}$ and reached equilibrium at an absorbance of 0.1285. As $\text{Ru}(\text{bpy})_3^{2+}$ concentration increased to 131 nM, the absorbance of Au nanoparticles decreased at the rate of $5.7 \times 10^{-3} \text{ min}^{-1}$ and reached equilibrium at an absorbance of 0.056. The slopes of peak absorbance of Au nanoparticles versus time in the presence of 112 and 114 nM $\text{Ru}(\text{bpy})_3^{2+}$ were clearly distinguished with rates of $9.8 \times 10^{-4} \text{ min}^{-1}$ and $2.5 \times 10^{-3} \text{ min}^{-1}$, respectively (Fig. 6B). The color-change rate was highly sensitive to the quantity of $\text{Ru}(\text{bpy})_3^{2+}$ and the colorimetric method could be used to differentiate as little as 7 pmol of $\text{Ru}(\text{bpy})_3^{2+}$ in the Au solution [(114-112) nM = 2 nM in 3.5 mL solution; $2 \text{ nM} \times 3.5 \text{ mL} = 7 \text{ pmol}$] (Fig. 6B).

TEM images acquired from the Au nanoparticle solutions that had been incubated with 0 and 131 nM $\text{Ru}(\text{bpy})_3^{2+}$ for 2 h showed that the individual nanoparticles were well isolated in the absence of $\text{Ru}(\text{bpy})_3^{2+}$ and became coagulated in the presence of 131 nM $\text{Ru}(\text{bpy})_3^{2+}$, suggesting that the color change of Au nanoparticles was attributable to the aggregation of Au nanoparticles.

To determine whether the color change of 19 nm Au nanoparticle solution induced by $\text{Ru}(\text{bpy})_3^{2+}$ was solely contributed by the salt effect of $\text{Ru}(\text{bpy})_3^{2+}$, the 0.360

nM Au nanoparticle solution was incubated with 524 nM NaCl or MgCl_2 , a concentration 4-fold higher than the critical concentration of $\text{Ru}(\text{bpy})_3^{2+}$. The spectra of the Au nanoparticle solution containing 524 nM NaCl or MgCl_2 were recorded over 2 hours. Plots of baseline-subtracted peak absorbance of Au nanoparticles versus time showed that the peak absorbance remained constant, indicating that neither 524 nM NaCl nor MgCl_2 changed the color of the Au nanoparticles (Fig. 6B). TEM images of the 0.360 nM Au nanoparticle solutions incubated with 524 nM NaCl or MgCl_2 for 2 hours were similar to those observed in Fig. 6C, showing that the individual Au nanoparticles were well isolated. This experiment suggested that the salt effect of $\text{Ru}(\text{bpy})_3^{2+}$ was not solely attributable to the aggregation of the nanoparticles. Other factors, such as the adsorption of $\text{Ru}(\text{bpy})_3^{2+}$ on the surface of Au nanoparticles and possible reaction between $\text{Ru}(\text{bpy})_3^{2+}$ and Au nanoparticles, may have played a significant role in changing the color of Au nanoparticle solution.

For the 48 nm Au nanoparticles, 6 pM Au nanoparticle solutions were titrated by $\text{Ru}(\text{bpy})_3^{2+}$ (Fig. 7). The spectra of the 48 nm Au nanoparticles in the presence of 83 nM $\text{Ru}(\text{bpy})_3^{2+}$ showed that the absorbance of the Au nanoparticles at 531 nm decreased with time as a broader absorbance peak beyond 800 nm appeared and increased with time (Fig. 7A). Plots of the baseline-subtracted peak absorbance versus time in Fig. 7B indicated that 83 nM was the critical concentration of $\text{Ru}(\text{bpy})_3^{2+}$ needed to change the color of 6 pM 48 nm Au nanoparticles from pink to blue. The rate of decreased absorbance (color change) at 531 nm was highly dependent upon the quantity of $\text{Ru}(\text{bpy})_3^{2+}$ (Fig. 7B). For instance, the peak absorbance of the 48 nm Au nanoparticle solution containing 76 nM $\text{Ru}(\text{bpy})_3^{2+}$ decreased with time gradually at the rate of $7 \times 10^{-3} \text{ min}^{-1}$ and reached equilibrium at an absorbance of 0.1757, while the absorbance of 48

nm Au nanoparticles in the presence of 83 nM $\text{Ru}(\text{bpy})_3^{2+}$ decreased at the rate of $1 \times 10^{-2} \text{ min}^{-1}$ and reached equilibrium at an absorbance of 0.096. TEM images of the 48 nm Au nanoparticle solutions in the absence and presence of $\text{Ru}(\text{bpy})_3^{2+}$ (0, 107 nM) in Fig. 7C and 7D indicated that the individual Au nanoparticles were well isolated in the absence of $\text{Ru}(\text{bpy})_3^{2+}$ and became aggregated in the presence of 107 nM $\text{Ru}(\text{bpy})_3^{2+}$. This suggested that the coagulation of Au nanoparticles was indeed involved in the color change of Au nanoparticle solution. The control experiment was carried out by incubation of 6 pM of the 48 nm Au nanoparticles with 570 nM NaCl or MgCl_2 (4-fold higher than the critical concentration of $\text{Ru}(\text{bpy})_3^{2+}$) and there was no color change of the Au nanoparticle solution. TEM images of the 48 nm Au nanoparticle solutions incubated with 570 nM NaCl or MgCl_2 for 2 hours were similar to those observed in the absence of $\text{Ru}(\text{bpy})_3^{2+}$ (Fig. 7C). As similarly observed with the 19 nm Au nanoparticles, the TEM images demonstrated that the color change of the 48 nm Au nanoparticle solution by $\text{Ru}(\text{bpy})_3^{2+}$ was not solely attributable to the salt-effect.

Using the same approach, the color change of the 97 nm Au nanoparticles (2 pM) induced by $\text{Ru}(\text{bpy})_3^{2+}$ was investigated (Fig. 8). The spectra of the 97 nm Au nanoparticles in the presence of 1.22 μM $\text{Ru}(\text{bpy})_3^{2+}$ in Fig. 8A show that the peak absorbance (545 nm) of the 97 nm Au nanoparticles decreased with time as a broader peak at a long wavelength beyond 800 nm appeared and increased with time. In this experiment, a higher concentration (1.22 μM) of $\text{Ru}(\text{bpy})_3^{2+}$ is used. Therefore, the absorbance of $\text{Ru}(\text{bpy})_3^{2+}$ at 281 nm and 452 nm was also observed (Fig. 8A: b). The absorbance of the Au nanoparticle solution decreased with time, lowering the baseline of absorption spectra of Au nanoparticles. The peak absorbance of 1.22 μM $\text{Ru}(\text{bpy})_3^{2+}$ at

281 nm and 452 nm remained relatively constant suggesting that the quantity of $\text{Ru}(\text{bpy})_3^{2+}$ remained unchanged over the incubation time.

Note that the large Au nanoparticles (97 nm) created a slightly higher absorbance baseline than the small nanoparticles (Fig. 5A-8A), owing to that Mie scattering of Au nanoparticles increased proportionally as the volume of nanoparticles increased. The larger nanoparticles (97 nm) scattered light more effectively than the small nanoparticles. This in turn reduced the transmittance, which lead to the higher absorbance baseline. The peak absorbance of the Au nanoparticles in Fig. 5B-8B has been corrected by its baseline absorbance. The change in baseline-subtracted peak absorbance was used to measure the color-change rate of the Au nanoparticles.

As observed with the 19 and 48 nm Au nanoparticle solutions, plots of baseline-subtracted peak absorbance of 97 nm Au (2 pM) nanoparticles solutions containing 1.17, 1.22, 1.27, and 1.30 μM $\text{Ru}(\text{bpy})_3^{2+}$ versus time in Fig. 8B indicated that the rate of decreased absorbance (color change) of Au nanoparticles was highly dependent upon the amount of $\text{Ru}(\text{bpy})_3^{2+}$ present. Using 1.17 μM $\text{Ru}(\text{bpy})_3^{2+}$, the peak absorbance of the 97 nm Au nanoparticle solution at 545 nm decreased with time at a rate of $1 \times 10^{-3} \text{ min}^{-1}$ and reached equilibrium at an absorbance of 0.104. In contrast, the absorbance of Au nanoparticles decreased in the presence of 1.22 μM $\text{Ru}(\text{bpy})_3^{2+}$ at a rate of $7 \times 10^{-3} \text{ min}^{-1}$ and reached equilibrium at an absorbance of 0.012. The critical concentration of $\text{Ru}(\text{bpy})_3^{2+}$ for the color change of 2 pM of the 97 nm Au nanoparticles was 1.17 μM . TEM images of the 97 nm Au nanoparticles (2 pM) in the absence and presence of $\text{Ru}(\text{bpy})_3^{2+}$ (0, 1.30 μM) in Fig. 8C and 8D showed that the individual Au nanoparticles were well isolated in the absence of $\text{Ru}(\text{bpy})_3^{2+}$ and only a very few of nanoparticles interacted with each other after incubation with 1.30 μM $\text{Ru}(\text{bpy})_3^{2+}$ for 2 hours. The

result suggested that the coagulation of Au nanoparticles is not a sole factor that caused the color change of the 97 nm Au nanoparticles. The control experiment was performed by incubating 2 pM of the 97 nm Au nanoparticles with 5.2 μM NaCl and MgCl_2 , a concentration 4-fold higher than the critical concentration of $\text{Ru}(\text{bpy})_3^{2+}$, and showed that the peak absorbance of the 97 nm Au nanoparticle solution remained constant (Fig. 8B) and the color of the Au nanoparticle solution was unchanged. TEM images of the 97 nm Au nanoparticle solution incubated with 5.2 μM NaCl or MgCl_2 for 2 hours were similar to those observed in the absence of $\text{Ru}(\text{bpy})_3^{2+}$ and showed the well-isolated individual Au nanoparticles (Fig. 8C). Once again demonstrating, the salt effect did not play a major role in changing the color of the 97 nm Au nanoparticle solution.

Taken together, the results indicated that the color-change kinetics of the Au nanoparticles induced by $\text{Ru}(\text{bpy})_3^{2+}$ was highly dependent upon the size of nanoparticles and $\text{Ru}(\text{bpy})_3^{2+}$ concentration. The critical concentrations of $\text{Ru}(\text{bpy})_3^{2+}$ needed for color change of the Au solutions of different nanoparticle sizes, the number of surface Au atoms of the individual nanoparticle, and the total surface Au atoms of all nanoparticles in the solution are summarized in Table II. It appeared that the larger the Au nanoparticle, the higher the molar ratio of $\text{Ru}(\text{bpy})_3^{2+}$ to Au nanoparticle was required to change the color of solution. For instance, the minimum molar ratio of $\text{Ru}(\text{bpy})_3^{2+}$ needed to change the color of the 19 nm, 48 nm and 97 nm Au nanoparticles were 3.0×10^2 , 1.4×10^4 and 6.0×10^5 respectively. By comparing the molar ratio of $\text{Ru}(\text{bpy})_3^{2+}$ to the Au nanoparticles (number of $\text{Ru}(\text{bpy})_3^{2+}$ molecules per Au nanoparticle) with the theoretically calculated monolayer of $\text{Ru}(\text{bpy})_3^{2+}$ molecules adsorbed on the surface of the individual nanoparticle, we found that more than a monolayer of $\text{Ru}(\text{bpy})_3^{2+}$ was required to change the color of the 97 nm Au

nanoparticles, whereas less than a monolayer of $\text{Ru}(\text{bpy})_3^{2+}$ was needed to change the color of the 19 nm and 48 nm Au nanoparticles.

The molar ratio of $\text{Ru}(\text{bpy})_3^{2+}$ to the surface Au atoms of the individual 48 nm Au nanoparticle (2×10^9) was 10-fold lower than that of the individual 19 nm Au nanoparticle (2×10^{10}). Note that the surface Au atoms of the individual 48 nm Au nanoparticle (9×10^4) was about 10-fold higher than that of the individual 19 nm Au nanoparticle (1×10^4). The molar ratio of $\text{Ru}(\text{bpy})_3^{2+}$ to the total surface Au atoms of all 48 nm Au nanoparticles in the solution (0.2) was 10-fold higher than that of all 19 nm Au nanoparticles (0.02). Note that the total surface Au atoms of the 48 nm Au nanoparticles (1.1×10^{15}) were 10-fold lower than that of the 19 nm Au nanoparticles (1.0×10^{16}).

These results showed that the critical concentration of $\text{Ru}(\text{bpy})_3^{2+}$ needed to change the color of the 19, 48 and 97 nm Au nanoparticle solutions was highly associated with the number of surface Au atoms of the individual nanoparticles and the total number of Au atoms of all nanoparticles in the solution. This association further suggested that the color-change mechanism of the Au nanoparticles induced by $\text{Ru}(\text{bpy})_3^{2+}$ may have involved the adsorption of $\text{Ru}(\text{bpy})_3^{2+}$ on the surface of Au nanoparticles. The relatively constant absorbance peak of $\text{Ru}(\text{bpy})_3^{2+}$ observed in the 97 nm nanoparticle experiments (Fig. 8A) indicated that any adsorption of $\text{Ru}(\text{bpy})_3^{2+}$ was a physical rather than chemical phenomena.

Color Change Kinetics: Temperature-Dependence

The measurements in Fig. 5-8 were carried out at the room temperature ($\sim 24^\circ\text{C}$). While conducting the previous experiments, we noticed that the critical concentration of

TABLE 2

The minimum concentrations of $\text{Ru}(\text{bpy})_3^{2+}$ needed for the color change of Au nanoparticle solutions

Diameter of Au nanoparticle (nm)	6.5 ± 1.5	18.6 ± 3.5	48.1 ± 5.8	96.7 ± 15.4
C, Au nanoparticle (pM)	2.13×10^3	3.60×10^2	6	2
Surface Au atoms per nanoparticle*	2×10^3	1×10^4	9×10^4	4×10^5
Total surface Au atoms of all nanoparticles in the solution	7×10^{15}	1×10^{16}	1×10^{15}	2×10^{15}
C, $\text{Ru}(\text{bpy})_3^{2+}$ (nM) †	/	107	83	1170
Molar Ratio, $\text{Ru}(\text{bpy})_3^{2+}$ /Au nanoparticle = number of $\text{Ru}(\text{bpy})_3^{2+}$ molecules per Au nanoparticle	/	3.0×10^2	1.4×10^4	6.0×10^5
Molar Ratio, $\text{Ru}(\text{bpy})_3^{2+}$ /surface Au atoms of a nanoparticle	/	2×10^{10}	2×10^9	7×10^9
Molar Ratio, $\text{Ru}(\text{bpy})_3^{2+}$ /total surface Au atoms	/	0.02	0.2	2
Maximum adsorbed $\text{Ru}(\text{bpy})_3^{2+}$ per nanoparticle (molecules)#	79	8×10^2	4×10^3	2×10^4

* The surface Au atoms of an individual Au nanoparticle are calculated by dividing the surface area of an individual Au nanoparticle (πD^2) with the area of an individual Au atom (diameter of Au atom (d_{Au}) = 0.288 nm; area = d_{Au}^2) using a close-pack model. $D = 6.5, 19, 48$ and 97 nm.

The total number of surface Au atoms is calculated by dividing the surface area of all Au nanoparticles ($\pi D^2 NCV$) in the solution with the area of an individual Au atom (diameter of Au atom (d_{Au}) = 0.288 nm; area = d_{Au}^2) using a close-pack model. Where D , N , C , and V refer to diameter of Au nanoparticles (6.5, 19, 48 and 97 nm), Avogadro's constant (6.02×10^{23}), concentration of the Au nanoparticles, and volume of Au nanoparticle solution, respectively.

† The minimum concentration of $\text{Ru}(\text{bpy})_3^{2+}$ needed to change the color of the Au nanoparticle solutions is determined experimentally as shown in Fig. 1-4.

The maximum number of a monolayer of $\text{Ru}(\text{bpy})_3^{2+}$ molecules adsorbed on the surface of an individual Au nanoparticle ($D = 6.5, 19, 48$, and 97 nm) is theoretically calculated by dividing the surface area of an individual Au nanoparticle (πD^2) with the area of an individual $\text{Ru}(\text{bpy})_3^{2+}$ molecule (diameter of $\text{Ru}(\text{bpy})_3^{2+}$ molecules (d) = 1.3 nm; area = d^2) using a close-pack model.

$\text{Ru}(\text{bpy})_3^{2+}$ for the color change of Au nanoparticles was highly sensitive to the temperature and varied slightly over fluctuations of the room temperature. Two

representative sizes of Au nanoparticles, 19 nm and 48 nm, were selected to investigate whether the color change temperature-dependence of the Au nanoparticles was associated with the size of nanoparticles. Three temperatures, 24.0 °C, 33.0 °C and 51.0 °C, were chosen to study the temperature-dependence of the Au nanoparticles color-change kinetics. The Au nanoparticle solutions were incubated with the previously determined critical concentrations of $\text{Ru}(\text{bpy})_3^{2+}$ at constant temperature (24.0 °C, 33.0 °C or 51.0 °C) and the spectra of the Au nanoparticle solutions were recorded over 2 h. Plots of the peak absorbance of Au nanoparticle solutions containing the critical concentration of $\text{Ru}(\text{bpy})_3^{2+}$ versus time at 24.0 °C, 33.0 °C and 51.0 °C (Fig. 9) showed that the rate of color change of Au nanoparticles induced by $\text{Ru}(\text{bpy})_3^{2+}$ was highly dependent upon the temperature.

In the presence of the critical concentration of $\text{Ru}(\text{bpy})_3^{2+}$, the rate of decreased absorbance (color change) of Au nanoparticles was sensitive to both the temperature and size of nanoparticles. In Fig. 9A, no significant color change was observed over 2 hours as the 19 nm Au nanoparticle solution (0.36 nM) was incubated with 0.107 μM $\text{Ru}(\text{bpy})_3^{2+}$ at 24.0 °C. As the temperature of solution was increased to 33.0 °C, the pink color of the Au nanoparticle solution vanished and turned light blue within 20 min of incubation time (Fig. 10A). Once the color changed from pink to blue, the reaction became an irreversible process. The similar phenomenon was observed at 51.0 °C with 2-fold and 8-fold higher reaction rate than at 33.0 °C and 24.0 °C, respectively. A control experiment was performed by incubating the Au nanoparticles with 524 nM NaCl or MgCl_2 , a 4-fold higher concentration than the critical concentration of $\text{Ru}(\text{bpy})_3^{2+}$, for 2 hours; no color change was observed at any temperature

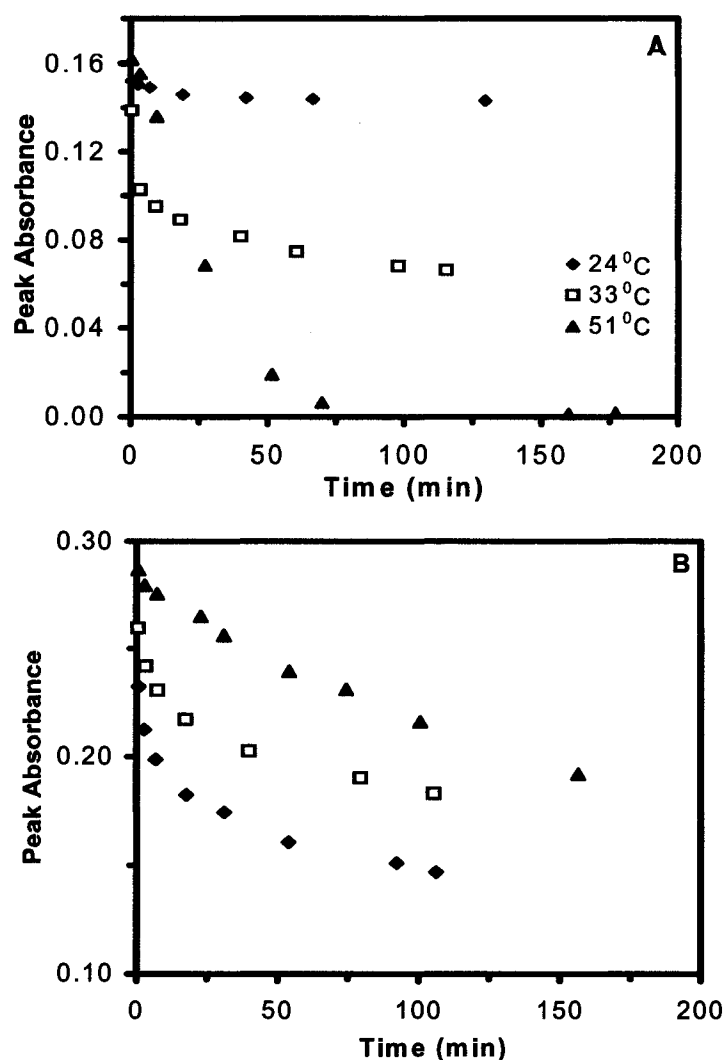


FIGURE 9. Representative plots of baseline-subtracted peak absorbance at 524 nm versus incubation time are constructed from the absorbance spectra of the solution. A, 0.360 nM of the 19 nm Au nanoparticle solution containing 107 nM $\text{Ru}(\text{bpy})_3^{2+}$ at (◆) 24.0°C, (□) 33.0°C, (▲) 51.0°C. B, 6 pM of the 48 nm Au nanoparticle solution containing 76 nM $\text{Ru}(\text{bpy})_3^{2+}$ at (◆) 24.0°C, (□) 33.0°C, (▲) 51.0°C.

(24.0 - 51.0 °C). UV-vis absorbance spectra of the $\text{Ru}(\text{bpy})_3^{2+}$ solution in the absence of Au nanoparticles at 24.0 - 51.0 °C were measured. The results indicated no change of $\text{Ru}(\text{bpy})_3^{2+}$ absorbance and further confirmed the chemical stability of $\text{Ru}(\text{bpy})_3^{2+}$.

In contrast to the results of the 19 nm Au nanoparticles, the surface plasmon absorbance of the 48 nm Au nanoparticle solution in the presence of the critical concentration (76 nM) of $\text{Ru}(\text{bpy})_3^{2+}$ decreased most rapidly at the lower temperature (Fig. 9B).

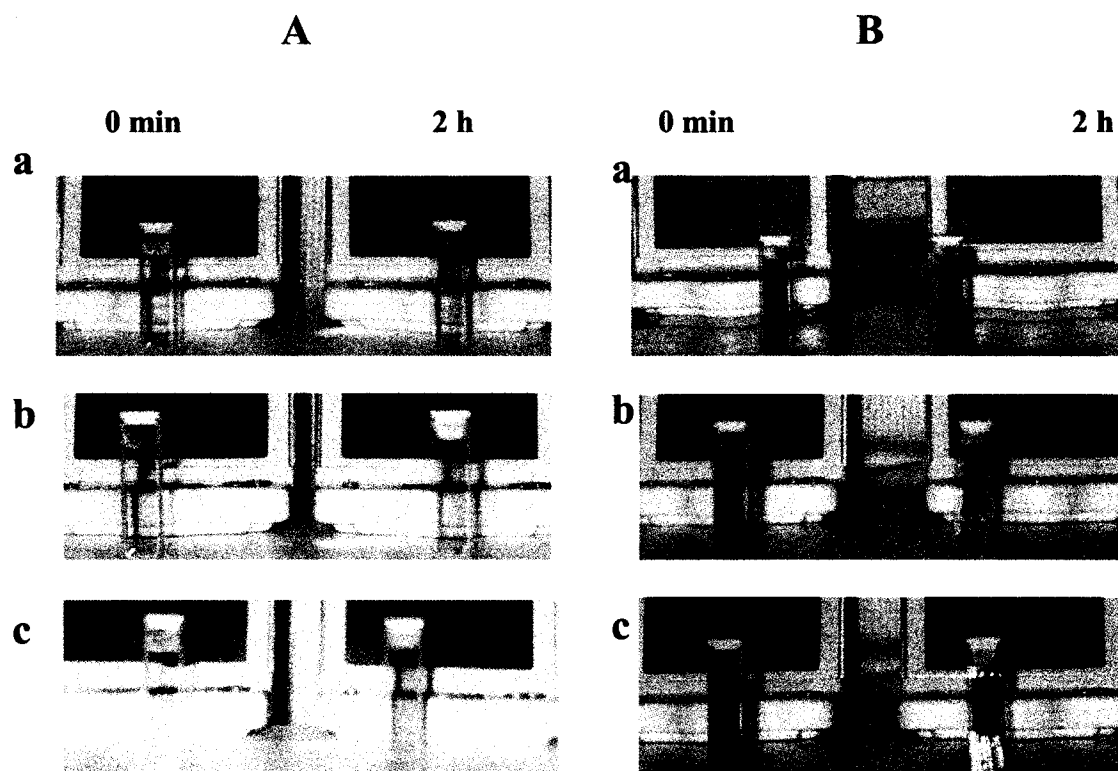


FIGURE 10. Representative color photos of the Au nanoparticle solutions are acquired from experiments in FIG. 9, showing temperature-dependence. A, The 19 nm Au nanoparticles (0.360 nM) before (0 min) (left) and after incubated with 107 nM $\text{Ru}(\text{bpy})_3^{2+}$ for 2 hours (right) at (a) 24.0°C, (b) 33.0°C, (c) 51.0°C. B, The 48 nm Au nanoparticles (6 pM) before (0 min) (left) and after incubated with 76 nM $\text{Ru}(\text{bpy})_3^{2+}$ for 2 hours (right) at (a) 24.0°C, (b) 33.0°C, (c) 51.0°C.

At 24.0 °C, the rate of change was 3-fold higher at than at 51.0 °C. This result suggested that the reaction rate decreased as temperature increased. The Au nanoparticle solution containing 76 nM $\text{Ru}(\text{bpy})_3^{2+}$ remained its original pink color at 33.0 and 51.0 °C for 2 h (Fig. 10B). Control experiments were performed by incubating

the Au nanoparticles with 5.2 μM NaCl or MgCl_2 concentration (4-fold higher than the critical concentration of $\text{Ru}(\text{bpy})_3^{2+}$) for 2 hours; no color change was observed at any temperature (24.0-51.0 $^\circ\text{C}$). The refractive index of water changes with temperature, which may have caused a blue shift and lower plasmon absorption of Au nanoparticles. Such a phenomenon may have obscured our observation of true temperature-dependence of the surface plasmon absorption of Au nanoparticles. To rule out such possibility, a control experiment in the absence of $\text{Ru}(\text{bpy})_3^{2+}$, demonstrated that the plasmon absorption of the 19 nm and 48 nm Au nanoparticles remained unchanged at 24.0-51.0 $^\circ\text{C}$. The other control experiment was performed by incubating the Au nanoparticles with a 4-10 fold higher concentration of NaCl or MgCl_2 than the critical concentration of $\text{Ru}(\text{bpy})_3^{2+}$. As previously mentioned, no color change of the Au nanoparticles was observed at 24.0-51.0 $^\circ\text{C}$. These results confirmed that the observed temperature-dependence of the color change of Au nanoparticles shown in Fig. 9 and 10 was not attributable to the changes in the refractive index of water.

Taken together, the results in Fig. 9 showed that the rate of color-change induced by $\text{Ru}(\text{bpy})_3^{2+}$ is highly dependent upon both the temperature and nanoparticle size. Based upon kinetic theory, as temperature increases, the rate of $\text{Ru}(\text{bpy})_3^{2+}$ adsorbed on the Au nanoparticle surface decreases whereas the rate of $\text{Ru}(\text{bpy})_3^{2+}$ neutralizing the surface charges of Au nanoparticles increases. The former decreases the color-change rate of Au nanoparticle solution. In contrast, the latter accelerates the color-change kinetics. For the smaller Au nanoparticles (19 nm in diameter), as temperature increased, the rate of surface charges of Au nanoparticles neutralized by $\text{Ru}(\text{bpy})_3^{2+}$ increased much more rapidly than the rate of $\text{Ru}(\text{bpy})_3^{2+}$ adsorbed on the Au nanoparticle surface decreased. Individual smaller nanoparticles (19 nm) have smaller

surface area and less negative charges than individual larger nanoparticles (48 nm). Thus, the salt effect (neutralization of surface charges of nanoparticles) for the smaller nanoparticles was more sensitive to the temperature change and played a more pronounced role in changing the surface plasmon absorption of Au nanoparticles. Consequently, the color-change rate of the 19 nm Au nanoparticles increased as temperature increased.

In contrast, for the larger nanoparticles (48 nm), as temperature increased, the rate of $\text{Ru}(\text{bpy})_3^{2+}$ adsorbed on the surface of Au nanoparticles decreased more significantly than the increased rate of neutralization of surface charges of nanoparticles by $\text{Ru}(\text{bpy})_3^{2+}$ (salt effect). The adsorption effect was the dominant mechanism and played a leading role in changing the color of the 48 nm Au nanoparticles. As a result, the color-change rate of the 48 nm Au nanoparticles decreased as temperature increased.

These plausible explanations may help to understand why the results from this study appear different from the reported findings and proposed models, which described the small temperature-dependence of surface plasmon absorbance (color) of colloidal Au nanoparticles and the smaller temperature-dependence of the larger Au nanoparticles. According to the chemical interface-damping model, Fermi distribution of electrons varies with temperature. The higher temperature leads to the larger population of the higher electronic states, which can undergo a charge transfer into the acceptor level (66). This model and previous studies show that the temperature-dependence of surface plasmon absorption of Au nanoparticles is very small and nearly negligible.

In this study, in the presence of the critical concentration of $\text{Ru}(\text{bpy})_3^{2+}$, we found that the surface plasmon absorption of Au nanoparticles showed astonishingly high dependence upon temperature, indicating that the plasmon absorbance of the Au

nanoparticles decreased more rapidly at the higher temperature for the 19 nm Au nanoparticles (8-fold higher at 51.0 °C than at 24.0 °C) (Fig. 9A), whereas the absorbance of the Au nanoparticles decreased more rapidly at the lower temperature for the 48 nm Au nanoparticles (3-fold higher at 24.0 °C than at 51.0 °C). The strikingly high temperature dependence suggests that other mechanisms, such as adsorption and desorption of $\text{Ru}(\text{bpy})_3^{2+}$ from the Au nanoparticle surface, chemical reaction of $\text{Ru}(\text{bpy})_3^{2+}$ with the surface Au atoms or charge transfer between ligand, tris(2,2'-bipyridine), with surface plasmon, may be involved in changing the color of Au nanoparticles. This study provides new insights into the size-dependence and temperature-dependence of surface plasmon absorption of Au nanoparticles in the presence of surface adsorbates, demonstrating a new approach for the color change of Au nanoparticle solution using temperature and surface adsorbates.

Even though the absorbance of $\text{Ru}(\text{bpy})_3^{2+}$ in Fig. 8A indicates that $\text{Ru}(\text{bpy})_3^{2+}$ remains constant over incubation time, such measurement of $\text{Ru}(\text{bpy})_3^{2+}$ is limited by the detection limit of Uv-vis absorbance spectroscopy. Therefore, we have not yet completely eliminated the possibility of chemical reaction between $\text{Ru}(\text{bpy})_3^{2+}$ with the Au nanoparticles.

CHAPTER III

DIRECT MEASUREMENTS OF MEMBRANE PERMEABILITY AND MULTI-DRUG RESISTANCE OF *P. AERUGINOSA* USING SINGLE NANOPARTICLE OPTICS

INTRODUCTION

Bacteria, such as *P. aeruginosa*, have emerged to be a major opportunistic human pathogen and the leading cause of nosocomial infections in cancer, transplantation, burn and cystic fibrosis patients. These infections are impossible to eradicate in part because of its intrinsic resistance to a wide spectra of structurally and functionally unrelated antibiotics (67 - 68). To effectively treat bacterial infections and prevent bacteria from developing multi-antibiotics resistance, the main strategy is to fully understand multi-drug resistance (MDR) mechanism and carefully design and screen more efficacious new antibiotics. Recent studies have revealed that the intrinsic resistance in gram-negative bacteria such as *P. aeruginosa* was attributable to a synergy of low outer membrane permeability and active drug extrusion. Several efflux systems including MexAB-OprM, MexCD-OprJ, MexEF-OprN and MexXY-OprM, have been reported in *P. aeruginosa*. The MexAB-OprM pump is the major efflux pump in wild-type (WT) cells. This pump consists of two inner membrane proteins (MexA and MexB) and one outer membrane protein (OprM) (69). The MexB protein is believed to extrude the xenobiotics utilizing the proton motive force as the energy source. Despite extensive research over decades, the mechanisms of MDR are not yet completely understood.

Most methods used for the study of bacterial MDR mechanisms measure the accumulation of quinolone antibiotics in bacteria using radioactively labeled (^{14}C and ^3H) quinolones or naturally fluorescent quinolones. Given that a common characteristic of MDR of bacteria is their broad resistance to quinolones, the popular method for assessing MDR is the measurement of time courses of fluorescence intensity of quinolones in the cells. Time courses of fluorescence intensity of quinolones (e.g., ethidium bromide) have been widely used for real-time monitoring of the accumulation of substrates in bulk bacterial cells (70). This approach provides the average kinetics from a large population of cells. Individual cells, however, act independently and have unsynchronized membrane permeability, efflux pump machinery and accumulation kinetics. Thus, it is possible that the true accumulation kinetics of an individual cell is buried in such an ensemble average measurement (71-72). For example, if the uptake and efflux kinetics of substrates by individual cells are vastly different from each other, such information would be lost in bulk measurement. Furthermore, this approach does not provide size information about the transformation of membrane pores of intact cells. Hence, current approaches are unable to address several important questions about when and where the substrates induce the transformation of membrane permeability and efflux machinery that lead to the MDR.

Many quantitative and qualitative methods have been developed to study resistance levels of bacteria. The most common techniques for testing the susceptibility of bacteria to antibiotics are broth dilution and agar plate techniques (73). Both methods are used to determine the minimum inhibitory concentration (MIC) of antibiotics toward bacteria. Other techniques including the efficacy time index assay (74), time-kill analysis, double-disc synergy test, inhibitor-potentiated disc diffusion test, three-

dimensional test, and PCR-Nhe I test, have been used to measure MIC and determine the susceptibility of bacteria (75). There is a range of specificity and sensitivity in these techniques. Some methods give false negative results. In addition, these methods are laborious and time-consuming. Furthermore, these methods cannot offer real-time temporal information for direct observation of the intrinsic resistance mechanism of bacteria, the size transformation of membrane pores, and the inhibitory mechanism of antibiotics in individual live cells. This hinders the further understanding of the modes of action of anti-microbial agents and the rational design of efficacious drugs to treat the infection. Thus, it is critical to develop a real-time screening tool that will provide real-time temporal and size resolution for direct determination of modes of action of anti-microbial agents in individual live cells. Such tools will offer the possibility of discovery of when and where the inhibitory mechanisms occur in live cells and determine the possible regulation pathways.

To this end, we have developed single nanoparticle optical assay and single live cell imaging to study the real-time size-transformation of cell wall and membrane permeability in individual live cells at nanometer (nm) size resolution and millisecond (ms) temporal resolution.

EXPERIMENTAL

Silver Nanoparticle Preparation and Characterization

Silver nanoparticles were prepared by reducing a 500 mL 1 mM AgNO₃ aqueous solution with a fresh 10 mL 1% sodium citrate aqueous solution as described elsewhere (47). All glassware was well cleaned with aqua regia, rinsed with ultrapure water (Nanopore, 18 MΩ), and dried prior to the use. We refluxed a freshly prepared 500 mL of 1 mM AgNO₃ solution in a three-necked round bottom flask. As the solution boiled,

we added 10 mL of a freshly prepared 1% (w/v) sodium citrate aqueous solution to reduce AgNO_3 and generate Ag nanoparticles; this led to a color change of the solution from colorless to greenish-yellow. The solution was refluxed for another hour, cooled to room temperature, and then filtered using a 0.22 μm filter. The Ag nanoparticles were characterized by optical dark-field microscopy and spectroscopy, and transmission electron microscopy (TEM, JEOL 100CX). Samples for TEM imaging were prepared on 100 mesh formvar coated copper grids (Electron Microscopy Sciences). The weight of Ag generated from the complete reduction of AgNO_3 was calculated. The volume of generated Ag was calculated by dividing the weight of generated Ag with silver density (10.49 g/cm^3). The number of Ag nanoparticles (average size 48 nm) in the solution was computed by dividing the volume of generated Ag with the volume of individual Ag nanoparticles. The moles of Ag nanoparticles were determined by dividing the number of Ag nanoparticles with Avogadro's constant (6.02×10^{23}). Ag nanoparticle concentration was then determined as $4 \times 10^{-10} \text{ M}$ by dividing the moles of nanoparticles with volume of the solution.

AZTREONAM EXPERIMENTS

Cell Culture and Preparation

Three strains of *P. aeruginosa*, WT (PAO4290), a wild-type expression level of MexAB-OprM), nalB-1 (TNP030#1), a MexAB-OprM over-expression mutant, and ΔABM (TNP076), a MexAB-OprM deficient mutant, were used (23, 29,76). Cells were pre-cultured in L-broth medium containing 1% tryptone, 0.5% yeast extract, and 0.5% NaCl at pH 7.2 in a shaker (Lab-line Orbit Envivon-Shaker, 150 rpm and 37°C) overnight to ensure the full growth of the cells. Cells were then cultured for an additional 8 hours. Cells were harvested by centrifugation at 7500 rpm (Beckman

Model J2-21 Centrifuge, JA-14 rotor) and 23°C for 10 minutes, washed three times with 50 mM PBS (pH=7.0) and then suspended again in the same buffer with a final adjusted cell concentration of $OD_{600nm}=0.1$ (optical density at 600 nm). Cell solutions (3 mL) containing 1.3 pM Ag nanoparticles and 0, 3.13, 31.3 $\mu\text{g/mL}$ AZT were prepared by mixing 2703 μL of the cell solution ($OD_{600nm}=0.1$) and 9.8 μL of 0.4 nM Ag nanoparticles with ultra-pure water, 187.8 μL of 50 $\mu\text{g/mL}$ AZT, and 187.8 μL of 500 $\mu\text{g/mL}$ AZT, respectively. A timer was started simultaneously to record the incubation time at the mixing point.

Nanoparticle Optics and Single Live Cell Imaging

The dark-field optical microscope was equipped with an oil dark-field condenser (Oil 1.43-1.20, Nikon), a 100x objective (Nikon Plan fluor 100x oil, iris, S.L. N.A. 0.5-1.3, W.D. 0.20 mm), the microscope illuminator (100 W halogen), a CCD camera (Micromax, 5 Mhz Interline, PID 1030x1300, Roper Scientific) for high-speed and high-resolution cell imaging, and a color digital camera (Coolpix 990, Nikon) for real-color imaging. Both cameras were added onto the microscope through a quad-adaptor (Nikon) for real-time imaging. A 20 μL aliquot of the cell solution containing 1.3 pM Ag nanoparticles and AZT (0, 3.13, 31.3 $\mu\text{g/mL}$) was added into a microchannel and directly imaged using dark-field microscope equipped with a CCD camera and color digital camera. The sealed microchannel was constructed by sandwiching the solution between a microscope slide and a cover slip.

RESULTS

Real-Time Imaging of AZT Function Using Nanoparticle Optics

Multicolor Ag nanoparticles were characterized using dark-field microscopy and spectroscopy (Fig. 11A). The color index of single Ag nanoparticles was used to

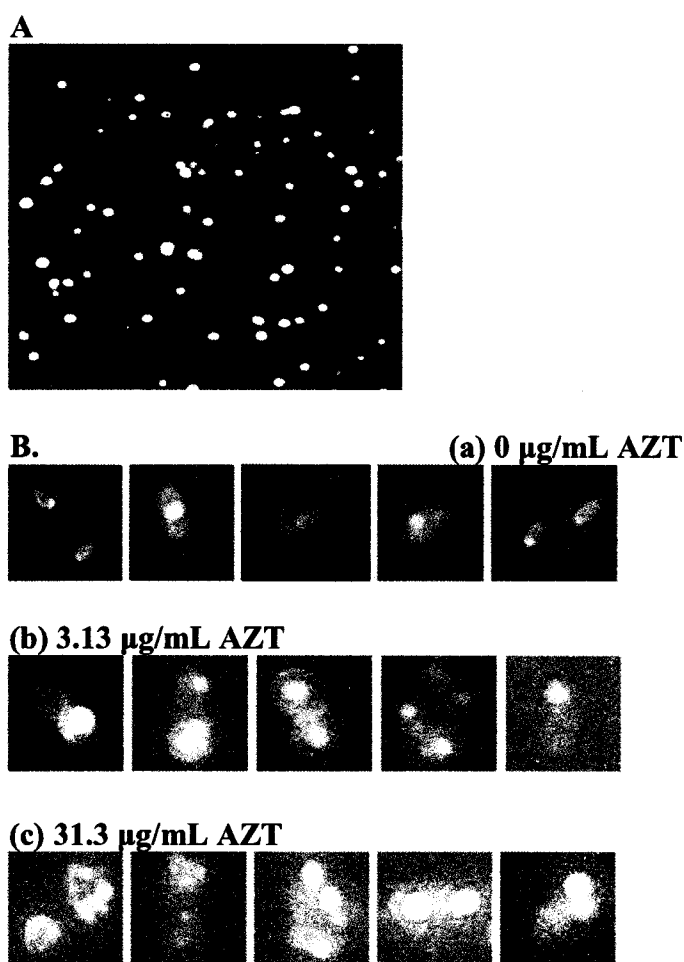


FIGURE 11. Silver Nanoparticles. A, Representative real color optical image of Ag nanoparticles. The image was taken from a 0.4 nM Ag nanoparticle solution in a microchannel by a digital color camera through dark-field optical microscope. B, Direct observation of real-time size transformation of membrane permeability in live cells (nalB-1) using nanoparticle optics. Representative optical images (a-c) of single cells selected from ~60 cells in the full-frame images. The solutions containing the cells ($OD_{600\text{ nm}} = 0.1$), 1.3 pM Ag nanoparticles, and (a) 0, (b) 3.13 and (c) 31.3 $\mu\text{g/mL}$ AZT, were prepared in a vial and imaged in a fresh microchannel at 15 min interval for 2 h, respectively.

compare with the size index of individual Ag nanoparticles measured using transmission electron microscopy (TEM). The result shows that the color index of violet, blue, green, and red is correlated with the size index of 30 ± 10 , 50 ± 10 , 70 ± 10 ,

and 90 ± 10 nm, respectively. These nanoparticle probes offer an important possibility of direct measurement of the sized transformation of membrane pores in live cells with ms temporal resolution and nm size resolution using the optical microscopy equipped with a high-speed CCD camera. Images of the cells (nalB-1) incubated with Ag nanoparticles and AZT in a microchannel were directly recorded using dark-field optical microscopy and spectroscopy (Fig. 11B). The result demonstrates that more cells accumulated Ag nanoparticles in the cell membrane as AZT concentration increases, suggesting that the size and number of membrane pores increases as AZT concentration increases.

The result also demonstrates that more Ag nanoparticles are observed in the cells (WT) as AZT concentration increases (Fig. 12). The images clearly illustrate the morphology of the cells and indicate that the cellular membrane is intact in the absence of AZT (Fig. 12A) and becomes disrupted as AZT concentration increases to 3.13 (Fig. 12B) and 31.3 $\mu\text{g/mL}$ (Fig. 12C). In the absence of AZT, only a few of the Ag nanoparticles are accumulated in WT cells and the number of Ag nanoparticles in the cells remains almost unchanged with time (Fig. 13A:a). As AZT concentration increases to 3.13 and 31.3 $\mu\text{g/mL}$, the accumulation rate of intracellular Ag nanoparticles increases 2.8-fold and 6-fold, respectively (Fig. 13A:b; c). This result demonstrates that AZT induces real-time sized transformation of cell wall and membrane pores. In order to investigate the role of the MexAB-OprM efflux pump on controlling the function of AZT, two mutants of WT, nalB-1 (mutant with over-expression of MexAB-OprM) and ΔABM (MexAB-OprM deficient mutant), were used in the experiments. In the absence of AZT, as those observed in WT, only a few of the nanoparticles are accumulated in nalB-1 and ΔABM .

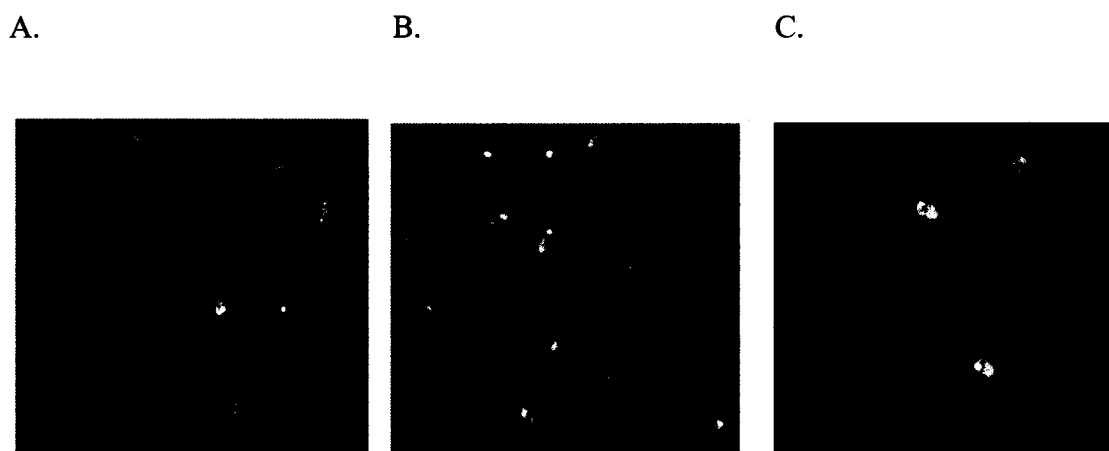


FIGURE 12. Monitoring membrane permeability of multiple cells (WT) simultaneously in real-time using nanoparticle optics. The full-frame optical images of the cells incubated with 1.3 pM Ag nanoparticles and AZT are directly recorded by the CCD camera (exposure time at 100 ms) and color digital camera through dark-field optical microscope. More nanoparticles are observed in the cells as AZT concentration increases. A, 0 µg/mL AZT. B, 3.1 µg/mL AZT. C, 31.3 µg/mL AZT.

The number of the nanoparticles remains almost unchanged over time (Fig. 13B-C:a). In the presence of 3.13 µg/mL AZT only a few of Ag nanoparticles are observed in nalB-1, unlike WT, and the number of Ag nanoparticles in nalB-1 remains unchanged over time (Fig. 13B:b). In contrast, the number of Ag nanoparticles accumulated in Δ ABM increases with time proportionally (Fig. 13C:b). Taken together, the result suggests that MexAB-OprM plays an important role in the accumulation of the nanoparticles in the cells. The least number of Ag nanoparticles is accumulated in nalB-1 (mutant with over-expression of MexAB-OprM) whereas the greatest number of Ag nanoparticles is observed in Δ ABM (MexAB-OprM deficient mutant). This suggests that MexAB-OprM appears to effectively extrude xenobiotics (nanoparticles) out of the cells at low AZT concentrations (0, 3.13 µg/mL) while the cellular membrane is still intact and membrane permeability is low. At the higher AZT concentration (31.3 µg/mL), the cellular wall is severely compromised and the

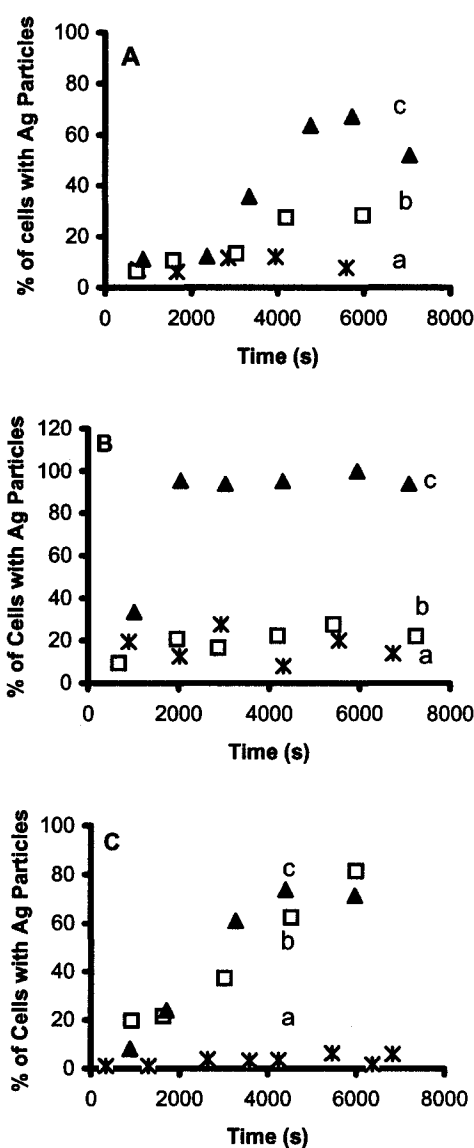


FIGURE 13. Direct observation of real-time size transformation of membrane permeability of the cells induced by AZT. Plots of percent of the cells with Ag nanoparticles versus time; ten images, similar to those in Fig. 8, from each solution, were acquired at 15 min interval with exposure time at 100 ms for each image. Approximately 300 cells in total were analyzed for each point. A, WT. B, nalB-1. C, ΔABM. a, (*) 0 μg/mL AZT. b, (□) 3.13 μg/mL AZT. c, (▲) 31.3 μg/mL AZT.

extrusion pump is unable to overcome the influx of xenobiotics (AZT and nanoparticles). Thus, the number of Ag nanoparticles in all strains *P. aeruginosa*

increases with time rapidly in presence of 31.3 $\mu\text{g/mL}$ AZT and is approximately 6-8 fold higher than in the absence of AZT.

DISCUSSION

Optical properties (colors) of Ag nanoparticles depend upon size and shape of the nanoparticles and the dielectric constant of the embedded medium of the nanoparticles. Therefore, the colors of nanoparticles are associated with sizes of nanoparticles when the shape of nanoparticle and embedded medium remain unchanged. The colors of Ag nanoparticles were correlated with their sizes as we reported previously (44, 47). This allowed us to use the color index of nanoparticles (violet, blue, green, and red) as the size index (30 ± 10 , 50 ± 10 , 70 ± 10 , and 90 ± 10 nm) for real-time measurement of size transformation of cell wall and membrane permeability at the nanometer scale using dark-field optical microscopy.

The quantum yield of Mie scattering of 20 nm Ag nanoparticles is about 10^7 times higher than that of a single fluorescent dye molecule. The scattering intensity of noble metal nanoparticles is proportional to the volume of nanoparticles. Thus, these nanoparticles are extremely bright and are able to be directly observed through dark-field microscope even with the naked eye. Unlike fluorescent dyes, these nanoparticles do not suffer photodecomposition and can be used as a probe to continuously monitor dynamic events in live cells for an unlimited time frame. The scattering intensity of the nanoparticles decreases about 10% as nanoparticles enter the cellular membrane because the cellular membrane and matrix absorb the light of the microscope illuminator and reduce its intensity. In addition, the quantum yield of Mie scattering of intracellular Ag nanoparticles is smaller than extracellular Ag nanoparticles because intracellular Ag nanoparticles are surrounded by biomolecules (e.g., proteins, lipid), which reduces the

reflection coefficient of Ag nanoparticles. Therefore, the nanoparticles outside the cellular membrane appear sharp and bright whereas the nanoparticles inside the cell membrane look blurry and dim. This feature allows us to determine whether the nanoparticles are inside or outside the cell membrane using the optical microscopy station. The locations of nanoparticles inside the cells have also been confirmed by TEM. The size of the nanoparticles (<100 nm) and the thickness of cell membrane (7 nm) are below the optical diffraction limit (~ 200 nm) of the microscope. The scattering intensity of nanoparticles is much higher than that of cellular membranes because of the higher intrinsic optical dielectric constant of Ag nanoparticles. It follows that the nanoparticles which appear to be accumulated on the membrane as those shown in Fig. 12C are blurry and dim and are therefore inside the cells.

Images of intact cells in Fig. 12 demonstrate that bulk cells are monitored simultaneously at single-cell resolution. A larger number of Ag nanoparticles are observed in the cells as the AZT concentration increases and the incubation time lengthens (Fig. 12-13). All cells studied are bacterial cells and currently there is no evidence available to support the process of endocytosis or pinocytosis in prokaryotes. This would suggest that AZT induces real-time size transformation of membrane pores and the accumulation of nanoparticles in the cells must be attributable to that increased membrane permeability.

Individual Ag nanoparticles are easily identified while the cellular membrane is still intact at low AZT concentrations ($0-3.13$ $\mu\text{g/mL}$) (Fig. 11B: a; b). Although optical images of nanoparticles always appear larger than actual size because of optical diffraction limit, the size of individual nanoparticles can be estimated using its optical color. At high AZT concentration (31.3 $\mu\text{g/mL}$), the cellular membrane is disintegrated,

leading to a rapid accumulation of nanoparticles in the cells. The accumulation of intracellular Ag nanoparticles exceeds the capacity of the cells and some of these nanoparticles begin to aggregate. Thus, it becomes difficult to distinguish individual nanoparticles (Fig. 11B: c). For antibiotics (e.g., chloramphenicol) that do not cause the complete disruption of the cell wall, individual nanoparticles in single cells can be well distinguished and monitored over time (44). Therefore, the observation of aggregating nanoparticles in live cells can be used to determine the complete disintegration of cell membrane and cell wall. This demonstrates another advantage of using nanoparticles as a probe to study modes of actions of antibiotics over fluorescent dyes, because fluorescent probes are unable to offer such information.

The two mutants of WT, *nalB-1* and Δ ABM, studied helped to demonstrate the role of MexAB-OprM in controlling the function of AZT. Although membrane permeability, as demonstrated by nanoparticle accumulation, of both mutants increased as AZT concentration increased and as incubation time increased, the rates of accumulation correlated with MexAB-OprM expression levels. The mutant with over-expression of MexAB-OprM (*nalB-1*) accumulated the least number of Ag nanoparticles in the presence of 3.13 μ g/mL AZT whereas the mutant with the deficient MexAB-OprM (Δ ABM) accumulated the most Ag nanoparticles. The result suggests that MexAB-OprM played an important role in the accumulation of Ag nanoparticles inside cells. *P. aeruginosa* is able to selectively extrude an array of substrates, including antibiotics, dyes, detergents, and chemo-toxic materials, out of the cells using efflux pumps with the proton motive force as the energy source (1-2, 27, 67-68). Thus, one plausible explanation for the role of MexAB-OprM in the observed accumulation of nanoparticles in the cells is the extrusion of nanoparticles out of cells. The mechanism

of nanoparticle extrusion could be similar to that of other substrates. The mechanism of how substrates uptake and efflux by *P. aeruginosa* still remains unclear despite the extensive study over decades (1-2, 27, 67-68). The nalB-1, mutant with over-expression of MexAB-OprM, appeared to extrude nanoparticles out of cells more effectively than Δ ABM (mutant with deficient of MexAB-OprM). Consequently, nalB-1 accumulated fewer nanoparticles than Δ ABM. In the presence of 31.3 μ g/mL AZT, a significant number of Ag nanoparticles accumulated in both mutants, indicating the complete disruption of membrane. This result demonstrates that MexAB-OprM efflux pump plays an important role in the equilibration of the size transformation of membrane permeability only while the membrane is still intact (i.e. in low concentrations of AZT (0, 3.13 μ g/mL). This study confirmed that the function of AZT is indeed the destruction of cell membrane (Fig. 11-12) and legitimized the real-time nanoparticle optical assay.

CHLORAMPHENICOL EXPERIMENTS

Cell Culture and Preparation

Three strains of *P. aeruginosa*, WT (PAO4290), a wild-type expression level of MexAB-OprM), nalB-1 (TNP030#1), a MexAB-OprM over-expression mutant, and Δ ABM (TNP076), a MexAB-OprM deficient mutant, were used. Cells were pre-cultured in L-broth medium containing 1% tryptone, 0.5% yeast extract, and 0.5% NaCl at pH 7.2 in a shaker (Lab-line Orbit Envivon-Shaker, 150 rpm and 37 °C) overnight to ensure the full growth of the cells. Cells were then cultured for an additional 8 hours. Cells were harvested by centrifugation at 7500 rpm (Beckman Model J2-21 Centrifuge, JA-14 rotor) and 23 °C for 10 minutes, washed three times with 50 mM PBS (pH = 7.0)

and then suspended again in the same buffer with a final adjusted cell concentration of $OD_{600nm} = 0.1$. These cell suspensions are employed for the study of membrane transport using single nanoparticle optics, single living cell imaging, and the preparation of samples for TEM imaging.

Single Living Cell and Single Nanoparticles Imaging System

The dark-field optical microscope is equipped with an oil dark-field condenser (Oil 1.43-1.20, Nikon), a 100x objective (Nikon Plan fluor 100x oil, iris, SL. N.A. 0.5-1.3, W.D. 0.20 mm), the microscope illuminator (100 W halogen), a CCD camera (Micromax, 5 MHz Interline, PID 1030 x 1300, Roper Scientific) for high-speed and high-resolution cell imaging, and a color digital camera (Coolpix 990, Nikon) for real-color imaging. Both cameras are added to the microscope through a quad-adaptor (Nikon) for real-time imaging. A LN back-illuminated CCD camera (Roper Scientific) coupled with a SpectraPro-150 (Roper Scientific) is added to the microscope using another quad-adaptor (Nikon) for simultaneous spectroscopic measurement (44, 46-48). This microscopy and spectroscopy system is capable of real-time imaging of single living cells, imaging and spectroscopic characterization of single nanoparticles, and single molecule detection (77 - 78).

Preparation and Imaging of Cell Suspensions

Three milliliters (3 mL) cell suspensions containing 1.3 pM Ag nanoparticles and chloramphenicol (0, 25 and 250 $\mu\text{g/mL}$) were prepared by mixing 2703 μL of the cell solution ($OD_{600\text{ nm}} = 0.1$) and 9.8 μL of 0.4 nM Ag nanoparticles, with ultrapure water, 30 μL of 2.5 mg/mL chloramphenicol, 30 μL of 25 mg/mL chloramphenicol, respectively. Each suspension was incubated in a vial at 37°C for 2 h. A 20 μL aliquot of the mixed suspension was sampled at 15-min intervals and directly imaged (100 ms

exposure time) in a freshly prepared micro-channel using the dark-field microscopy and spectroscopy imaging system equipped with CCD camera. The sealed micro-channel was constructed by sandwiching the solution between a microscope slide and a cover slip with a 6 μ m thick membrane as a spacer.

Data Analysis and Statistics of Single Living Cell Imaging

Each full-frame CCD image was able to simultaneously monitor ~60 cells from a cell suspension with $OD_{600\text{ nm}} = 0.1$. Ten representative images of each suspension at 15 min intervals were recorded over 2 h. Thus, 70 images (~4200 cells) were acquired in total for each solution over the course of 2 h. Each experiment was repeated at least three times; thus, ~12,600 cells of each strain of *P. aeruginosa* were studied and analyzed at single-cell resolution. Images of five representative cells from each suspension were selected to show the intracellular nanoparticles in detail (Fig. 16 A). Cumulative histograms of the distribution of number of nanoparticles in the cells versus the nanoparticle sizes are shown in Fig. 17. At every 15 min, ten images (~600 cells) of each suspension were recorded for each data point in Fig. 20. Each experiment was repeated at least three times. Thus, in total ~18,000 cells of each strain of *P. aeruginosa* at each 15 min were studied and analyzed at the single-cell resolution.

Ultra-Thin Sectioning of Cells for Transmission Electron Microscopy Imaging

A 120 mL aliquot of cell suspension ($OD_{600\text{ nm}} = 0.1$) containing 1.3 pM Ag nanoparticles and chloramphenicol (0, 25, 250 μ g/mL) was prepared as described above and incubated in the shaker (150 rpm and 37 °C) for 2 hours. Cells were then harvested using centrifugation at 25,000 rpm (a Beckman ultra-centrifuge, Ti-50 rotor, at 23 °C) for 30 min. Each pellet was suspended in 1 mL of PBS buffer (pH = 7.0). Each solution was transferred to a sterile micro-centrifuge tube. The cells were collected using

centrifugation at 2000 rpm for 5 min, and the cell pellets were fixed using 2% glutaraldehyde in PBS and incubating at 4°C overnight. The primary fixative was removed and the pellets were rinsed with PBS buffer in triplicate; each wash cycle lasted 10 min. The cell pellets were then removed from the micro-centrifuge tube and deposited onto a clean microscope slide. A 30 μ L aliquot of agar was mixed with each pellet and allowed to solidify. Excess agar was trimmed away from the pellets using a razor blade. Each pellet was then divided into duplicate samples. The solidified pellets were transferred to sterile tubes. A 5 mL aliquot of 2% OsO₄ in distilled water was added into each tube as a secondary fixative; fixation was carried out at 4°C for 2 h. The pellets were rinsed using distilled water (x 3); each washing cycle lasted 10 min. Pellets were then dehydrated using 25%, 50%, 75%, and 100% ethanol in distilled water (5 mL) for 15 min each. The pellets were infiltrated using a mixture of resin and acetone (50/50) (EM Bed 812, Ted Pella) at room temperature overnight (79). The pellets were then infiltrated using 100% resin for 1 h. The pellets were then transferred to embedding molds and embedded in 100% resin. The molds were placed in an oven to cure at 65°C for 48 h. Sections with 0.5 μ m thicknesses were prepared using an ultramicrotome (RMC MT2C) and examined using an optical microscope to ensure the sample was well prepared. The micro-sections were then sliced using a diamond knife to prepare 70-80 nm ultra-thin layer cross-sections. The nanometer ultra-thin sections were mounted on 100 mesh Formvar-coated copper grids, slightly stained with a uranyl acetate/lead citrate mixture, and imaged using the TEM (100CXII, Jeol); operating voltage was 60 kV.

RESULTS

Real-Time Sizing Membrane Permeability Using Single Nanoparticle Optics

Silver nanoparticles with diameters 20-100 nm were synthesized as described above. These Ag nanoparticles were characterized using dark-field optical microscopy, spectroscopy and TEM (Fig. 14). The full-frame optical image (Fig. 14A) shows that the solution contained multiple colors of single nanoparticles. The TEM image in Fig. 14B indicates that Ag nanoparticles with a variety of sizes were present in the solution. Fig. 14B also shows that the majority of nanoparticles are spherical while a very few nanoparticles are triangular and hexagonal. The color distribution of single nanoparticles in 0.4 nM solution measured using dark-field microscopy and spectroscopy was used to compare with the size distribution of single nanoparticles from the same solution determined by TEM. The results indicated that the color index of violet, blue, green, and red correlated with the size index of 30 ± 10 , 50 ± 10 , 70 ± 10 , and 90 ± 10 nm, respectively, as we reported previously. The solution contained approximately 23% of violet (30 ± 10 nm), 53% of blue (50 ± 10 nm), 16% of green (70 ± 10 nm), and 8% of red (90 ± 10 nm) nanoparticles. These multicolored nanoparticles were then used as nanometer-sized probes to directly measure the sizes of substrates that could transport through living microbial membrane. The aim was to determine the change in membrane permeability and pore sizes in real time.

To minimize the possible effect of competitive transport between nanoparticles and the substrate of interest (i.e. chloramphenicol) and to prevent the possible aggregation of nanoparticles, a very low concentration of nanoparticles (1.3 pM) was used with the living cells ($OD_{600\text{ nm}} = 0.1$) for real-time monitoring of membrane

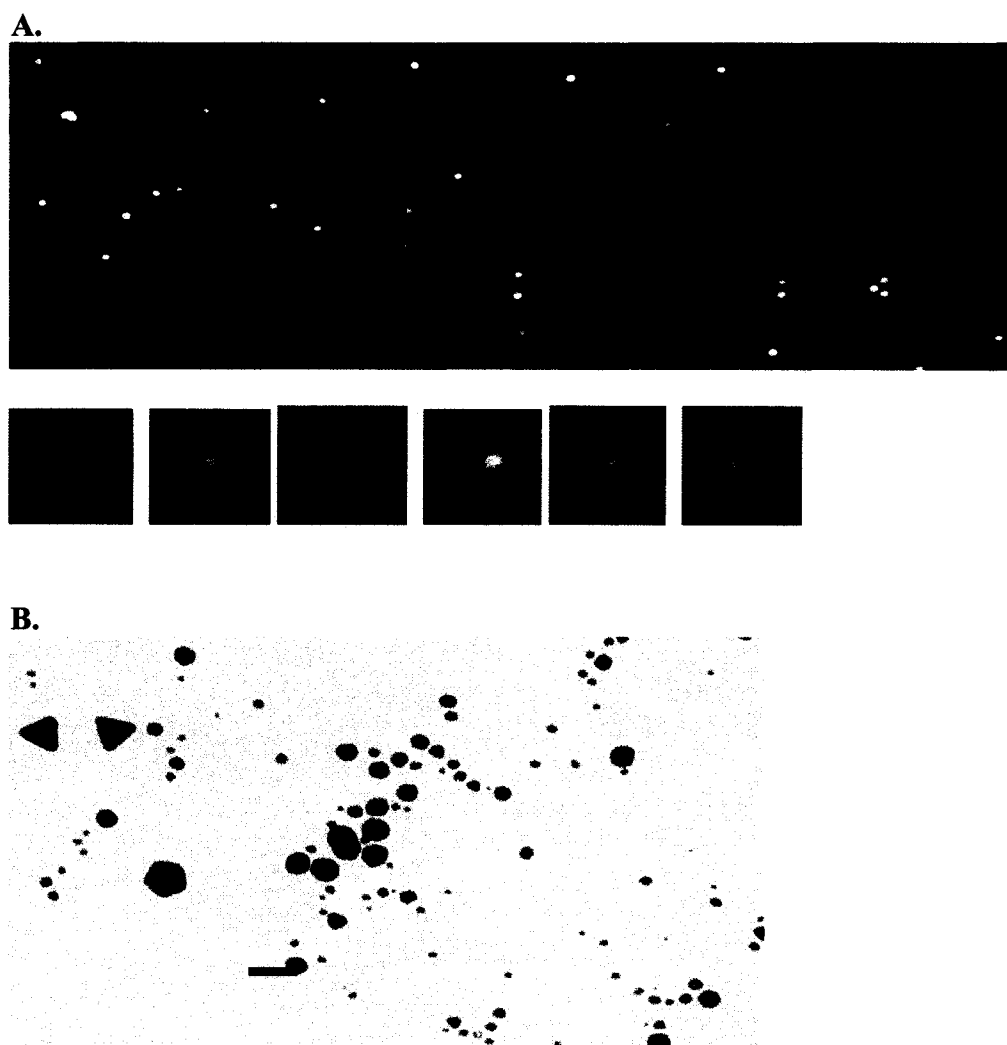


FIGURE 14. Characterization of Ag nanoparticles, color and size indices. A, The representative full frame optical image of individual Ag nanoparticles taken from a 0.4 nM Ag nanoparticle solution in a microchannel by a digital color camera through the dark-field optical microscope. Optical images of single Ag nanoparticles selected from the full frame image show the color index of Ag nanoparticles. The optical images of nanoparticles look larger than their actual sizes because of the optical diffraction limit (~ 200 nm). B, Representative TEM images of Ag nanoparticles from the solutions in (A) show the sizes and shapes of nanoparticles. The scale bar represents 40 nm.

transport at the nanometer scale. Many living individual cells and single nanoparticles in the microchannel were monitored simultaneously using a CCD camera through a dark-field microscope. More nanoparticles were observed in the cells as chloramphenicol concentration increased (Fig. 15). Representative images of single

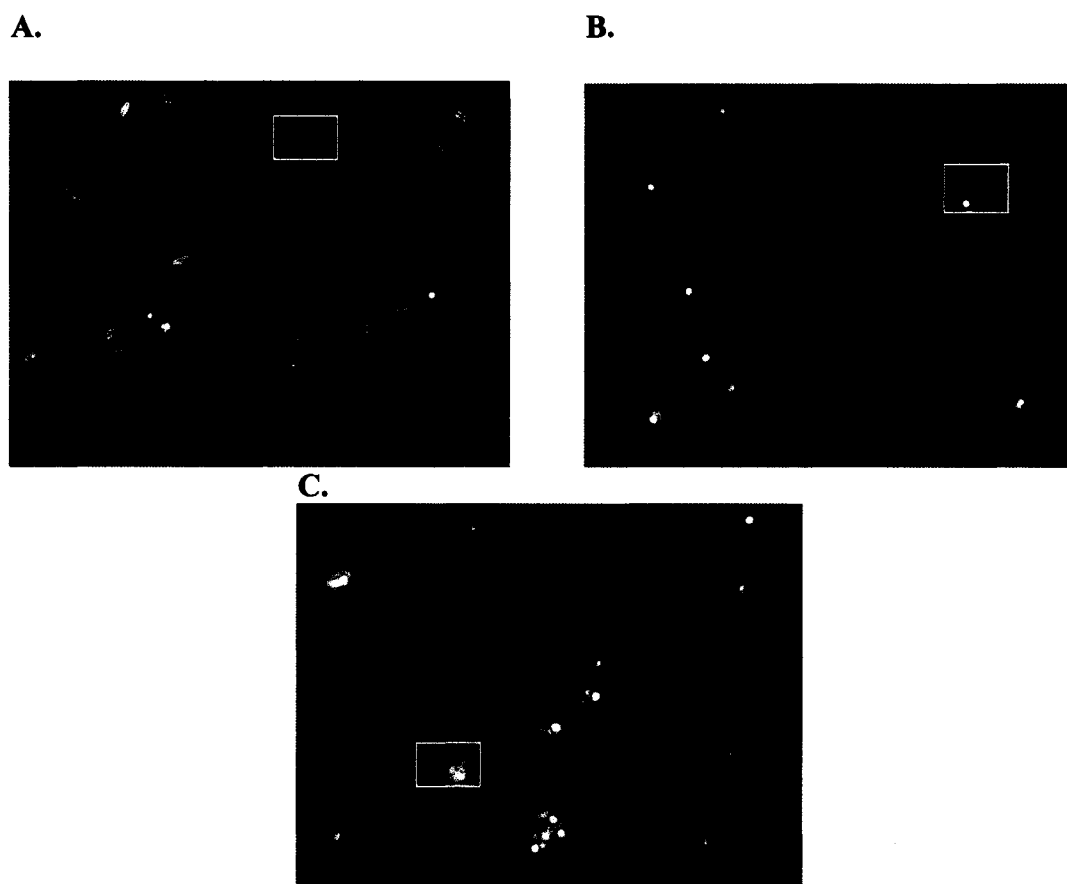


FIGURE 15. Simultaneous real-time monitoring of membrane transport in multiple living cells (WT) with and without chloramphenicol. The representative optical images of the cells ($OD_{600\text{ nm}} = 0.1$) incubated with 1.3 pM Ag nanoparticles. A, $0\text{ }\mu\text{g/mL}$ chloramphenicol and no nanoparticles in highlighted cell. B, $25\text{ }\mu\text{g/mL}$ chloramphenicol and single nanoparticle in highlighted cell. C, $250\text{ }\mu\text{g/mL}$ chloramphenicol and multiple nanoparticles in highlighted cell. The scale bar represents $4\text{ }\mu\text{m}$.

cells selected from the full images shown in Fig. 16 illustrate the cells containing nanoparticles in detail and highlight that more nanoparticles are present in the cells as chloramphenicol concentration increases. Normalized histograms of the number of nanoparticles with the cells versus sizes of the nanoparticles (Fig. 17) indicated that a greater number of larger Ag nanoparticles are with the cells as chloramphenicol concentration increases, suggesting that the permeability and porosity of the cellular membrane increased as chloramphenicol concentration increased. Note that a higher

percentage of 50 ± 10 nm nanoparticles (53% of total nanoparticles) are present in the solution. Therefore, more 50 ± 10 nm nanoparticles are observed in the cells. The relative numbers of specific sizes of intracellular nanoparticles in the presence of 0, 25 and 250 $\mu\text{g/mL}$ chloramphenicol are compared to determine the change of membrane permeability and porosity as chloramphenicol concentration increased.

The integrated scattering intensity of selected individual nanoparticles in and out of cells were measured and subtracted from the background of the same image. Results indicated that the intensity of intracellular nanoparticles was about 10% less than extracellular nanoparticles in the solution and about 20% less than those extracellular nanoparticles on the membrane. The scattering intensity of nanoparticles decreased slightly ($\sim 10\%$) as nanoparticles entered the cellular membrane because the cellular membrane and matrix absorb the microscope illuminator light and reduced its intensity. The decreased intensity of intracellular nanoparticles appears to depend upon the location of nanoparticles inside the cells (e.g. depth below the cellular membrane). We attempted to quantitatively correlate the scattering intensity of intracellular nanoparticles with their depth below the cellular membrane. Unfortunately, the task was impossible because the optical diffraction limit defined the spatial resolution (~ 200 nm) and made the nanoparticles appear larger than their actual sizes. Nevertheless, we were able to qualitatively determine whether the nanoparticles were in or out of the cells based upon their intensity changes as these nanoparticles entered the cells and their transport processes were recorded in real time (44). In addition, the quantum yield of Rayleigh/Mie scattering of intracellular Ag nanoparticles is smaller than extracellular Ag nanoparticles because intracellular Ag nanoparticles are surrounded by biomolecules (e.g., proteins, lipid) that reduce the reflection coefficient of Ag nanoparticles.

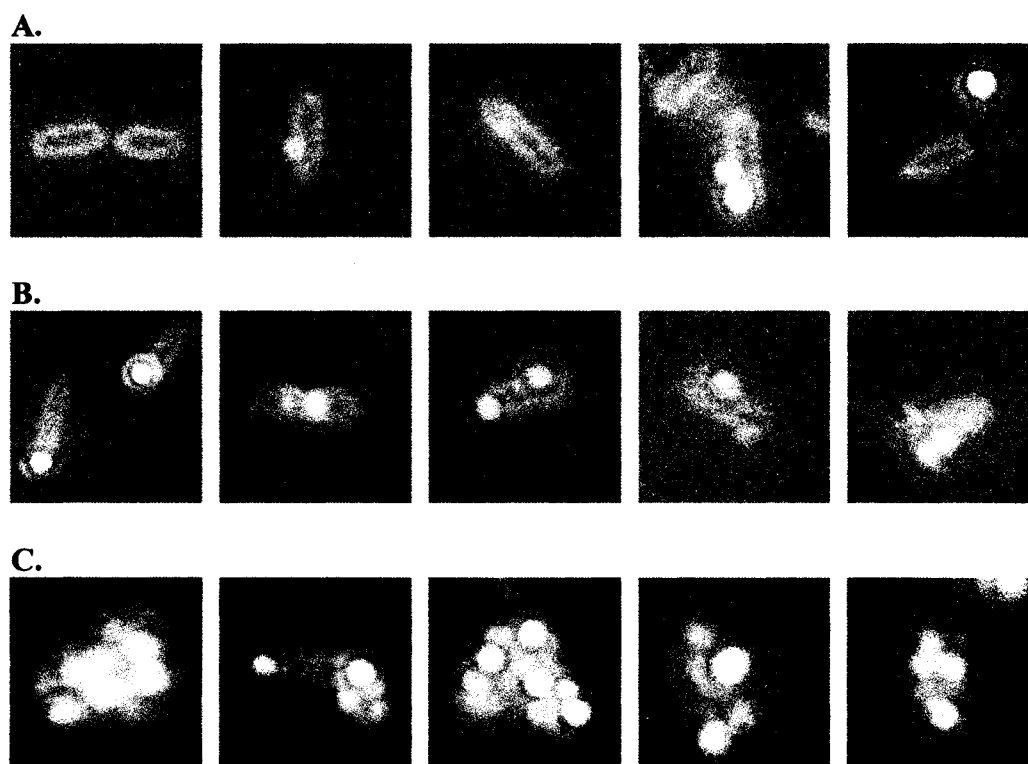


FIGURE 16. Direct real-time observations of dose-dependent changes in membrane permeability and pore sizes in *P. aeruginosa* (WT), induced by chloramphenicol. Representative optical images (A-C) of single cells selected from ~60 cells in the full-frame images similar to Fig. 15. Each solution is prepared in a vial and imaged in the microchannel at 15 min intervals for 2 h. The solutions contain the same concentration of cells ($OD_{600\text{ nm}} = 0.1$) and Ag nanoparticles (1.3 pM), but different concentration of chloramphenicol. A, 0 $\mu\text{g/mL}$ chloramphenicol. B, 25 $\mu\text{g/mL}$ chloramphenicol. C, 250 $\mu\text{g/mL}$ chloramphenicol.

Therefore, the nanoparticles outside the cellular membrane appear to radiate more sharply and brightly, whereas nanoparticles inside the cells look blurry and dim (Fig. 18). This feature allowed us to determine whether the nanoparticles were inside or outside the cells using optical microscopy. The size of the nanoparticles (<100 nm) and the thickness of cell membrane (36 nm including 8 nm inner or outer membrane and ~20 nm between inner and outer membrane of gram-negative bacteria) were all below the optical diffraction limit (~200 nm). The scattering intensity of nanoparticles is much

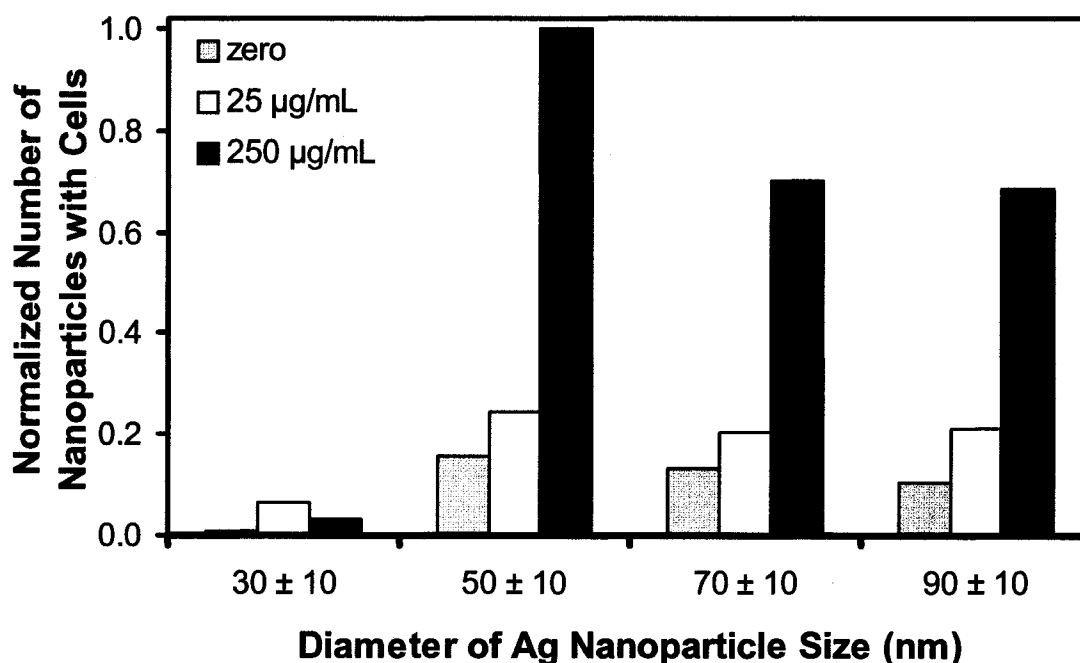


FIGURE 17. Representative normalized histograms of the number of Ag nanoparticles with the cells versus sizes of nanoparticles from the solutions in Fig. 16. Each solution contains the same concentration of cells ($OD_{600\text{ nm}} = 0.1$) and Ag nanoparticles (1.3 pM), but different concentration of chloramphenicol.

higher than that of the cellular membrane because of the higher intrinsic optical dielectric constant of Ag nanoparticles. Therefore, the nanoparticles are much brighter than the membrane, appearing to be accumulated on the membrane (Fig. 18B). However, these nanoparticles are blurry, and dimmer than the extracellular nanoparticles, which indicated that these blurry nanoparticles are inside the cells. Taken together, the results indicate that, in the absence of chloramphenicol, the majority of red nanoparticles (>80 nm) appear to stay outside the cells, whereas violet, blue and green nanoparticles (< 80 nm) may enter the cells.

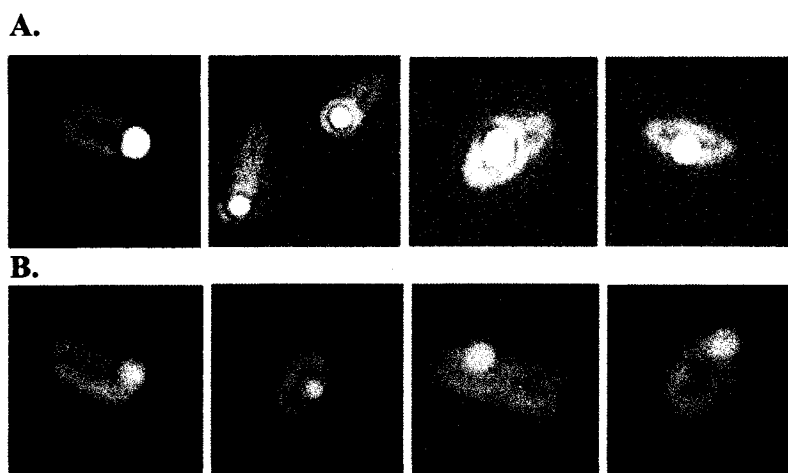


FIGURE 18. Determination of extracellular and intracellular Ag nanoparticles using the scattering intensity of nanoparticles. Optical images of Ag nanoparticles accumulated (A) on membrane (outside the cell) and (B) inside single living cells (*P. aeruginosa*) recorded by digital color camera and CCD camera (exposure time = 100 ms) through the dark-field optical microscope. Extracellular nanoparticles in (A) appear to radiate more sharply and brightly, whereas intracellular nanoparticles in (B) look blurry and dim, indicating that the scattering intensity of nanoparticles decreases as nanoparticles enter the cells, owing to light absorption of cellular membrane and decreased reflection coefficient of intracellular Ag nanoparticles. The scale bars represent 2 μm . The solutions are prepared as described in Fig. 12.

To determine the sizes and locations of intracellular nanoparticles at the sub-nanometer (\AA) level, ultrathin sections (70-80 nm) of the fixed cells that had been incubated with 1.3 pM nanoparticles and chloramphenicol (0, 25 and 250 $\mu\text{g/mL}$) for 2 hours, were prepared and imaged using TEM as described above. TEM images in Fig. 19A unambiguously demonstrate that Ag nanoparticles with a variety of sizes (20-80 nm in diameter) are inside the cells in the absence of chloramphenicol. The majority of the nanoparticles were located in the cytoplasmic space of the cells, whereas a few nanoparticles were just underneath the cellular membrane. The cells with embedded triangular nanoparticles (Fig. 19A) were selected for easy identification of Ag nanoparticles (Fig. 10B). Since the cells were aligned randomly in the embedded resin

pellets and were sliced in a random fashion, the shapes of cells are different as shown in Fig. 19. The representative cell shapes (e.g., slicing through the vertical or horizontal center of the cells or off the centers of the cells) are selected and shown in Fig. 19 to illustrate the positions of the intracellular nanoparticles. Taken together, the TEM images showed that nanoparticles with sizes ranging up to 80 nm were embedded inside the cells in the absence of chloramphenicol, which agreed well with those measured using single nanoparticle optics. This suggests that, even in the absence of chloramphenicol, nanoparticles up to 80 nm can transport through the outer and inner cell membrane of *P.aeruginosa*. This size is about 50 times larger than conventional antibiotics. As chloramphenicol concentration increased from 0 to 25 and 250 $\mu\text{g/mL}$, larger Ag nanoparticles are observed inside the cells. This result suggests that by inhibiting protein synthesis, chloramphenicol increased the membrane permeability and sizes of membrane pores.

To investigate the role of the efflux pump proteins (MexAB-OprM) in controlling the accumulation of intracellular nanoparticles and function of chloramphenicol, we studied the membrane permeability of two mutants, nalB-1 (the mutant with the overexpression level of MexAB-OprM) and ΔABM (the mutant devoid of MexAB-OprM). Plots of the normalized percent of intracellular Ag nanoparticles versus time for WT, nalB-1 and ΔABM in 0, 25 and 250 $\mu\text{g/mL}$ chloramphenicol, are shown in Fig. 20A (a, b, c), 20B (a, b, c) and 20C (a, b, c), respectively. Each data point represents 600 cells in ten full-frame images, which were acquired in real time as the cells were accumulating intracellular Ag nanoparticles. The nanoparticles transporting in and out of the cells were recorded in real time, resulting in the fluctuation of data points in

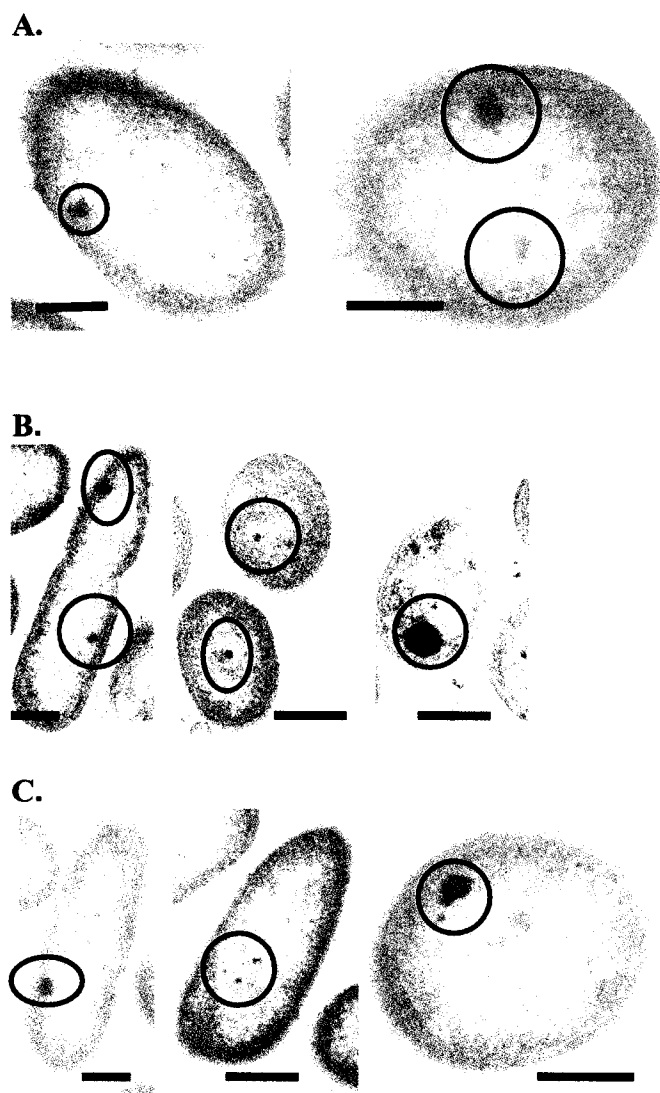


FIGURE 19. Transmission electron micrographs showing sizes and locations of Ag nanoparticles inside Wild Type (WT) cells. Ultra-thin cross-sections (70-80 nm) of fixed WT cells were sectioned using a diamond knife. The cells ($OD_{600\text{ nm}} = 0.1$) have been incubated with 1.3 pM Ag nanoparticles. The scale bars represent 220 nm and the circles are used to highlight the nanoparticles. A, 0 $\mu\text{g/mL}$ chloramphenicol. B, 25 $\mu\text{g/mL}$ chloramphenicol. C, 250 $\mu\text{g/mL}$ chloramphenicol. All cells were incubated for 2 h before fixation, as described in the text.

Fig. 20. The number of intracellular Ag nanoparticles in nalB-1 (MexAB-OprM overexpression mutant) appeared to fluctuate greatly (Fig. 20B). This observation may be attributable to a higher efflux rate of nanoparticles by nalB-1 and suggests that

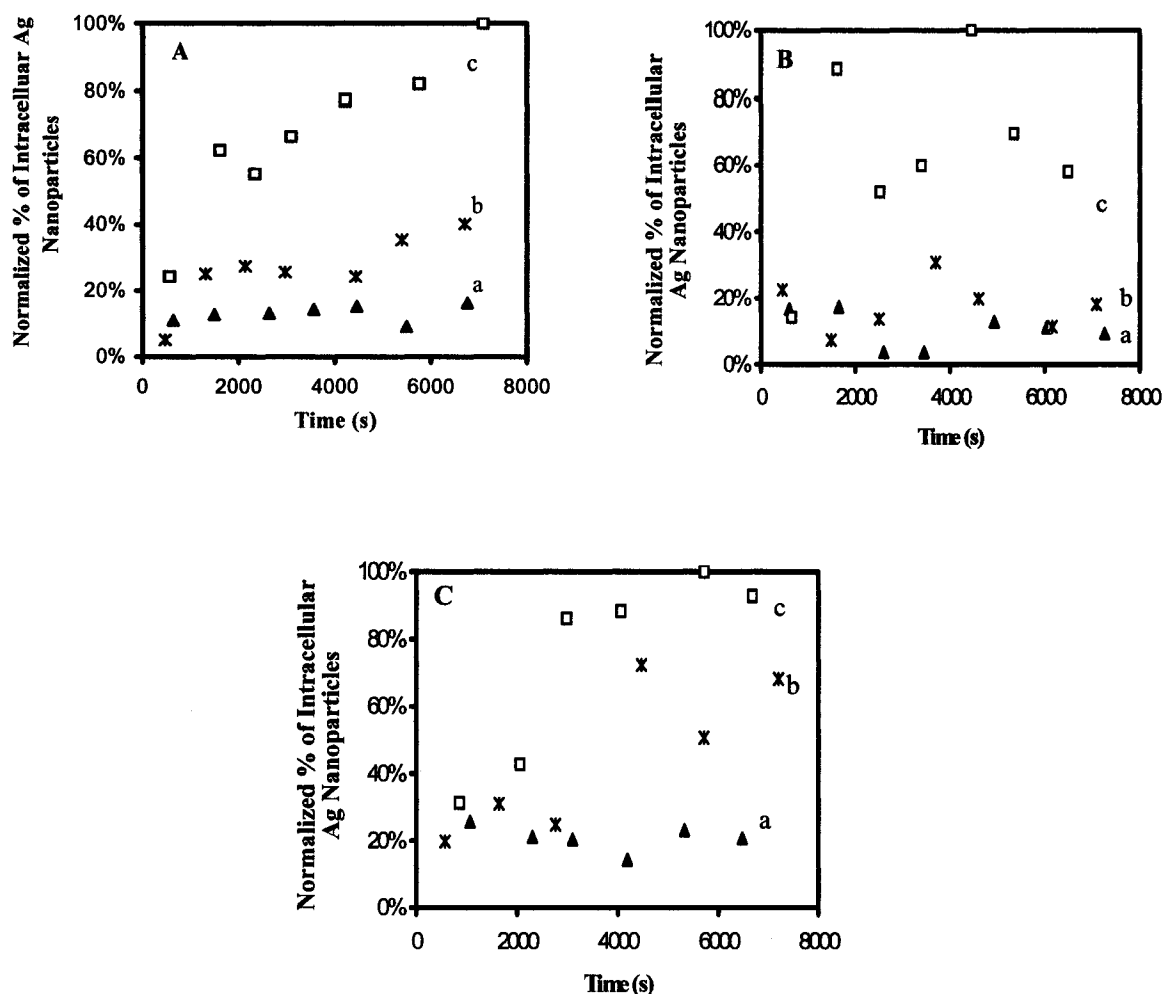


FIGURE 20. Real-time measurements of accumulation kinetics of single Ag nanoparticles in living cells. Membrane permeability and porosity increases as chloramphenicol concentration increases. Plots are of normalized the number of intracellular Ag nanoparticles versus time. A, WT: \blacktriangle 0 $\mu\text{g/mL}$ chloramphenicol, $*$ 25 $\mu\text{g/mL}$ chloramphenicol, \square 250 $\mu\text{g/mL}$ chloramphenicol. B, nalB-1: \blacktriangle 0 $\mu\text{g/mL}$ chloramphenicol, $*$ 25 $\mu\text{g/mL}$ chloramphenicol, \square 250 $\mu\text{g/mL}$ chloramphenicol. C, ΔABM : \blacktriangle 0 $\mu\text{g/mL}$ chloramphenicol, $*$ 25 $\mu\text{g/mL}$ chloramphenicol, \square 250 $\mu\text{g/mL}$ chloramphenicol. Ten full-frame images of each solution are acquired at 15 min intervals and each image is recorded with 100 ms exposure time. Each data point represents 600 cells.

nanoparticles were indeed moving in and out of living cells in real time. Note that these cells were incubated in PBS at room temperature and the cell growth rate in such an

environment is negligible. Thus, the cell concentration remained unchanged over the 2-hour incubation.

In order to understand the effect of chloramphenicol upon membrane porosity and transport, the accumulation kinetics of single Ag nanoparticles of WT, nalB-1 and Δ ABM in the absence and presence of chloramphenicol (0, 25 and 250 $\mu\text{g/mL}$) were measured and compared. In the absence of chloramphenicol (Fig. 20: a), a very small number of intracellular Ag nanoparticles were observed in WT (Fig. 20A: a) and Δ ABM (Fig. 20C: a), whereas few of intracellular Ag nanoparticles were found in nalB-1 (Fig. 20B: a). The number of intracellular Ag nanoparticles in all three strains remained relatively constant. As the chloramphenicol concentration increased to 25 $\mu\text{g/mL}$ (Fig. 20: b), the number of intracellular Ag nanoparticles in WT (Fig. 20A: b) and Δ ABM (Fig. 20C: b) increased with time at a rate of 4×10^{-5} and $8 \times 10^{-5} \text{ s}^{-1}$ respectively which are about ten-fold higher than in the absence of chloramphenicol. In contrast, the number of intracellular Ag nanoparticles in nalB-1 (Fig. 20B: b) remained almost unchanged over time as observed in the absence of chloramphenicol (Fig. 20B: a). As chloramphenicol concentration increased to 250 $\mu\text{g/mL}$ (Fig. 20: c), the number of intracellular Ag nanoparticles in WT (Fig. 20A: c) and Δ ABM (Fig. 20C: c) increased with time at a rate of 1×10^{-4} and $2 \times 10^{-4} \text{ s}^{-1}$, which were about 2.5-fold higher than in 25 $\mu\text{g/mL}$ chloramphenicol, respectively. Unlike those observed in 0-25 $\mu\text{g/mL}$ chloramphenicol, the intracellular Ag nanoparticles in nalB-1 (Fig. 20B: c) increased with time at the rate of $5 \times 10^{-5} \text{ s}^{-1}$, that is about 2-fold and 4-fold lower than in WT and Δ ABM, respectively.

Taken together, the results show that the number of Ag nanoparticles accumulated in all three strains increased as chloramphenicol concentration increased

and as incubation time increased, suggesting that chloramphenicol increases membrane porosity and permeability (Fig. 20). In addition, the results indicated that accumulation kinetics of intracellular nanoparticles is associated with the expression levels of MexAB-OprM. The mutant with overexpression level of MexAB-OprM (nalB-1) accumulated the least number of intracellular Ag nanoparticle, whereas the mutant devoid of MexAB-OprM (Δ ABM) accumulated the greatest number of Ag nanoparticles, suggesting that MexAB-OprM plays a critical role in controlling of accumulation of intracellular Ag nanoparticles.

DISCUSSION

Optical properties (e.g. color) of Ag nanoparticles depend on size and shape of nanoparticles and the dielectric constant of the embedded medium (80). Unlike the bulk plasmon, the surface plasmon of nanoparticles can be directly excited by propagating electromagnetic waves, leading to the selective absorption and scattering of light. When the shape of the nanoparticles and their embedded medium remain unchanged, the colors of Ag nanoparticles are dependant upon the sizes of the nanoparticles (Fig. 14A). Such unique size dependent optical properties allow us to use the color index of nanoparticles (violet, blue, green, red) as a nanometer size index probes (30 ± 10 , 50 ± 10 , 70 ± 10 , 90 ± 10 nm) for real-time monitoring of living cellular membrane permeability and porosity at the nanometer scale.

Individual Ag nanoparticles are extremely bright under dark-field optical microscope and can be directly imaged by a digital or CCD camera through the dark-field microscope. Unlike fluorescence dyes, these nanoparticles do not suffer photodecomposition and can be used as a probe to continuously monitor dynamics and kinetics of membrane transport in living cells for an extended time (hours). In addition,

these nanoparticles can be used as nanometer probes to determine the sizes of substrates that are transporting in and out of the living cellular membrane at the nanometer scale in real time.

The scattering intensity of the nanoparticles decreases as nanoparticles enter the cell membrane and move into the cytoplasmic space for two main reasons. Light from the microscope illuminator is absorbed by the cellular membrane and is less intense when it reaches an intracellular nanoparticle. Secondly, the cellular matrix (e.g. proteins, lipids) lowers the reflection coefficient of intracellular nanoparticles when compared to extracellular Ag nanoparticles. With an imaging system that is sufficiently sensitive to detect single fluorescence dye molecules, intracellular and extracellular single Ag nanoparticles with diameters at 20-100 nm are easily observed and distinguished (Fig. 17 and 18A). Since the size of nanoparticles and thickness of cellular membrane are under the optical diffraction limit (~ 200 nm), the intracellular nanoparticles appear accumulated on the membrane (Fig. 18B). However, these nanoparticles appeared blurry and dimmer than the extracellular nanoparticles, indicating that the blurry nanoparticles were inside the cells.

TEM was used to confirm the intracellular nanoparticles inside the cells at sub-nanometer (\AA) resolution. The TEM images of ultrathin cross-section of cells with nanoparticles in Fig. 19 unambiguously illustrate that the nanoparticles with the sizes up to 80 nm in diameter were observed inside the cells in the absence of chloramphenicol. The majority of nanoparticles (20-80 nm) were in the cytoplasmic space of the cells, whereas some of nanoparticles were right underneath the cellular membrane. This finding suggests that the outer and inner membranes of *P. aeruginosa* are permeable to

substrates with sizes up to 80 nanometers, which are 50 times larger than conventional antibiotics and detergents.

Bulk cells are monitored simultaneously at the single-cell resolution using single living cell imaging (Fig. 16). Accumulation kinetics of nanoparticles in living cells were measured in real time using single nanoparticle optics. Even though these nanoparticles look larger than their actual sizes due to the optical diffraction limit of the microscope, the sizes of nanoparticles were determined using their colors. As chloramphenicol concentration increased from 0 to 25 and 250 $\mu\text{g/mL}$, more nanoparticles were observed in the cells, suggesting that the membrane permeability and porosity increased. As more nanoparticles accumulated in the cells, it became more difficult to distinguish individual nanoparticles. Nevertheless, the sizes of individual intracellular nanoparticles were still able to be distinguished using their colors even in the presence of 250 $\mu\text{g/mL}$ chloramphenicol. This suggests that chloramphenicol increased membrane permeability, but did not completely disintegrate the cell walls. Such observations were distinguished from our previous study of the function of AZT (β -lactam antibiotic) in which AZT completely interrupted the cell walls and individual intracellular Ag nanoparticles were aggregated and hard to distinguish in the presence of 31.3 $\mu\text{g/mL}$ AZT.

Chloramphenicol is neither a β -lactam nor aminoglycoside antibiotic. Its primary target is ribosomal peptidyl transferase, where it acts competitively to inhibit normal substrate binding and protein synthesis. This study suggests that chloramphenicol also lead to increased membrane permeability. These new insights further demonstrate the unique advantages of using single nanoparticles as probes for the study of function of antibiotics and membrane transport. A plausible explanation for

such a mode of action of chloramphenicol is that the drug inhibits protein synthesis, leading to disintegration of the membrane and increased membrane permeability.

The accumulation rate of intracellular nanoparticles showed genetic dependence (Fig. 20); a mutant devoid of MexAB-OprM (Δ ABM) accumulated the nanoparticles most rapidly, whereas MexAB-OprM overexpression mutant (nalB-1) accumulated the nanoparticles most slowly. This result suggests that the xenobiotic pump mechanism comprised of MexAB-OprM played an important role in controlling the accumulation of nanoparticles in the cells; nanoparticles are much larger substrates than conventional drugs (e.g., antibiotics, dyes).

It was surprising that the nanoparticles (up to 80 nm) were observed to permeate the cellular membrane in the absence of chloramphenicol. These are bacterial cells and currently there is no evidence available to support the process of endocytosis, pinocytosis or exocytosis in prokaryotes (*P. aeruginosa*). However, it is well known that MexAB-OprM can extrude a wide spectrum of substrates, such as antibiotics, dyes, detergents, and chemotoxic materials, out of the cells using the proton motive force as the energy source. Therefore, one plausible suggestion for the transport mechanism of nanoparticles through the living cellular membrane is that nanoparticles enter the cells through passive diffusion, and are most likely extruded out of the cells by the extrusion mechanism of bacteria. Even though the sizes of Ag nanoparticles seem 50 times larger than the pore sizes of membrane pumps (MexAB-OprM), it is possible that the substrates (nanoparticles) can induce the assembly of the pumps in real time and define the pore sizes of the pumps. Currently, the crystal structure of the membrane pump is unavailable and the extrusion mechanism of the pump still remains essentially unknown.

On the other hand, it is also possible that Ag nanoparticles may enter the cells and are extruded out of the cells using unidentified pathways.

Unlike fluorescence probes, Ag nanoparticles can offer real-time size information of the substrates that transport through living cell membranes at the nanometer scale. Because the color index of nanoparticles can be used as the nanometer size index, the accumulation kinetics can be measured at the millisecond temporal resolution using dark-field optical microscopy and spectroscopy. In addition, the scattering intensity of Ag nanoparticles decreases slightly (~10%) as nanoparticles pass through the membrane and enter the cells, offering the opportunity to trace the transport of nanoparticles in and out of the membrane. Furthermore, the scattering intensity of Ag nanoparticles does not decay over time, owing to their resistance to photodecomposition. Taken together, these unique characteristics of Ag nanoparticles allow multiple sizes (multiple colors) of Ag nanoparticles to be used as nanometer probes to determine the sizes of transport substrates and measure membrane permeability and porosity in living cells for an extended time.

CHAPTER IV

VALIDATION OF NANOPARTICLE OPTICS USING CONVENTIONAL METHODS

INTRODUCTION

Most methods used for the study of bacterial MDR mechanisms measure the accumulation of quinolone antibiotics in bacteria using radioactively labeled (^{14}C and ^3H) quinolones or natural fluorescent quinolones. Given that a common characteristic of MDR of bacteria (*P. aeruginosa*) is their broad resistance to quinolones, the popular method for assessing MDR is the measurement of time courses of fluorescence intensity of quinolones in the cells. Time courses of fluorescence intensity of quinolones have been widely used for real-time monitoring of the accumulation of substrates in bulk bacterial cells. This approach provides the average kinetics from a large population of cells. Individual cells, however, act independently and have unsynchronized membrane permeability, efflux pump machinery and accumulation kinetics.

Ethidium Bromide (EtBr) has been widely used as a fluorescence probe for the study of membrane permeability and extrusion machinery of bacterial cells. EtBr is especially suitable fluorescence probe for such study because EtBr emits weaker fluorescence in an aqueous environment (outside the cells) and becomes ten-fold more strongly fluorescent as it enters the cells and intercalates with DNA in the cells (81). It is well known that EtBr enters the cells using passive diffusion and is extruded out of cells by efflux pumps of *P. aeruginosa* using a proton motive force as an energy source. Due to its wide use as a probe to characterize bacteria cells and its ability to be used in

single bacteria cell accumulation kinetic experiments, EtBr was chosen as a probe to validate the results obtained from the use of Ag nanoparticles.

AZTREONAM EXPERIMENTS

Antibiotic Susceptibility Testing

Susceptibility testing and determination of MIC of AZT in the presence of 10 μ M EtBr or 1.3 pM Ag nanoparticles were performed using broth dilution method and single live cell imaging. Cells were first pre-cultured in L-broth medium as described previously and then cultured for an additional 8 hours in the same medium containing AZT (0, 3.13, 15.7, 31.3 μ g/mL) in the presence of 10 μ M EtBr or 1.3 pM Ag nanoparticles. The optical density of 10x dilution of cell solution at 600 nm (OD_{600nm}) was measured using UV-visible spectrometry to determine the proliferation of cells. A 20 μ L aliquot of each mixed solution was also imaged in a microchannel using single live cell imaging to determine the number of cells in the solution.

Fluorescence Spectroscopic Measurements

Time courses of fluorescence intensity of EtBr at 590 nm were measured using a fluorescence spectrometer (Perkin Elmer LS50B) with a time-drive mode at a 3 second data acquisition interval and with a 488 nm excitation line. These time courses of fluorescence intensity were used for real-time monitoring of EtBr accumulation kinetics in bulk live cells in the absence and presence of AZT (0, 3.13, 31.3 μ g/mL). The result was used to validate the nanoparticle optics assay for real-time measurement of the size-transformation of membrane permeability.

RESULTS

Fluorescence Spectroscopic Measurements

In order to rule out possible steric and size effects of using large Ag nanoparticles as a probe to measure the real-time function of AZT, the small molecule (EtBr) was used as a fluorescence probe for real-time measurement of accumulation of EtBr in the intact bulk cells. In the absence of AZT, time courses of fluorescence intensity of EtBr in intact cells (Fig. 21:a) demonstrated that fluorescence intensity of EtBr in all three strains increases with time slightly at a rate of $2 \times 10^{-3} \text{ s}^{-1}$. As AZT concentration increased from 0 to $3.13 \text{ } \mu\text{g/mL}$ AZT, fluorescence intensity of EtBr in nalB-1 increased with time most slowly with a rate at $3 \times 10^{-3} \text{ s}^{-1}$ whereas the fluorescence intensity of EtBr in ΔABM increased with time most rapidly with a rate at 0.1 s^{-1} . This result indicates that MexAB-OprM appeared to play a key role in the accumulation of EtBr in the cells in the absence and presence of $3.13 \text{ } \mu\text{g/mL}$ AZT. MexAB-OprM effectively extruded substrate (EtBr) out of the cells in the low AZT concentration ($0, 3.13 \text{ } \mu\text{g/mL}$). In $31.3 \text{ } \mu\text{g/mL}$ AZT, fluorescence intensity of EtBr in all three strains increased rapidly with time at a rate of 0.1 s^{-1} . At high AZT concentration ($31.3 \text{ } \mu\text{g/mL}$), the pump was unable to extrude the influx of EtBr that occurred with larger membrane permeability induced by AZT. This result agreed well with those observed using nanoparticle optics (Fig. 13 and Fig. 21), demonstrating that the real time nanoparticle optics assay is well suitable for the study of function of antibiotics in live cells. Unlike the bulk analysis using fluorescence spectroscopy, nanoparticle optics offers new insights into the size transformation of cellular membrane in single live cell at nanometer scale.

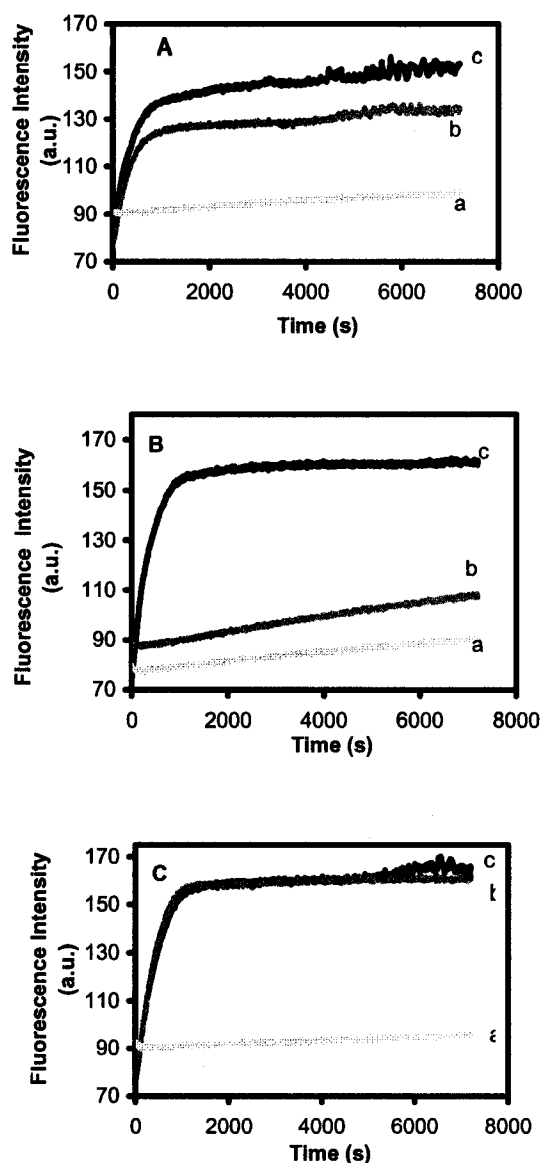


FIGURE 21. Real-time monitoring of EtBr accumulation kinetics in the *P. aeruginosa*. Representative time courses of fluorescence intensity of EtBr at 590 nm from the solutions containing 10 μM EtBr and the cells ($\text{OD}_{600\text{nm}} = 0.1$). Time courses of fluorescence intensity were acquired from the 3.0 mL solution in a quartz cuvette using fluorescence spectroscopy with time-drive mode at a 3 second data acquisition interval and 488 nm excitation. A, WT: (a) 0 $\mu\text{g/mL}$ AZT (b) 3.13 $\mu\text{g/mL}$ AZT (c) 31.3 $\mu\text{g/mL}$ AZT. B, nalB-1: (a) 0 $\mu\text{g/mL}$ AZT (b) 3.13 $\mu\text{g/mL}$ AZT (c) 31.3 $\mu\text{g/mL}$ AZT. C, ΔABM : (a) 0 $\mu\text{g/mL}$ AZT (b) 3.13 $\mu\text{g/mL}$ AZT (c) 31.3 $\mu\text{g/mL}$ AZT.

For example, when the blue nanoparticles accumulated inside the cells, the pores of membrane could be estimated as 50 ± 10 nm in diameter. When green nanoparticles

were observed inside the cells, the pores of the membrane could be determined to be at least 70 ± 10 nm in diameter.

Minimum Inhibitory Concentration

To ensure that 10 μ M EtBr and 1.3 pM Ag nanoparticles did not compete with AZT for accumulation in the cells, MIC of AZT was measured in 10 μ M EtBr (Fig. 22). The result indicated that MIC of AZT in 10 μ M EtBr or 1.3 pM Ag nanoparticles was the same as those observed in the absence of EtBr and Ag nanoparticle with MIC of AZT at 3.13 and 15.7 μ g/mL for WT and nalB-1, respectively. The result indicated that

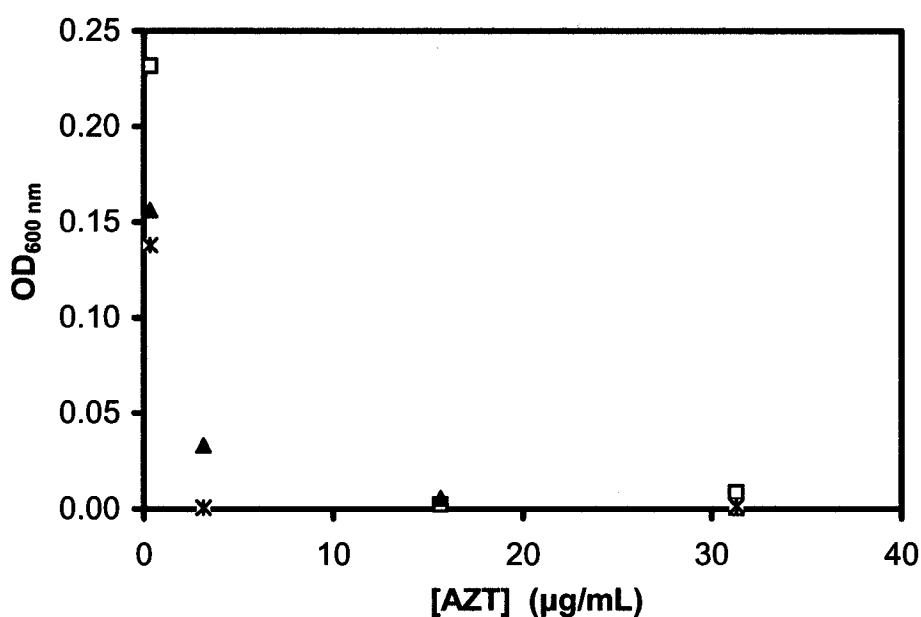


FIGURE 22. **Minimum inhibitory concentration (MIC) of aztreonam.** Δ ABM, WT and nalB-1: representative plots of OD_{600nm} versus AZT concentration from the solutions containing 10 μ M EtBr and Δ ABM (\square), WT (*) and nalB-1 (\blacktriangle) indicating that the MIC of Δ ABM, WT and nalB-1 was 3.13, 3.13 and 15.7 μ g/mL, respectively. Similar result was observed when 10 μ M EtBr was replaced by 1.3 pM Ag nanoparticles.

the presence of 10 μM EtBr or 1.3 pM nanoparticles did not affect the accumulation of AZT in the cells. The result also demonstrated that 10 μM EtBr and 1.3 pM Ag nanoparticles did not generate significant toxicity to the cells.

DISCUSSION

Comparison experiments using the small molecule EtBr as a fluorescence probe were carried out to validate nanoparticle optical assay for direct observation of the real-time function of AZT. EtBr has been a popular fluorescence probe for real-time monitoring of resistance mechanism in bulk cells. EtBr was especially suitable to serve as a fluorescent probe for such study because EtBr emits weaker fluorescence in aqueous environment and becomes strongly fluorescent in non-polar or hydrophobic environment, particularly as intercalates with DNA in cells. The MIC of AZT in the absence and presence of EtBr (10 μM) or Ag nanoparticles (1.3 pM) remained unchanged (Fig. 22), suggesting that the presence of EtBr (10 μM) or Ag nanoparticles (1.3 pM) neither interfered with the accumulation of AZT in the cells nor created significant toxicity to the cells. The results measured using EtBr and Ag nanoparticles were comparable and agreed well. Therefore, both EtBr (10 μM) and Ag nanoparticles (1.3 pM) are reliable probes for the real-time study of function of AZT in live cells.

CHLORAMPHENICOL EXPERIMENTS

Antibiotic Susceptibility Study

For minimum inhibitory concentration (MIC) measurements, cells were first pre-cultured in L-broth as previously described, and then cultured for an additional eight hours in the same medium containing chloramphenicol (0-250 $\mu\text{g/mL}$) in the presence and absence of 10 μM EtBr or 1.3 pM Ag nanoparticles. The cell growth curves were determined by measuring $\text{OD}_{600\text{ nm}}$ of 10x dilutions of the cell culture solutions using a

UV-visible spectrometer (Gary 2G, Varian). The plots of OD_{600 nm} versus chloramphenicol concentration were used to determine the MIC of chloramphenicol for the cells. In addition, a 20 μ L aliquot of each cell suspension was imaged in a microchannel using single living cell imaging to study the dependence of cell proliferation upon chloramphenicol concentration. The sealed microchannel was constructed by sandwiching the cell suspension between a microscope slide and a cover slip as described in detail in our previous publications. Using the same approach, the MICs of Ag nanoparticles and EtBr in the absence of chloramphenicol were also measured.

Fluorescence Spectroscopic Measurements

Transients of time-dependent fluorescence intensity of EtBr at 590 nm in the absence and presence of chloramphenicol were measured using a fluorescence spectrometer (Perkin-Elmer LS50B) with a time-drive mode at a 3 second data acquisition interval and a 488 nm excitation line. These time-dependent fluorescence intensity transients were used for real-time monitoring of EtBr accumulation kinetics in bulk living cells. The results were used to compare with those measured using single nanoparticle assay and single living cell imaging.

RESULTS

Fluorescence Spectroscopic Measurements

To rule out possible steric and size effects of using Ag nanoparticle probes for real-time monitoring of membrane permeability and porosity induced by chloramphenicol, we used a small molecule (EtBr) as a fluorescence probe, and measured accumulation kinetics of EtBr in bulk WT, nalB-1 and Δ ABM solutions in the presence of 0, 25 and 250 μ g/mL chloramphenicol. EtBr and chloramphenicol enter the

cells through passive diffusion and are extruded out of the cells by the efflux pumps in *P. aeruginosa* (82 - 85). The EtBr concentration at 10 μ M was deliberately selected to be much lower than chloramphenicol concentration, 25 μ g/mL (77 μ M) and 250 μ g/mL (770 μ M), allowing chloramphenicol to dominate the passive diffusion pathway and enter the cells. This approach minimized the possible effect of the presence of EtBr on the accumulation of chloramphenicol, ensuring the function of chloramphenicol to be studied using EtBr.

Transients of time-dependent fluorescence intensity of EtBr at 590 nm from the solutions containing 10 μ M EtBr and the cells (WT, nalB and Δ ABM) in the absence and presence of chloramphenicol (0, 25, and 250 μ g/mL) are shown in Fig. 23A, 23B and 23C, respectively. The changes of fluorescence intensity over time were used to monitor the real-time accumulation kinetics of EtBr in the cells as EtBr entered the cells and intercalated with DNA. The intercalation of EtBr with DNA results in a 10-fold increase in the fluorescence intensity of the dye. The accumulation rate of EtBr in 0, 25 and 250 μ g/mL chloramphenicol were measured and compared to determine the dose effect of chloramphenicol upon membrane permeability. The initial fluorescence intensity of each cell type varied slightly, which was attributed to variation of cell concentration ($OD_{600\text{ nm}} = 0.1 \pm 0.02$), distribution of cell sizes (1-2 μ m), and the fluctuation of excitation intensity of the Xe lamp in fluorescence spectrometer. In these experiments, the cells are incubated in PBS buffer solution at room temperature and the cells did not grow and divide significantly in such an environment. Thus, the cell concentration remained unchanged over 2-hour incubation.

In the absence of chloramphenicol (Fig. 23: a), the transients of time-dependent fluorescence intensity of EtBr in nalB-1, WT and Δ ABM, showed that fluorescence

intensity increased with time at a rate of 5×10^{-4} , 5×10^{-4} and $4 \times 10^{-3} \text{ s}^{-1}$, respectively. Results indicated that Δ ABM accumulated EtBr at approximately 10-fold (Fig. 23C: a) more rapidly than WT (Fig. 23A: a) and nalB-1 (Fig. 23B: a). As chloramphenicol concentration increased to 25 $\mu\text{g/mL}$ (Fig. 23: b), the fluorescence intensity increased with time at rates of 9×10^{-4} , 6×10^{-4} and $5 \times 10^{-3} \text{ s}^{-1}$, which was slightly (1.8, 1.2, and 1.3 fold) higher than the rates observed in the absence of chloramphenicol, for bulk

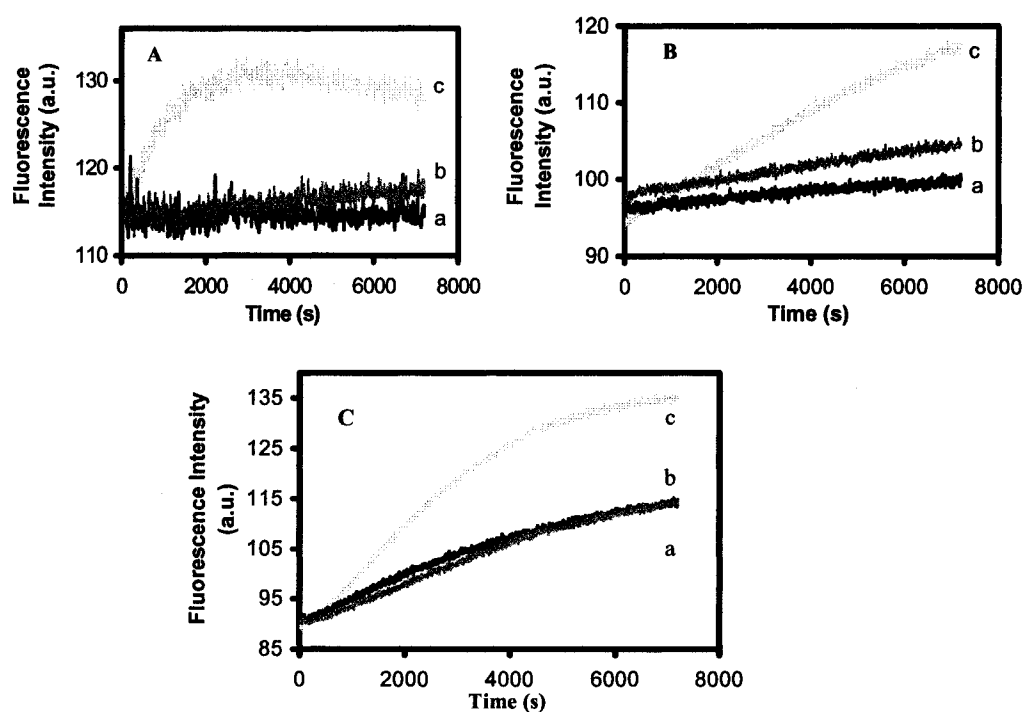


FIGURE 23. Real-time monitoring of EtBr accumulation kinetics in living cells. Representative time-dependent fluorescence intensity of EtBr at 590 nm from the 3.0 mL solutions containing 10 μM EtBr and the cells ($\text{OD}_{600 \text{ nm}} = 0.1$). A, WT: (a) 0 $\mu\text{g/mL}$ chloramphenicol, (b) 25 $\mu\text{g/mL}$ chloramphenicol (c) 250 $\mu\text{g/mL}$ chloramphenicol. B, nalB-1: (a) 0 $\mu\text{g/mL}$ chloramphenicol, (b) 25 $\mu\text{g/mL}$ chloramphenicol (c) 250 $\mu\text{g/mL}$ chloramphenicol. C, Δ ABM: (a) 0 $\mu\text{g/mL}$ chloramphenicol, (b) 25 $\mu\text{g/mL}$ chloramphenicol (c) 250 $\mu\text{g/mL}$ chloramphenicol.

WT, nalB-1 and Δ ABM, respectively. In contrast, as chloramphenicol concentration increased further to 250 $\mu\text{g/mL}$ (Fig. 23: c), fluorescence intensity increased with time at

rates of 3×10^{-3} , 9×10^{-3} and $1 \times 10^{-2} \text{ s}^{-1}$. These rates are 3, 18 and 2 times greater than the rates observed in 25 $\mu\text{g/mL}$ chloramphenicol, for nalB-1, WT and ΔABM , respectively. The rates of increased fluorescence intensity in ΔABM (Fig. 23C: c) are 1.1-fold and 3.3-fold higher than the rates observed in WT (Fig. 23A: c) and nalB-1 (Fig. 23B: c), respectively.

The results showed that the mutant devoid of MexAB-OprM (ΔABM) accumulated EtBr most rapidly, whereas the mutant with over-expression level of MexAB-OprM (nalB-1) accumulated EtBr most slowly. This suggests that MexAB-OprM played an important role in controlling the accumulation of EtBr. The results also agree qualitatively with those measured using single nanoparticle optics and single living cell imaging (Fig. 20), validating that single Ag nanoparticles may be used as nanometer scale probes for real-time size estimates of membrane transport in living cells. Unlike the accumulation kinetics measured using fluorescence probes (EtBr), the results acquired by single nanoparticles and single living cell images offer the new insights into the change of membrane permeability and pore sizes at the nanometer scale (Fig. 17 and 18). For example, Ag nanoparticles with sizes greater than 80 nm (red nanoparticle) appeared to have difficulty transporting through the membrane of *P. aeruginosa* in the absence of chloramphenicol (Fig. 18). In contrast, a greater number of larger nanoparticles were accumulated in living cells as chloramphenicol concentration increased (Fig. 17), suggesting that chloramphenicol increased the membrane permeability and pore sizes.

Antibiotic Susceptibility Testing

If Ag nanoparticles or EtBr competed with chloramphenicol for membrane transport and accumulation in the cells, such competition would have led to decreased

accumulation of chloramphenicol in the cells and in turn changed the susceptibility of chloramphenicol. To rule out the possibility of such competitive accumulation in the cells, the MIC of chloramphenicol in the presence of 10 μ M EtBr was determined by measuring optical density (OD) of cell suspension at 600 nm and imaging individual living cells in the cell suspension. Note that OD_{600 nm} and single living cell imaging were applied to determine the number of cells that had survived in the presence of particular concentration of chloramphenicol. Plots of OD_{600 nm} of bulk cell suspension versus chloramphenicol concentration (0, 2.5, 12.5, 25, 50, 250 μ g/mL) in Fig. 24 indicated

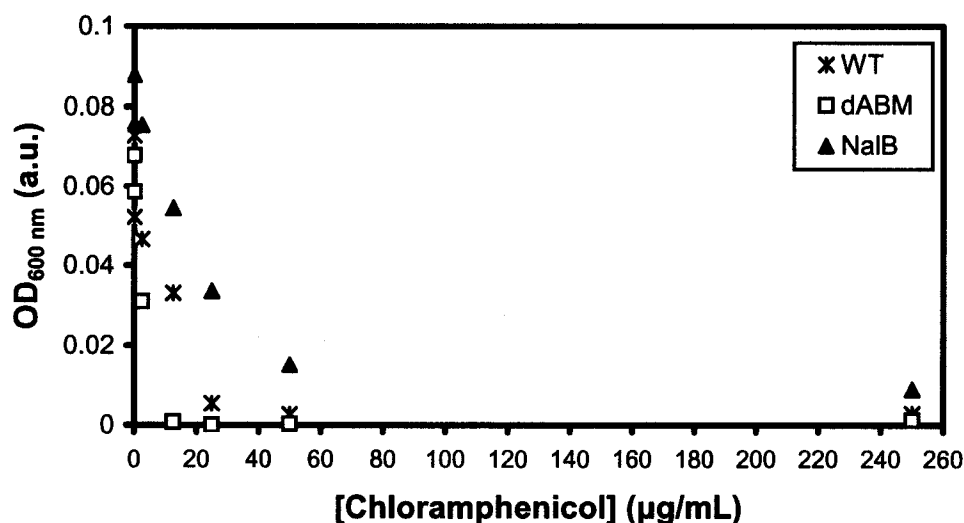


FIGURE 24. Minimum inhibitory concentration (MIC) of chloramphenicol. WT, nalB-1 and Δ ABM: Representative plots of OD_{600 nm} versus chloramphenicol concentration (0, 2.5, 12.5, 25, 50, and 250 μ g/mL) from the solutions containing 10 μ M EtBr and Δ ABM (\square), WT (*) and nalB-1 (\blacktriangle), indicating that the MIC of Δ ABM, WT and nalB-1 is 12.5, 25 and 250 μ g/mL, respectively.

MICs of 12.5, 25 and 250 $\mu\text{g/mL}$ chloramphenicol for ΔABM , WT and *nalB-1* cells, respectively.

DISCUSSION

EtBr has been widely used as a fluorescence probe for the study of membrane permeability and extrusion machinery of bacterial cells. EtBr is especially suitable fluorescence probe for such studies because EtBr emits weaker fluorescence in an aqueous environment (outside the cells) and becomes ten-fold more strongly fluorescent as it enters the cells and intercalates with DNA in the cells. It is well known that EtBr enters the cells using passive diffusion and is extruded out of cells by various efflux pumps of *P. aeruginosa* using a proton motive force as an energy source.

The fluorescence spectra of EtBr indicated that the emission peak at 590 nm remains unchanged in 2 h incubation of EtBr with the living cells; therefore, the transients of time-dependent fluorescence intensity at 590 nm were used to measure the accumulation kinetics of living cells. The results showed that fluorescence intensity increased with time more rapidly as chloramphenicol concentration increased and demonstrated that chloramphenicol increased membrane permeability (Fig. 23). The time-dependent fluorescence intensity transients also showed mutant dependence. The mutant devoid of MexAB-OprM (ΔABM) accumulated EtBr most rapidly, whereas the mutant with overexpression of MexAB-OprM (*nalB-1*) accumulated EtBr most slowly, suggesting that MexAB-OprM played a leading role in the accumulation of substrate (EtBr) in the cells. The accumulation kinetics measured using EtBr (Fig. 23) was consistent with those observed using single nanoparticles (Fig. 20), eliminating the concern of possible steric and size effects when using large nanoparticle probes for the study of membrane transport mechanism in living cells.

The MICs of chloramphenicol in the presence of 10 μM EtBr or 1.3 pM Ag nanoparticles also showed the mutant dependence, indicating MIC of 12.5, 25, and 250 $\mu\text{g/mL}$ for ΔABM , WT and *nalB-1*, respectively (Fig. 24). The MICs agreed well with those measured in the absence of EtBr and Ag nanoparticles, further suggesting that the presence of 10 μM EtBr or 1.3 pM Ag nanoparticles neither affected the accumulation of chloramphenicol in the cells nor created significant toxicity to the cells. This result further confirms that a low concentration of Ag nanoparticles (1.3 pM) can be used as powerful nanoprobes to study real-time membrane transport in living microbial cells.

Unlike fluorescence probes, Ag nanoparticles can offer real-time size information of the substrates that transport through living cell membranes at the nanometer scale. Because the color index of nanoparticles can be used as a nanometer size index, the size transformation and accumulation kinetics can be measured directly; we reported membrane transformation with millisecond temporal resolution using dark-field optical microscopy and spectroscopy. In addition, the scattering intensity of Ag nanoparticles decreases slightly ($\sim 10\%$) as nanoparticles pass through the membrane and enter the cells, offering the opportunity to trace the transport of nanoparticles in and out of the membrane by monitoring scattering intensity over time. Furthermore, the scattering intensity of Ag nanoparticles does not decay over time, owing to their resistance to photodecomposition. Taken together, these unique characteristics of Ag nanoparticles allow multiple sizes (multiple colors) of Ag nanoparticles to be used as nanometer probes to determine the sizes of substrates transported and measure changes in membrane permeability and porosity in living cells for an extended time.

CHAPTER V

CONCLUSIONS

GOLD NANOPARTICLES

In conclusion, we have studied the color-change kinetics of the colloidal Au nanoparticles (6.5, 19, 48, 97 nm) induced by a variety of concentrations of $\text{Ru}(\text{bpy})_3^{2+}$ at 24.0, 33.0 and 51.0 °C. The new findings are summarized as follows. (i) The minimum (critical) concentration of $\text{Ru}(\text{bpy})_3^{2+}$ needed to change the color of the Au nanoparticles is highly dependent upon temperature, the size of nanoparticles, the surface Au atoms of the individual nanoparticle, and the total surface Au atoms of all nanoparticles in the solution. (ii) The surface plasmon absorption (color) of Au nanoparticle solution in the presence of the critical concentration of $\text{Ru}(\text{bpy})_3^{2+}$ is highly sensitive to temperature and nanoparticle size, suggesting that the surface plasmon absorption of Au nanoparticle solution can be altered by temperature and the surface adsorbates, $\text{Ru}(\text{bpy})_3^{2+}$. (iii) The color-change rate of Au nanoparticles is highly sensitive to the presence of $\text{Ru}(\text{bpy})_3^{2+}$ concentration. For example, the rate of the 19 nm Au nanoparticles (0.36 nM) changes 3-fold in response to a variation of 7 pmol $\text{Ru}(\text{bpy})_3^{2+}$. Taken together, these findings suggest the possibility of ultra-sensitive analysis of surface adsorbates using the colorimetry of Au nanoparticles and the design of optical properties of Au nanoparticles by modification of Au nanoparticle surfaces with specific adsorbates. These findings also open upon the new opportunity for the study of photochemistry of $\text{Ru}(\text{bpy})_3^{2+}$ on the Au nanoparticle surfaces.

AZTREONAM

Silver nanoparticle optics were developed and applied for real-time study of the modes of action of AZT in live bacterial cells. Real-time size transformation of cell wall

and membrane permeability induced by AZT was directly observed using nanoparticle optics and single live cell imaging. The results suggest that AZT induces real-time size transformation of membrane permeability and disruption of cell wall. This study has demonstrated that noble metal nanoparticles could serve as a non-bleaching nanometer probe for real-time monitoring of function of antibiotics in live cells. The real-time nanoparticle optical assay offers a rapid tool for real-time screening of antibiotics with ms temporal and nm size resolution, and provides the unique new opportunity for better evaluation of the pharmacokinetics of antibiotics. One can now use this unique tool to study the function of other antibiotics in live cells for a better characterization of the antibiotic mode of action and further advancing the understanding of MDR mechanism in real-time.

CHLORAMPHENICOL

We developed and applied single Ag nanoparticle optics and single living cell imaging to investigate membrane transport in living microbial cells (*P. aeruginosa*) in real time. New findings from this study include: (i) in the absence of antibiotics, Ag nanoparticles with sizes up to 80 nm can transport through the inner and outer cellular membrane of *P. aeruginosa*; this is about 50 times larger than the size of conventional antibiotics. The majority of the intracellular Ag nanoparticles are located in the cytoplasmic space of the cells, whereas a few nanoparticles are just underneath the cellular membrane. (ii) Single nanoparticle optics and single living cell imaging can be used to investigate the new function of antibiotics. For example, this study indicates that chloramphenicol increases the membrane permeability in a dose-dependent manner, which has not been reported previously.

ETHIDIUM BROMIDE

We incorporated the fluorescence probe EtBr, which is well known to enter the cell via passive diffusion and is extruded out of cells by various efflux pumps of *P. aeruginosa*, as a control to verify the Ag nanoparticle accumulation data. The new findings are summarized: (i) the accumulation kinetics of intracellular Ag nanoparticles measured using single nanoparticle optics and single cell imaging are similar to the bulk population accumulation kinetics of EtBr. This observation validates that Ag nanoparticles can be used as nanoprobe to measure membrane transport mechanisms of microbial cells in real-time. (ii) MICs of both aztreonam and chloramphenicol in the absence and presence of 1.3 pM Ag nanoparticles or 10 μ M EtBr remain the same. This indicates that neither 1.3 pM Ag nanoparticles nor 10 μ M EtBr affects the accumulation of antibiotics in *P. aeruginosa* and suggests that neither 1.3 pM Ag nanoparticle nor 10 μ M EtBr creates significant toxicity to the bacteria. Taken together, this study further demonstrates that a low concentration of Ag nanoparticles (1.3 pM) can be used as powerful nanoprobe to study membrane transport in living microbial cells.

REFERENCES

1. Stover, C. K., Pham, X. Q., Erwin, A. L., Mizoguchi, S. D., Warren, P., Hickey, M. J., Brinkman, F. S., Hufnagle, W. O., Kowalik, D. J., Lagrou, M., Garber, R. L., Goltry, L., Tolentino, E., Westbrook-Wadman, S., Yuan, Y., Brody, L. L., Coulter, S. N., Folger, K. R., Kas, A., Larbig, K., Lim, R., Smith, K., Spencer, D., Wong, G. K., Wu, Z., and Paulsen, I. T. (2000) *Nature* **406**, 959-964
2. Nakae, T. (1997) *Microbiologia* **13**, 273-284
3. Masuda, N., Sakagawa, E., Ohya, S., Gotoh, N., Tsujimoto, H., and Nishino, T. (2000) *Antimicrob. Agents Chemother.* **44**, 3322-3327
4. Lee, A., Mao, W., Warren, M., Mistry, A., Hoshino, K., Okumura, R., and Ishida, H. (2000) *O. J. Bacteriol.* **182**, 3142-3150
5. Maseda, H., Yoneyama, H., and Nakae, T. (2000) *Antimicrob. Agents Chemother.* **44**, 658-664
6. Ahmadi, T., Logunov, S., and El-Sayed, M. (1997) *ACS Symp. Ser. Nanostructured Materials* **679**, 125-140
7. Hodak, J., Henglein, A., and Hartland, G. (2000) *Pure. Appl. Chem.* **72**, 189-197
8. Brown, L., and Hutchison, J. (1999) *J. Am. Chem. Soc.* **121**, 882-883
9. Lyon, L., Pena, D., and Natan, M. (1999) *J. Phys. Chem. B* **103**, 5826-5831
10. Park, S., Im, J., Chun, B., and Kim, J. (1999) *Microchem. J.* **63**, 71-91
11. Davidović, D., and Tinkham, M. (1999) *Phys. Rev. Lett.* **83**, 1644-1647
12. Ghaddar, T., Wishart, J., Kirby, J., Whitesell, J., and Fox, M. (2001) *J. Am. Chem. Soc.* **123**, 12832-12836
13. Han, M., and Quek, C. (2000) *Langmuir* **16**, 362-367

14. Demers, L., Mirkin, C., Mucic, R., Reynolds, R., Letsinger, R., Elghanian, R., and Viswanadham, G. (2000) *Anal. Chem.* **72**, 5535-5541
15. Link, S., Burda, C., Wang, Z. L., and El-Sayed, M. (1999) *J. Chem. Phys.* **111**, 1255
16. Link, S., and El-Sayed, M. (1999) *J. Phys. Chem. B* **103**, 4212-4217
17. Templeton, A., Hostetler, M., Kraft, C., and Murray, R. (1998) *J. Am. Chem. Soc.* **120**, 1906-1911
18. Mie, G. (1908) *Ann. Phys.* **25**, 377-445
19. Sato, S., Toda, K., and Oniki, S. (1999) *J. Colloid. Interface Sci.* **218**, 504-510
20. Anderson, M., Morris, C., Stroud, R., Merzbacher, C., and Rolison, D. R. (1999) *Langmuir* **15**, 674-681
21. Eck, D., and Helm, C. (2001) *Langmuir* **17**, 957-960
22. Musick, M., Keating, C., Keefe, M., and Natan, M. (1997) *J. Chem. Mater.* **9**, 1499-1502
23. Yoneyama, H., Maseda, H., Kamiguchi, H., and Nakae, T. (2000) *J. Biol. Chem.* **275**, 4628-4634
24. Morjani, H., Aouali, N., Belhoussine, R., Veldman, R. J., Levade, T., and Manfait, M. (2001) *Int. J. Cancer.* **94**, 157-65
25. Xu, N., Wan, Q., Kyriacou, S., Brownlow, W., and Nowak, M. (2003) *Biochem. Biophys. Res. Commun.* **305**, 941-949
26. Liu, P. (1974) *J Infect Dis.* **130** 94-99
27. Ma, D., Cook, D., Hearst, J., and Nikaido, H. (1994) *Trends Microbiol.* **2**, 489-493

28. Greenwood, D. (1997) in *Antibiotic and Chemotherapy: Anti-infective Agents and Their Use in Therapy* (O'grady, F., Lambert, H. P., Finch, R. G. and Greenwood, D., eds) 7th Ed. pp 10-21, Churchill Press, Livingstone, NY
29. Ocaktan, A., Yoneyama, H., and Nakae, T., (1997) *J. Biol. Chem.* **272**, 21964-21969
30. Fung-Tomc, J., Gradelski, E., Valera, L., Huczko, E., and Bonner, D. (2002) *Int. J. Antimicrob. Agents.* **20**, 57-60
31. Palasubramaniam, S., and Parasakthi, N. (2001) *Malays. J. Pathol.* **23**, 73-78
32. Morshed, S., Lei, Y., Yoneyama, H., and Nakae, T. (1995) *Biochem. Biophys. Res. Commun.* **210**, 356-362
33. Mulvaney, P. (1996) *Langmuir* **12**, 788-800
34. Kharitonov, A., Shipway, A., and Willner, I. (1999) *Anal. Chem.* **71**, 5441-5443
35. McConnell, W., Novak, J., Brousseau III, L., Fuierer, R., Tenent, R., and Feldheim, D. (2000) *J. Phys. Chem.* **104**, 8925-8930
36. Whyman, R. (1996) *Gold Bulletin* **29**, 11-15
37. Bohren, C. F., and Huffman, D. R. (1983) in *Absorption and Scattering of Light by Small Particles*; 1st Ed pp 287-380, Dover Publications Inc., New York, NY
38. Kreibig, U., and Vollmer, M. (1995) in *Optical Properties of Metal Clusters* (Springer Series in Material Science, Vol 25) pp 14-123 Springer Publishing, Berlin, Germany
39. Haes, A., and Van Duyne, R. (2002) *J. Am. Chem. Soc.* **124**, 10596-10604
40. Handley, D. A. (1989) in *Colloid Gold: Principles, Methods and Applications* (Hayat, M. A., Ed.) pp 1-8, Academic Press, New York, NY

41. Grabar, K., Freeman, R., Hommer, M., and Natan, M. (1995) *Anal. Chem.* **67**, 735-743
42. Wada, Y., Hamasaki, T., and Satir, P. (2000) *Mol. Biol. Cell* **11**, 161-169
43. Mirkin, C., Letsinger, R., Mucic, R., and Storhoff, J. (1996) *Nature* **382**, 607-609
44. Xu, N., Chen, J., Jeffers, R., and Kyriacou, S. (2002) *Nano Letters* **2**, 175-182
45. Sandhu, K., Simard, J., McIntosh, C., Smith, S., and Rotello, V. (2002) *Bioconjugate Chem.* **13**, 3-6
46. Xu, N., and Patel, R. (2004), in *Encyclopedia of Nanoscience and Nanotechnology* (Nalwa, H. S., Ed.) pp.181-192, American Scientific Publishers, Stevenson Ranch, CA
47. Kyriacou, S., Brownlow, W., and Xu, N. (2004) *Biochemistry* **43**, 140-147
48. Xu, N., and Patel, R. (2004) in *Handbook of Nanostructured Biomaterials and Their Applications in Nanobiotechnology* (Nalwa, H. S., ed.) American Scientific Publishers, Stevenson Ranch, CA
49. Teranishi, T., Haga, M., Shiozawa, Y., and Miyake, M. (2000) *J. Am. Chem. Soc.* **122**, 4237-4238
50. Link, S., and El-Sayed, M., (1999) *J. Phys. Chem. B* **103**, 8410-8426
51. Kreibig, U., and Genzel, U. (1985) *Surf. Sci.* **156**, 678-700
52. Kimura, K. (1996) *Surface Review and Letters* **3**, 1219-1222
53. Shipway, A., Lahav, M., Gabai, R., and Willner, I. (2000) *Langmuir* **16**, 8789-8795
54. Brown, K., Walter, D., and Natan, M. (2000) *Chem. Mater.* **12**, 306-313
55. Zamborini, F., Hicks, J., and Murray, R. (2000) *J. Am. Chem. Soc.* **122**, 4514-4515

56. Templeton, A., Hostetler, M., Kraft, C., and Murray, R. (1998) *J. Am. Chem. Soc.* **120**, 1906-1911
57. Maye, M., Chun, S., Han, L., Rabinovich, D., and Zhong, C. (2002) *J. Am. Chem. Soc.* **124**, 4958-4959
58. Shipway, A., Lahav, M., Blonder, R., and Willner, I. (1999) *Chem. Mater.* **11**, 13-15
59. Lahav, M., Heleg-Shabtai, V., Wasserman, J., Katz, E., Willner, I., Dürr, H., Hu, Y., and Bossmann, S. (2000) *J. Am. Chem. Soc.* **122**, 11480-11487
60. Roundhill, D. M. (1994) in *Modern Inorganic Chemistry* (Fackler, J. P., Ed.) pp. 165-169, Plenum, New York, NY
61. Xu, X., and Bard, A. (1994) *Langmuir* **10**, 2409-2414
62. Huang, T., and Murray, R. (2002) *Langmuir* **18**, 7077-7081
63. Hövel, H., Fritz, S., Hilger, A., and Kreibitz, U. (1993) *Phys. Rev.* **48**, 1817-1820
64. Perner, M., Bost, P., Lemmer, U., Plessen, G., and Feldmann, J. (1997) *Phys. Rev. Lett.* **78**, 2192-2195
65. Handley, D., (1989), in *Colloid Gold: Principles, Methods and Applications*; (Hayat, M. A., Ed) pp.15-27, Academic Press, New York, NY
66. Huang, T., and Murray, R. (2002) *Langmuir* **18**, 7077-7081
67. Poole, K. (2001) *J. Mol. Microbiol. Biotechnol.* **3**, 255-264
68. Ryan, B., Dougherty, T., Beaulieu, D., Chuang, J., Dougherty, B., and Barrett, J. (2001) *Expert Opin.* **10**, 1409-1422
69. Morshed, S. R., Lei, Y., Yoneyama, H., and Nakae, T. (1995) *Biochem. Biophys. Res. Commun.* **210**, 356-362

70. Mortimer, P., and Piddock, L. (1991) *J. Antimicrob. Chemother.* **28**, 639-653
71. Kyriacou, S., Nowak, M., Brownlow, W., and Xu, N. (2002) *J. Biomed. Opt.* **7**, 576-586
72. Xu, N., Brownlow, W., Huang, S., and Chen, J. (2003) *Biochem. Biophys. Res. Commun.* **305**, 79-86
73. Andrews, J. (2001) *J. Antimicrob. Chemother.* **48**, 5-16
74. Okazaki, M., Suzuki, K., Asano, K., Shukuya, N., Egami, T., Higurashi, Y., Morita, K., Uchimura, H., and Watanabe, T. (2002) *J. Infect. Chemother.* **8**, 37-42
75. Bedenic, B., Randegger, C., Boras, A., and Haechler, H. (2001) *Chemother.* **13**, 24-33
76. Saito, K., Yoneyama, H., and Nakae, T. (1999) *FEMS Microbiol. Lett.* **179**, 67-72
77. Steel, C., Wan, Q., and Xu, N. (2004) *Biochemistry* **43**, 175-182
78. Xu, N., Jeffers, R., Gao, J., and Logan, B. (2001) *The Analyst*, **126**, 1285-1292
79. Klaus, T., Joerger, R., Olsson, E., and Granqvist, C. (1999) *Proc. Natl. Acad. Sci.* **96**, 13611-13614
80. Haynes, C., and Van Duyne, R. (2001) *J. Phys. Chem. B* **105**, 5599-5611
81. Morgan, A., Lee, J., Pulleyblank, D., Murray, N., and Evans, D., (1979) *Nucleic Acids Res.* **7**, 547-569
82. Yoneyama, H., Ocaktan, A., Tsuda, M., and Nakae, T. (1997) *Biochem. Biophys. Res. Commun.* **233**, 611-618
83. Yoneyama, H., Ocaktan, A., Gotoh, N., Nishino, T., and Nakae, T. (1998) *Biochem. Biophys. Res. Commun.* **244**, 898-902

84. Li, X., Livermore, D., and Nikaido, H. (1994) *Antimicrob. Agents. Chemother.* **38**, 1732-1741
85. Li, X., Livermore, D., and Nikaido, H. (1995) *Antimicrob. Agents. Chemother* **39**, 1948-1953

VITA

William John Brownlow

Department of Chemistry and Biochemistry
Old Dominion University
4541 Hampton Boulevard
Norfolk, VA 23529-0126

Education

- December, 2006 M.S. Chemistry, Old Dominion University, Norfolk, VA
 Thesis: *Development of Single Nanoparticle Optical Assays for Imaging Single Living Cells*
- May, 1994 B.S. Chemical Engineering, Virginia Tech, Blacksburg, VA
 Minor in Chemistry

Publications

- “Single Live Cell Imaging for Real-Time Monitoring of Resistance Mechanism in *Pseudomonas aeruginosa*”, S. Kyriacou, M. Nowak, W. Brownlow, X. N. Xu*, *Journal of Biomedical Optics*, 7(4), 2002
- "Single Molecule Detection of Efflux Pump Machinery in *Pseudomonas aeruginosa* ", X.N. Xu*, W. Brownlow, S. Huang and J. Chen, *Biochemical and Biophysical Research Communications*, 305(2), 2003
- “Using Nanoparticle Optics Assay for Direct Observation of the Function of Antimicrobial Agents in Single Live Bacterial Cells”, S. Kyriacou, W. Brownlow, X. N. Xu*, *Biochemistry*, 2003
- “Real-Time Probing of Membrane Transport in Living Microbial Cells Using Single Nanoparticle Optics and Living Cell Imaging”, X. N. Xu*, W. Brownlow, S. Kyriacou, Q. Wan, J. Viola, *Biochemistry*, 2004
- “Direct Observation of Substrate Induction of Resistance Mechanism in *Pseudomonas aeruginosa* Using Single Live Cell Imaging”, X. N. Xu*, Q. Wan, S. Kyriacou, W. Brownlow and M. Nowak, *Biochemical and Biophysical Research Communications*, 305, 2003
- “Size and Temperature Dependence of Surface Plasmon Absorption of Gold Nanoparticles Induced by Tris(2,2'-bipyridine) ruthenium(II)”, X. N. Xu*, S. Huang, W. Brownlow, K. Salatia, and R. Jeffers, *The Journal of Physical Chemistry B*, 43(32), 2004